OPTIMIZATION OF BEAM PAINTING FOR ELF/VLF WAVE GENERATION AT HAARP USING TIME-OF-ARRIVAL ANALYSIS

By

SHUJI FUJIMARU

A DISSERTATION PRESENTED TO THE GRADUATE SCHOOL
OF THE UNIVERSITY OF FLORIDA IN PARTIAL FULFILLMENT
OF THE REQUIREMENTS FOR THE DEGREE OF
DOCTOR OF PHILOSOPHY

UNIVERSITY OF FLORIDA

2014

I dedicate this dissertation to my parents, Akio and Ikuyo Fujimaru, to my brother Yoshiki Fujimaru, and to my grandparents, Mitsuyoshi and Yuko Fujimaru and Shinako Hosozawa.

ACKNOWLEDGMENTS

I would like to express my appreciation to my adviser, Dr. Robert Moore, for his encouragement, guidance, and help throughout my graduate studies. This dissertation would not possibly have been completed in a professional manner without his patient and unselfish support. I also would like to thank Dr. Vladimir Rakov, Dr. Subrata Roy, Dr. Martin Uman, and Dr. YK Yoon for serving as members of my PhD committee and for providing precise and prompt feedback on this dissertation despite their busy schedules.

I am grateful to all my colleagues with whom I have shared a fulfilling research experience through my graduate school life. I am especially grateful to Daniel Kotovsky for providing helpful advice on plasma physics and electromagnetics, to Michael Mitchel for providing unfailing support of observational instruments, to Neal Dupree for sharing the hard work of instrument deployment, and to all the other lab members with whom I have had the pleasure to work: Tong Wang, Divya Agrawal, Jerrod Langston, Sydney Greene, Matthew Bell, and Dian Li.

Without the tremendous help I received from the HAARP staff and the Alaskan locals to deploy instruments, perform experiments, and collect data in the treacherous Alaskan wilderness, I would not have been able to complete this dissertation. I would like to especially thank Dr. Mike McCarrick for implementing my transmission sequences at HAARP, Jay Scrimshaw for letting us operate the instruments at his homes in Gakona and Copper Lake, Doug and Judy Frederick for keeping our instrument warm with their generator at Paradise, Barbara Charley for sharing her cabin with our instrument, and Norma and Doyle Traw for providing us warm housing and breakfast in Chistochina.

Lastly, I owe my deepest gratitude to my parents and families in Japan for being my life support with their unconditional love.

This work is supported in part by the following grants and contracts to the University of Florida: DARPA contract HR0011-09-C-0099, US Air Force grant FA9453-12-1-00246, ONR grant #N000141010909, DARPA grant HR0011-10-1-0061, and NSF grants AGS-0940248 and ANT-0944639.

TABLE OF CONTENTS

page

CHAPTER

LIST OF TABLES

LIST OF FIGURES

Abstract of Dissertation Presented to the Graduate School
of the University of Florida in Partial Fulfillment of the
Requirements for the Degree of Doctor of Philosophy

OPTIMIZATION OF BEAM PAINTING FOR ELF/VLF WAVE GENERATION AT HAARP USING TIME-OF-ARRIVAL ANALYSIS

By

Shuji Fujimaru

May 2014

Chair: Robert C. Moore
Major: Electrical and Computer Engineering

This dissertation experimentally and theoretically investigates the generation of radio waves in the extremely low frequency (ELF, 3–3000 Hz) and very low frequency (VLF, 3–30 kHz) bands by high frequency (HF, 3–30 MHz) heating of the lower ionosphere. ELF and VLF waves can propagate to large distances around the globe with little attenuation, making them ideally suited for long distance communications and ionospheric remote sensing. These waves may also propagate into near-Earth space, where they can control the population of energetic radiation belt particles. Improving the efficiency of this unconventional mechanism for ELF/VLF wave generation is the primary emphasis of this work.

For the experimental observations presented herein, the ELF/VLF signal detected at the receiver is considered to be the sum of several multi-path components. These multi-path components are produced by reflections from the ground and the lower ionosphere. A novel time-of-arrival (TOA) analysis technique is applied to observations to distinguish between line-of-sight (LOS) and ionospherically-reflected (IR) components. This decomposition enables the experimental differentiation of HF heating (i.e., source) effects and Earth-ionosphere waveguide (i.e., propagation) effects. TOA analysis of experimental observations for various HF heating schemes are compared against a theoretical model to demonstrate the validity of the technique.

TOA analysis is applied to evaluate the ELF/VLF source properties produced by rapidly scanning the HF beam across the ionosphere, a very efficient modulation technique known as beam-painting. By precisely controlling the duration of the HF pulse during the beam-painting

experiments, the amplitude and phase of individual ELF/VLF array elements are experimentally measured. The influence of the source area, phasing distribution, heating and cooling time scales, and obliqueness of the HF beam on the received ELF/VLF amplitude are experimentally quantified for the first time. Based on these observations, a simple change to the modulation format is proposed to significantly increase the received ELF/VLF amplitude by $>$4 dB and the HF-to-ELF conversion efficiency by $>$7 dB.

Lastly, a rigorous optimization method is applied to maximize the received ELF/VLF wave amplitude. The optimization is based on experimental observations, and utilizes the observed amplitudes, phases, and propagation delays associated with 8 different HF heating locations. The optimal heating pattern is predicted to increase the received ELF/VLF amplitude by $\sim$7 dB and the HF-to-ELF conversion efficiency by $\sim$11 dB, constituting a tremendous improvement over the current state-of-the-art modulation formats.

CHAPTER 1
INTRODUCTION

This dissertation investigates the generation of radio waves in the extremely low frequency (ELF, 3–3000 Hz) and very low frequency (VLF, 3–30 kHz) bands by high frequency (HF, 3–30 MHz) heating of the lower ionosphere in the presence of the auroral elecrojet current system. All experiments presented herein were performed at the High Frequency Active Auroral Research Program (HAARP) observatory in Gakona, Alaska. A novel method is employed to isolate the detected ELF/VLF signal from Earth-ionosphere waveguide propagation effects. As a direct result of this analysis, new HF modulation techniques are proposed to optimize the amplitude of the ELF/VLF signal received at a single site. This chapter introduces the difficulties associated with conventional ELF/VLF wave generation, provides a literature review focused ELF/VLF wave generation by HF heating, and concludes by identifying the scientific contributions of this dissertation.

1.1 Conventional ELF/VLF Wave Generation

ELF/VLF waves reflect between the Earth's ionosphere and ground and propagate to global-scale distances with relatively low attenuation in the Earth-ionosphere waveguide. They also penetrate tens of meters into seawater. For these reasons, they are ideally suited for long-distance communications. Navies in several countries use ELF and VLF waves to communicate with submerged vehicles [e.g., *Bernstein et al.*, 1974; *Merrill*, 1974]. Before the advent of the global position system (GPS), ELF/VLF waves were used for global navigation and time transfer [e.g., *Frank*, 1983; *Swanson*, 1983], and they have subsequently provided a valid, although coarser, failsafe for GPS. Furthermore, ELF/VLF waves are effective tools for remotely sensing the properties of the ionosphere [e.g., *Cummer et al.*, 1998; *Agrawal and Moore*, 2012] and magnetosphere [e.g., *Inan and Carpenter*, 1987; *Gołkowski et al.*, 2011]. For instance, particular attention has been paid to the ionospheric and magnetospheric effects of lightning [e.g., *Lauben et al.*, 2001; *Dowden et al.*, 2002; *Moore et al.*, 2003; *Said et al.*, 2010] and nuclear explosions [e.g., *Field and Engel*, 1965; *Helliwell*, 1965].

Despite the numerous communications-oriented and scientific applications, conventional methods for the generation of ELF/VLF waves are costly. Although a number of VLF transmitters currently operate in the $\sim$15–30 kHz band with reasonable efficiency ($>$20%), the required antenna size is on the order of hundreds of meters [*Watt*, 1967]. One of the most powerful VLF transmitters is operated at Cutler, Maine by the US Navy. This transmitter consists of two star antennas: each antenna is a vertical monopole with leads connecting the center mast to six surrounding masts. The average height of the masts is $\sim$200 m and the total area enclosed by the antennas is $\sim 2 \times 10^6$ m^2 ($\sim$500 acres). The center mast that radiates the signal is $\sim$300 m high, and it is still electronically small for the 10–20 km wavelength in the upper VLF range. Tuning to the resonant frequency makes it possible to maintain $>$70% radiation efficiency at 14 kHz [*Watt*, 1967], but the bandwidth of operation is significantly limited (100's of Hz). It should be noted that the Cutler transmitter presently operates at a different frequency (24.0 kHz).

At the lower end of the ELF/VLF frequency range ($<$5 kHz), a long horizontal wire is a more practical implementation that can achieve lengths comparable to a wavelength ($>$60 km). Because the long horizontal wire lies close to the ground, however, image sources tend to cancel most of the radiated fields. Even on thick ice sheets, ELF/VLF antennas radiate with low efficiency. For instance at Siple Station, Antarctica, a 21.4 km horizontal antenna transmitted waves at a few kHz with at most $\sim$2% efficiency [*Raghuram et al.*, 1974]. For low-ELF frequencies ($<$100 Hz), the antenna project at the Wisconsin Test Facility used a multitude of $\sim$22.5 km wires to achieve efficiencies on the order of $\sim$0.01% [*Papadopoulos et al.*, 1990]. In this case, once again, the bandwidth of the transmission is severely limited.

For all of these transmitters, operation and maintenance costs are high and the available bandwidth is a small fraction of the center frequency. From this perspective, modulated HF heating of the ionosphere in the presence of naturally occurring electric currents is an important alternative method to generate ELF/VLF waves, and simultaneously provides a means to study long distance ELF/VLF propagation in a controlled environment. While this unconventional method for ELF/VLF wave generation suffers from even lower efficiency ($\sim$0.0001–0.001%) [*Barr et al.*, 1985; *Moore et al.*, 2007; *Cohen and Gołkowski*, 2013], it is not significantly limited in bandwidth. Recent efforts to improve the efficiency have achieved a 10-fold enhancement in radiated ELF/VLF power by rapidly scanning the HF beam across the ionosphere [*Cohen et al.*, 2008, 2010a,b]. While the improvement in efficiency has been documented, the physical reasons for the improvement have not been experimentally quantified. As a result, it is not yet possible to optimize the ELF/VLF source region for controlled injection into the Earth-ionosphere waveguide or into near-Earth space. As a first step toward providing such capabilities, this dissertation experimentally quantifies the effects produced by individual HF beam steering parameters on ELF/VLF wave generation and investigates the optimal combination of those parameters to maximize the ELF/VLF wave amplitude received at an individual ground-based receiver.

1.2 Previous Measurements of Ionospheric ELF/VLF Wave Generation

Since *Getmantsev et al.* [1974] first succeeded in ELF/VLF wave generation by heating the ionosphere, a number of efforts have been conducted in order to increase the efficiency of ELF/VLF wave generation, which is on the order of $\sim$0.0001–0.001$\%$. Typically, the radiated power of the ELF/VLF wave source is estimated by comparing the observed ELF/VLF amplitude with an HF heating and ELF/VLF wave propagation model. At Tromsø, Norway, using 1 MW of HF power, *Barr et al.* [1985] estimated 1 to 2 W of radiated ELF/VLF power, depending on the ionospheric condition. At HAARP in Alaska, using 960 kW of HF power, *Moore* [2007] estimated 4–32 W (and detected the signal more than 4,500 km away from HAARP). More recently, after an upgrade of the HAARP HF transmitter to 3.6 MW, *Cohen and Gołkowski* [2013] estimated a maximum radiated ELF/VLF power of $\sim$265 W. For these estimations, the transmission formats were limited to a vertical, narrow beam with amplitude modulation, and the carrier and modulation frequencies were 2.75–3.25 MHz and 0.5–3.5 kHz respectively. Of course, ELF/VLF wave generation depends on the strength of the auroral electrojet currents, on the properties of the ionosphere, and on the HF transmission parameters employed. Although we can only control the last of these items, it is worth explaining the importance of the geomagnetic conditions local to HAARP prior to delving into the HF transmission parameters.

1.2.1 Local Ionospheric and Geomagnetic Conditions

Local ionospheric and geomagnetic conditions play an important role determining the ELF/VLF signal strength and generation efficiency. The properties of the ionosphere vary significantly with time (even minute by minute). Strong or weak ELF/VLF signals can be generated, depending on how the electron density and electron temperature vary with altitude within the *D*-region ionosphere, even for the same HF beam configuration. In essence, the ionospheric parameters affect the efficiency of ionospheric conductivity modulation produced by HF heating. *Cohen and Gołkowski* [2013] statistically analyzed ELF/VLF signal generation at HAARP for over a course of 91 days. Their analysis revealed that the average ELF/VLF signal strength was highest during the daytime, but the strongest signal levels (for shorter periods of time) were generated during the nighttime. This statistical observation is consistent with the theoretical model of *Milikh and Papadopoulos* [2007] that predicts larger ELF/VLF signal levels for higher *D*-region ionospheric electron densities.

Further studies correlate observed ELF/VLF signal strengths with magnetometer observations [*Rietveld et al.*, 1987; *Jin et al.*, 2009, 2011]. The magnetometer measures near-DC magnetic field fluctuations that are related to the strength of the auroral electrojet currents at $\sim$150 km altitude. *Jin et al.* [2011] integrated magnetometer measurements with riometer absorption and ionosonde electron density measurements and demonstrated correlation between ELF/VLF signal strengths and magnetometer measurements in most cases. *Rietveld et al.* [1983] observed a direct correlation between the ELF/VLF signal amplitude (and polarization) and the auroral electric field strength (and direction) measured using the STARE radar system. *Rietveld et al.* [1984] observed a spatial correlation with STARE observations by tilting the HF beam in different directions, and *Rietveld et al.* [1987] reported a temporal correlation using 32 hours of ELF/VLF, STARE, magnetometer, and riometer observations.

Most of the ELF/VLF generation experiments have been performed at high latitudes ($>$60°N) because of the strong auroral electrojet electric field. However, at equatorial latitudes, the equatorial dynamo current naturally flows in the lower ionosphere. At the Arecibo Observatory (18°N, 66°W) in Puerto Rico and at the Jicamerca (11°S, 76°W) in Peru, successful ELF/VLF signals generation experiments have been performed. The ELF/VLF amplitudes generated at the Arecibo and Jicamerca were 10–100 times smaller than those generated at high latitudes [*Ferraro et al.*, 1982, 1984; *Lunnen et al.*, 1984].

While naturally occurring electric currents are an important part of the ELF/VLF wave generation process, they are not absolutely necessary to generate ELF/VLF signals. Several recent experiments have focused on generating ELF/VLF waves in the absence of a strong auroral electrojet. *Papadopoulos et al.* [2011a,b] showed theoretical and experimental results of the ionospheric current drive (ICD) mechanism, in which F-region pressure was modulated by HF heating. The generated ELF signal ($<$70 Hz) was $\sim$10–20 dB weaker than ELF/VLF waves generated by electrojet modulation. *Eliasson et al.* [2012]'s observation supported the model result by detecting the ELF signals at the further site (330–7700 km) when there was no signal detection directly at the HAARP site. Wave generation with ICD is limited to $<$100 Hz, however. Another electrojet-independent ELF/VLF wave generation mechanism works moderately well at higher frequencies. The "cubic" modulation format was initially thought to beat one HF signal with the second harmonic of a second HF signal. This transmission format was first performed by *Kotik and Ermakova* [1998] broadcasting one beam at $\sim$9 MHz and the other beam at $\sim$4.5 MHz in which the $\sim$9 MHz beam and the second harmonic of the $\sim$4.5 MHz beam differ by a frequency in the ELF/VLF range. *Moore et al.* [2013] performed a similar experiment, but used TOA analysis to determine that the source height resided in the D-region ionosphere. *Moore et al.* [2013] further provided numerical modeling to determine that the dominant "cubic" generation mechanism at high latitudes consists of the beating of one HF signal with the inner product of the first and second HF signal. Observed signal amplitudes were lower than AM electrojet modulation by $\sim$30 dB in the 5 kHz range but only by $\sim$10 dB in the 20 kHz range.

Although mechanisms exist to generate ELF/VLF waves without use of the auroral electrojet currents, at the present time, ELF/VLF wave generation is much more efficient when the electrojet is employed. For the remainder of this dissertation, I focus on techniques to modulate the auroral electrojet currents for ELF/VLF wave generation. I now consider the role that HF transmission parameters play in ELF/VLF wave generation processes.

1.2.2 HF Transmission Parameters

The HF transmission parameters are the only controllable knobs in the ELF/VLF wave generation system. At HAARP, the HF power, frequency, polarization, modulation frequency, and modulation waveform are all precisely controllable. The HAARP HF transmitter is also capable of rapidly scanning the ionosphere. It can re-position the beam with 5 μ-second accuracy, as long as the positions are within 15° of one centralized point. I now discuss the effects these parameters have on ELF/VLF wave generation.

1.2.2.1 HF power

Increasing the power of the HF beam increases the generated ELF/VLF signal strength, although the specific relationship between ELF/VLF amplitude and HF power is non-linear. For instance, *Stubbe et al.* [1982] compared the amplitude produced by AM at 0–50% and 50–100% modulation power depth. The amplitudes would be the same if the ELF/VLF signal strength varied linearly with HF power. The amplitude produced by 0–50% power depth was $\sim$1.5 times larger than the amplitude produced by 50–100% power depth, however. *Moore* [2007] measured the amplitude with different average HF power changing modulation power depth (30–60%) and identified the optimal average HF power. At low HF power levels, researchers generally characterized the relationship with a simple power-law: the ELF/VLF signal amplitude is proportional to the HF power raised to some exponent. *Ferraro et al.* [1984], *Barr et al.* [1987] and *Barr et al.* [1988] used 0.5 for the exponent to model their received signals. *Papadopoulos et al.* [1990] theoretically determined the exponent as <0.5 for low altitudes ($\sim$70–75 km) and as $\sim$2 for higher altitudes ($>$90 km). *Barr and Stubbe* [1991a] observed the ELF/VLF signal with changing HF effective radiated power from 50 MW to 1 GW and fit the power-law equation to the observations. The exponent varied between 0.7 and 0.97 depending on the modulation frequency. *Barr and Stubbe* [1993] applied the power-law to the harmonics of the radiation and determined the exponent as $\sim$0.95.

Despite the excellent match of the observations to the simple power law, at high HF power levels, the power law requires modification to account for observations of saturation effects [*Moore et al.*, 2006].

1.2.2.2 Oblique HF heating

Oblique HF heating of the ionosphere was introduced by *Rietveld et al.* [1984]. *Barr et al.* [1987] and *Barr et al.* [1988] tilted the HF beam from $+37^\circ$ to -37° toward and away from the receiver. They observed $\sim$1–6 kHz signals at $\sim$550 km distant site and showed that tilting the HF beam toward the receiver produced 8–10 dB larger amplitude than tilting the beam away from the receiver. The amplitude changes by a larger degree at higher modulation frequencies. *Barr et al.* [1988] concluded that the amplitude increased or decreased due to the distributed phasing of the ELF/VLF source within the heated region. When tilting the HF beam toward the receiver, the relative phasing of the elemental source components within the heated region produce constructive interference at the receiver. On the other hand, when tilting the HF beam away from the receiver, the relative phasing of the elemental source components produce destructive interference at the receiver. *Cohen et al.* [2010a] presented similar experimental results.

1.2.2.3 Rapid heater beam scanning

By rapidly and repeatedly directing the HF beam toward different positions within the ionosphere, HF transmitters can generate multiple ELF/VLF sources. Due in large part to the relative timing of the transmissions, the sources will have significantly different phases and constitute an ELF/VLF phased array. The simplest phased array is a two-element phased array created by alternatively heating two locations with a CW beam [*Barr et al.*, 1987]. In this case, one location was aimed toward the receiver $\sim$550 km away from Tromsø, whereas the second location was in the opposite direction. The off-zenith angles were symmetrically changed to observe the interference pattern created by the two sources. The received amplitude was approximately doubled when the locations were separated by half of the ELF/VLF wavelength.

Under certain circumstances, each source within the ELF/VLF phased array can be treated independently, and the total received ELF/VLF signal can be estimated as the linear sum of the field generated by these sources. *Gołkowski et al.* [2013] compared observations against a simple model, which indicated that independent treatment of ELF/VLF sources was valid at least up until the HF beams overlapped at the 3-dB point.

Increasing the number of source elements, or equivalently increasing the area of the source has also been shown to be an effective method to increase the ELF/VLF amplitude and efficiency. [*Barr and Stubbe*, 1991a] experimentally showed that the ELF/VLF signal amplitude is proportional to the source area. *Cohen and Gołkowski* [2013] transmitted different HF beam patterns and the broader beam pattern generally produced larger ELF/VLF amplitudes. Two novel HF modulation schemes designed to effectively increase the source area and form the phased array have been suggested and implemented: ”beam painting” and ”geometric modulation.” Both of the techniques involve rapidly scanning the HF beam over a vast area, effectively increasing the area of the ELF/VLF source region.

The beam painting (BP) technique described by *Papadopoulos et al.* [1989] provides a means to increase the area of the ionospheric ELF/VLF source region without significantly affecting the localized conductivity modulation. The modulation technique is implemented by rapidly and repeatedly scanning a vast area of the ionosphere with the HF beam. The rapid heater beam scanning is followed by a cooling period during which the HF transmitter is off, such that the “on” time plus the “off” time corresponds to the desired period of the ELF/VLF wave to be generated. In order for this modulation technique to work as designed, it is necessary that the characteristic time constant for electron heating is significantly shorter than that for electron cooling so that the benefit of a larger heating area more than compensates for the loss associated with a shorter HF heating duration [*Papadopoulos et al.*, 1989, 1990].

Papadopoulos et al. [1989] theoretically simulated the beam painting at 200 Hz modulation frequency. They claimed to determine an optimal ratio of heater “on” to “off” time that would increase the HF-to-ELF conversion efficiency by $\sim$500 times (compared to square-wave AM). This power conversion efficiency was hopeful to outperform the long wire ELF transmitter [*Papadopoulos et al.*, 1990]. However, *Barr and Stubbe* [1991a] and *Barr et al.* [1999] experimentally tested the heating-cooling response of the ionosphere and showed that the minimum ratio of the heating and cooling response was $\sim$0.3 while the BP mechanism required a ratio of 0.05 to achieve the cited efficiency improvement.

Geometric modulation (GM), as implemented by *Cohen et al.* [2008], is a special case of beam painting. During GM, the HF beam scans the ionosphere in a geometric pattern (e.g., a circle or a line), cycling through the pattern at a desired ELF/VLF frequency. *Cohen et al.* [2008] differentiated GM from BP by noting that GM does not have any off time (the HF beam is always at full power) and that GM cycles through the given pattern only once per ELF/VLF period. Similar to BP, GM produces a large distributed ELF/VLF source region, and it has been demonstrated that the resulting source can be treated as an ELF/VLF phased array [*Cohen et al.*, 2010a]. GM is effective at increasing the received ELF/VLF signal amplitude for higher modulation frequencies ($>$3 kHz) and produces a gain of 7–11 dB over vertical AM (square-wave) heating with 50% duty cycle [*Cohen et al.*, 2008, 2010a]. *Cohen et al.* [2010a] also implemented BP, and observed only a few dB enhancement of the amplitude over AM at a nearby site ($\sim$34 km), but no enhancement at farther sites ($\sim$700 km). *Cohen et al.* [2010b]'s model result showed that BP was not effective because even HAARP's achievable HF power was not sufficient to increase the electron temperature quickly enough to take advantage of BP. Nevertheless, differentiation between the BP and GM techniques is mere nomenclature: the basic physical concepts guiding the two methods are the same.

The BP and GM experiments highlight the primary factors that contribute to the ELF/VLF signal amplitudes generated using a phased array, which are: the HF heated area, the duty cycle, the spatial distribution of phase, and the obliqueness of the HF beam. These four factors have not been treated systematically in the past studies, and their effects compete with each other. This dissertation optimizes the received ELF/VLF amplitude by properly accounting for these competing effects.

1.2.2.4 Other HF transmission properties

This section summarizes effects of other important HF transmission properties. First, HF frequency is discussed. The HAARP HF transmitter can broadcast between 2.7 and 9.5 MHz. Within that range, lower HF frequencies experience a larger rate of absorption within the *D*-region ionosphere [*James*, 1985]. For instance, *Cohen et al.* [2012a] compared the received ELF/VLF amplitudes produced by a narrow beam at 3.25 MHz and a broad beam at 9.50 MHz, both of which had roughly the same HF power density. The observation showed the narrow 3.25 MHz beam produced 5–10 dB larger amplitude than the broad 9.50 MHz beam.

HF beam polarity, X- or O-mode, also produces a difference in the received ELF/VLF signal amplitude. It is generally consistent that X-mode generates 4–8 dB larger received ELF/VLF amplitude than O-mode [*Stubbe et al.*, 1982; *Ferraro et al.*, 1984; *James et al.*, 1984; *Villascfior et al.*, 1996; *Barr et al.*, 1999] because the X-mode wave counteracts the natural direction of electron motion around the Earth's magnetic field, and in turn, experiences a larger rate of absorption.

The modulation waveform is also an important factor to consider. The most common waveform is the square-wave waveform for which the duty cycle can be controlled precisely. The ELF/VLF amplitude increases with increasing duty cycle up to 20–40% and decreases at higher duty cycles [*Barr and Stubbe*, 1991b; *Cohen et al.*, 2010a; *Jin et al.*, 2012]. This trend is due to the fact that the ionospheric heating time constant tends to be larger than the cooling time constant [*Barr and Stubbe*, 1991b]. *Jin et al.* [2012] experimentally compared the amplitude generated by 2125 Hz modulation for square wave, sine wave, and sine-like optimal waveform (an inverted waveform designed to minimize the generation of harmonics). The experimental results indicated that the square wave modulation at 40% duty cycle generated the largest amplitude and that the square wave at 20% duty cycle was the most efficient. *Barr and Stubbe* [1991b] found that the efficiency of square wave modulation was slightly different, however. While 20% duty cycle was the most efficient at 510 Hz, at 2010 Hz and 6010 Hz the efficiency monotonically decreased with increasing duty cycle. There have been other waveforms transmitted for the ELF/VLF wave generation such as the square-root-sinusoid and triangle waveforms. These waveforms have not been analyzed from the aspect of efficiency improvement [*Cohen*, 2009; *Agrawal and Moore*, 2012].

Having summarized the effects of ionospheric and geomagnetic conditions, as well as the effects of various HF transmission parameters on the received ELF/VLF signal amplitude, I now progress to discuss analysis techniques.

1.3 Analysis Techniques

Two primary effects must be considered in order to properly analyze ELF/VLF signals observed on the ground: 1) the formation of the ionospheric ELF/VLF current source by HF heating, and 2) the propagation of the radiated ELF/VLF signal within the Earth-Ionosphere waveguide. Conventionally, two separate models are employed to predict the ELF/VLF source formation and the Earth-ionosphere waveguide propagation to test the understanding of source and waveguide effects [e.g., *Barr et al.*, 1987; *Rietveld et al.*, 1987; *Moore et al.*, 2007; *Cohen et al.*, 2012b; *Gołkowski et al.*, 2013]. Although propagation properties within the Earth-ionosphere waveguide are highly variable and frequency dependent, they cannot be directly controlled; as a result, ELF/VLF wave generation efficiency studies focus on controlling the properties of the ionospheric ELF/VLF current source. Carefully designed experiments are required to distinguish between propagation effects and source effects.

A multitude of works successfully compare ELF/VLF observations to model predictions. Due to the complexity of the models and their dependence of the ionospheric parameters (which can vary widely, and are largely unknown), however, it is more desirable to experimentally isolate the two contributions in order to simplify the modeling and to make the experimental measurement more physically meaningful. This dissertation introduces and rigorously applies ELF/VLF time-of-arrive (TOA) analysis to separate ELF/VLF source effects from waveguide propagation effects. In the following sections, I review past experimental and analytical efforts related to this topic.

1.3.1 Neutralization of Waveguide Propagation Effects

Because ELF/VLF propagation within the Earth-ionosphere waveguide is highly dependent on frequency, it is difficult to derive ELF/VLF source properties based on observations at different frequencies. For instance, depending on the ELF/VLF frequency employed, the amplitude of the second harmonic may be observed to be larger than that of the fundamental. Under normal circumstances, this is a waveguide propagation effect, with the frequency of the second harmonic approaching one of the waveguide resonances. One possible way to neutralize the effect of the waveguide is to normalize the received field or to compare it against a reference signal. For example, *Barr and Stubbe* [1993] investigated the harmonics generated during ELF/VLF wave generation experiments. They normalized the amplitude of the third harmonic (at 3 kHz, generated using a 1 kHz fundamental frequency, for instance) to the amplitude of the fundamental frequency (at 3 kHz, generated using a 3 kHz fundamental frequency). The two transmissions were closely spaced in time in order to avoid complications arising from a temporally changing ionosphere or the temporally changing strength of the electrojet current. The normalized frequency content of the radiated ELF/VLF wave nearly exactly matched the normalized frequency content of the transmitted modulation waveform *Barr and Stubbe* [1993]. The harmonic ratio was used to calculate heating and cooling time constants as well as the power law index of HF-to-ELF/VLF conversion. *Moore and Agrawal* [2011] and *Agrawal and Moore* [2012] also normalized their observation by supplying a reference signal at the same frequency. These cases successfully investigated multi-HF beam heating under different power settings. The normalization was used to cancel waveguide and electrojet strength variations with time. It was determined that continuous HF heating (in addition to modulated heating) suppresses the received ELF/VLF amplitude and the degree of suppression as a function of power was used to estimate electron densities in the *D*-region ionosphere.

1.3.2 Pulsed HF Heating

Pulsed HF heating experiments provide another means to isolate the ELF/VLF source effects from waveguide effects. *Stubbe et al.* [1982] transmitted square pulses and observed the first ionosphere response at 0.7–0.8 ms followed by weak signals for ∼2 ms. The first signal was interpreted as line-of-sight (LOS) propagation from the ionosphere to the receiver, whereas the following signals were interpreted as ionospherically reflected (IR) signals. The observation of the pulse in the time domain separates the LOS signal from the IR signals and is advantageous to simplify the model – without the Earth-Ionosphere reflections. Using this advantage, *Rietveld et al.* [1986] characterized the heating and cooling time constants with an exponential heating model. Similarly, *Papadopoulos et al.* [2005] compared the LOS component of pulsed heating observations against a conductivity modulation model and used a 3-D Green's function to calculate the temporal evolution of magnetic fields.

While there is certainly utility in pulsed HF heating experiments, the experimental observations represent only the initial reaction of the ionosphere to HF heating. For ELF/VLF wave generation, the sinusoidal steady-state solution is the desired observation. The ELF/VLF TOA analysis presented in this dissertation provides the desired sinusoidal steady-state solution.

1.3.3 Phase versus Frequency

A simplified version of the TOA analysis method discussed in Chapter 2 consists of estimating the group delay of the received ELF/VLF signal by differentiating the received signal phase with frequency. *Stubbe et al.* [1981] and *Rietveld et al.* [1989] applied this method to determine the group delay (as a function of modulation frequency) of the ELF/VLF signal generated using a linear frequency-time modulation format. Using the calculated group delays, they estimated ELF/VLF source heights that varied rapidly as a function of frequency between 60 and 130 km. The largest fluctuations occurred near Earth-ionosphere waveguide resonances. It is likely that these fluctuations occurred because simply differentiating the phase with frequency does not isolate the LOS and ionospherically-reflected signal components. *Riddolls* [2003] applied essentially the same method to the ELF/VLF harmonics generated during the HF heating process, and found similar results. In the context of this dissertation, the effective source altitudes determined by *Stubbe et al.* [1981], *Rietveld et al.* [1989], and *Riddolls* [2003] are contaminated by ionospherically reflected signal components.

1.3.4 Time of Arrival Analysis

The time of arrival analysis presented herein provides a means to isolate LOS and IR signal components. The analysis produces bandwidth-averaged amplitude, phase, and propagation delay measurements. In Chapter 2, we demonstrate that this decomposition provides an accurate measurement of the ELF/VLF source phase, and in Chapters 3, 4, and 5, we demonstrate how this knowledge can be used to optimize the ELF/VLF signal amplitude received at an individual receiver site. Similar analysis techniques can be used to optimize ELF/VLF excitation of the Earth-ionosphere waveguide or to optimize ELF/VLF injection into space, assuming high frequency resolution TOA analysis can be provided. The combination of high frequency resolution and TOA analysis is beyond the scope of this dissertation. Nevertheless, the ability to derive information regarding ELF/VLF source phase distribution and the ability to manipulate that distribution is of critical importance to all three goals. Through the application of TOA analysis, this dissertation demonstrates both capabilities.

1.4 Scientific Contributions

The scientific contributions of this dissertation are as follows:

1. The ELF/VLF time-of-arrival (TOA) analysis method is introduced as an effective means to separate line-of-sight (LOS) signal components from ionospherically-reflected (IR) signal components received at an individual ELF/VLF receiver. It is demonstrated that TOA analysis identifies the maximum altitude of the dominant ELF/VLF source generated by modulated HF heating. By separating the the multi-path signal components, the ELF/VLF source effects are successfully separated from Earth-Ionosphere waveguide propagation effects.

2. Using TOA analysis, the parameters that affect ELF/VLF waves generated using beam painting (BP) and geometric modulation (GM) are experimentally quantified for the first time. By decomposing the spatial distribution of the ELF/VLF source, the HF heating area is identified as the most important effect on received ELF/VLF amplitude. Conversely, the distribution of source phasing is identified as the effect most detrimental to the ELF/VLF amplitude. Based on the experimental observations, simple modifications to the spatial heating pattern are suggested to increase the received ELF/VLF amplitudes.

3. The effect of modulation duty cycle on ELF/VLF wave generation is quantified as a function of source location. It is determined that perceived heating and cooling rates derived from these measurements are dependent upon the source location relative to the receiver location.

4. A method to optimize the HF beam painting pattern, maximizing the ELF/VLF signal amplitude at a given receiver location, is demonstrated. The optimization incorporates experimental observations made for 8 heating locations and accounts for the effective duty cycle, source area, and source phasing.

CHAPTER 2
ELF/VLF WAVE GENERATION MECHANISM AND THE TOA METHOD

This chapter reviews the basic physical mechanism for ELF/VLF wave generation by modulated HF heating of the ionosphere and describes how it is adapted to the TOA technique that will be used throughout this dissertation. The important physical processes and HF heating parameters are discussed to provide a context within which interpret the TOA measurements. In addition, the TOA timing accuracy and resolution are discussed together with physical and mathematical limitations.

2.1 ELF/VLF Wave Generation Mechanism

The cartoon diagram shown in Figure 2-1 depicts the process of ELF/VLF wave generation by HF heating of the lower ionosphere. At HAARP, using the 12×15 element array with 3.6 MW input power, an HF broadcast for ELF/VLF wave generation typically has a center frequency of $\sim$3–6 MHz, an ERP of 0.1–1 GW, and illuminates an area of $\sim$25 km by $\sim$20 km at $\sim$80 km altitude. As the HF wave propagates upward, it interacts with the ionosphere, and the wave energy is absorbed between $\sim$60–100 km altitude, the so-called *D*-region. The wave absorption is significant in the *D*-region due to the high collision frequency ($\sim$1 MHz). The physical process of ELF/VLF wave generation is broken up into several parts: HF wave propagation and absorption in the *D*-region ionosphere, the modulation of ionospheric conductivities, the modulation of the auroral electrojet currents at ELF/VLF frequencies, and the resulting radiation of ELF/VLF waves.

2.1.1 The Ionosphere

The ionosphere is a plasma medium containing electrons, ions, and neutral particles which are ionized by the radiated energy from the sun. The structure of the ionosphere from 80 km to 400 km is shown in Figure 2-2. The distributions of ionospheric constituents are provided by ionospheric models: the International Reference Ionosphere (IRI) and MSIS-E-90 Atmosphere Model for the ionized and neutral particles. These data are available online [*Bilitza*, 2012]. The ionospheric structure varies as a function of time (e.g, day or night), season (e.g, summer or winter), and

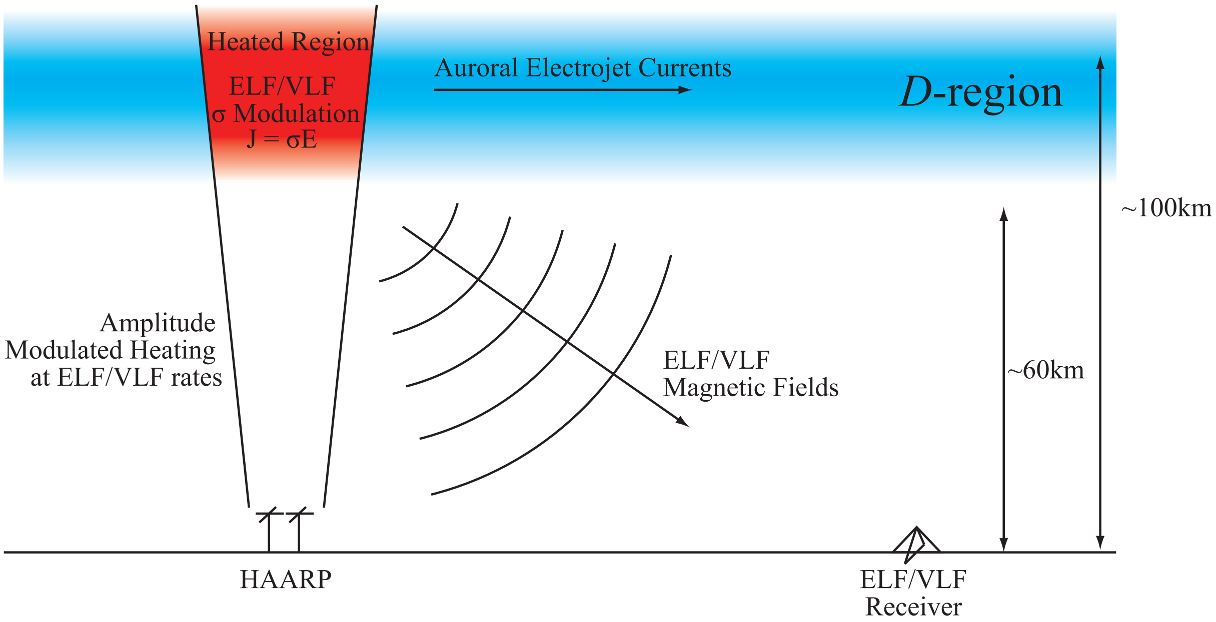

Figure 2-1. A cartoon diagram of the ELF/VLF wave generation mechanism.

location (e.g, latitude and longitude). The structure shown in the Figure 2-2 is for 8 October 2002 at 12:00 UT at coordinates 62° North and 145° West. This location corresponds to HAARP's location at a local time of 3:00 am. Figure 2-2(a) includes the densities of electrons, neutral molecules, and neutral atoms. The electron, neutral, and ion temperatures are shown in the Figure 2-2(b).

The regions of the ionosphere are typically classified as the *D*-region (50–90 km), the *E*-region (90–140 km), and the *F*-region (above 150 km) [*Davies*, 1990], although these definitions are not strict. Generally speaking, the *F*-region has the highest electron concentration and temperature because it is affected most by the sun's radiation. At lower altitudes, the electron density decreases. On the other hand, densities of neutral molecules and neutral atoms increase at the lower altitudes resulting in the *D*-region being a high collisional region.

The electron-neutral and electron-ion collision frequencies are shown in Figure 2-2(c) together with the total of the two collision frequencies. These values are calculated from the data shown in Figure 2-2(a) and (b) using a simple model [*Ratcliffe*, 1959]. Electrons collide with heavy particles such as ions, molecules, and atoms; because of these collisions, the wave is absorbed as it propagates through the collisional plasma medium. At higher altitudes, the total collision

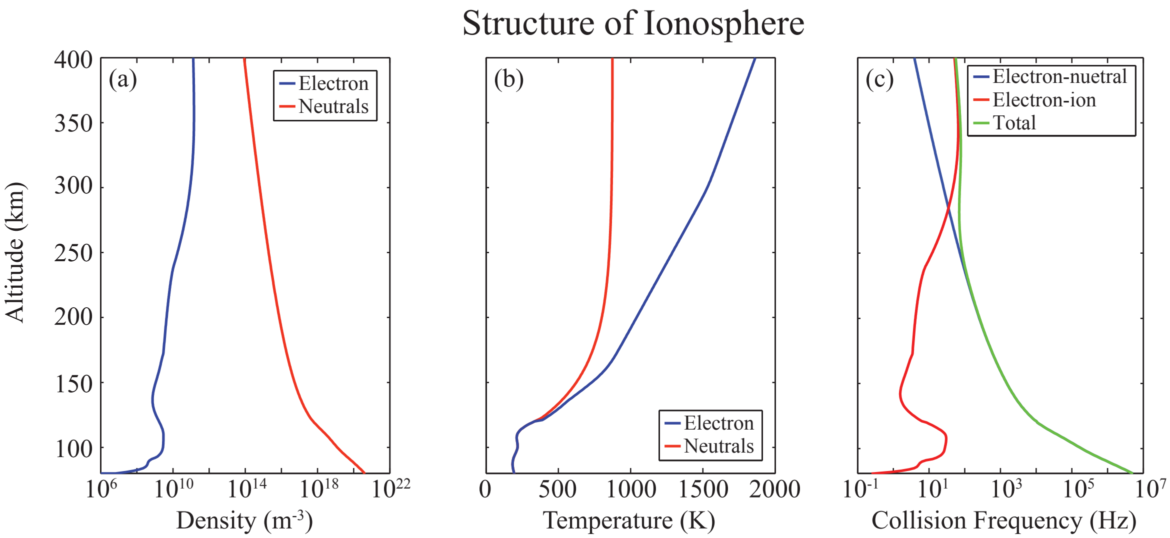

Figure 2-2. (a) Density of electrons and neutral particles, (b) Electron and neutral temperature, (c) Electron-neutral, electron-ion, and total collision frequencies.

frequency is dominated by electron-ion collisions, whereas in the *D*-region ionosphere, electron-neutral collisions dominate.

2.1.2 Refractive Index

The refractive index, n, determines the rate of absorption within the *D*-region ionosphere. With the refractive index, a general solution of the wave equation takes the phasor form of (in the case of E-field propagating in the positive z direction),

$$E = E_0 e^{-jn\beta_0 z} e^{j\omega t} \tag{2–1}$$

where E_0 is the amplitude of the electric field, β_0 is the free-space wave number, and ω is the angular frequency of the wave. The refractive index can take a complex form, defined as $n = \mu - j\chi$. By substituting the complex form of the refractive index in to Equation 2–1, it becomes,

$$E = E_0 e^{-\chi\beta_0 z} e^{-j\mu\beta_0 z} e^{j\omega t} \tag{2–2}$$

The fields are thus attenuated along the direction of propagation due to the imaginary part of the refractive index. In turn, the wave power is absorbed by the medium that the wave propagates through. The refractive index is determined by the Appleton-Hartree equation [*Ratcliffe*, 1959],

$$n^2 = 1 - \frac{X}{1 - jZ - \frac{Y^2 \sin^2\Theta}{2(1-X-jZ)} \pm \sqrt{\frac{Y^4 \sin^4\Theta}{4(1-X-jZ)^2} + Y^2\cos^2\Theta}} \tag{2–3}$$

where the sign of the radical in the denominator determines the mode of propagation: $+$ is for the ordinary mode (O-mode), and $-$ is for the extraordinary mode (X-mode). Θ is the angle between the wave k-vector and the Earth's magnetic field, and

$$X = \frac{\omega_N^2}{\omega^2}, \quad Y = \frac{\omega_{ce}}{\omega}, \quad Z = \frac{\nu}{\omega} \tag{2–4}$$

where ω_N is the plasma frequency, ω_{ce} is the gyrofrequency, ω is the angular frequency of the wave, and ν is the collision frequency. Individually, ω_N and ω_{ce} are defined:

$$\omega_N^2 = \frac{N_e q_e^2}{\varepsilon_0 m_e} \quad \text{and} \quad \omega_{ce} = \frac{B|q_e|}{m_e} \tag{2–5}$$

where N_e is the electron density, q_e is the electron charge, ε_0 is the permittivity in free space, m_e is the electron mass, and B is the magnitude of the Earth's magnetic field. Using the electron density shown in Figure 2-3, ω_N is on the order of 5×10^6 rad/s (0.8 MHz) for the D and E region, and 5×10^7 rad/s (8 MHz) for the F region. Meanwhile, ω_{ce} is on the order of 9.5×10^6 rad/s (1.5 MHz) where the Earth magnetic field is $\sim 50\ \mu T$.

The refractive index is calculated using Equation 2–3 for a 3 MHz X-mode HF wave. The results are shown on log scale in Figure 2-3, where the real part of the refractive index remains close to 1 in the D and E-regions, implying that the HF wave propagates through without significant reflection. In this electron density profile, the refractive index goes to 0 and reflects the HF wave at ~245 km (not shown). Meanwhile, the imaginary part of n is largest at ~90 km altitude and decreases at higher altitudes, indicating that most of the absorption occurs in the D-region.

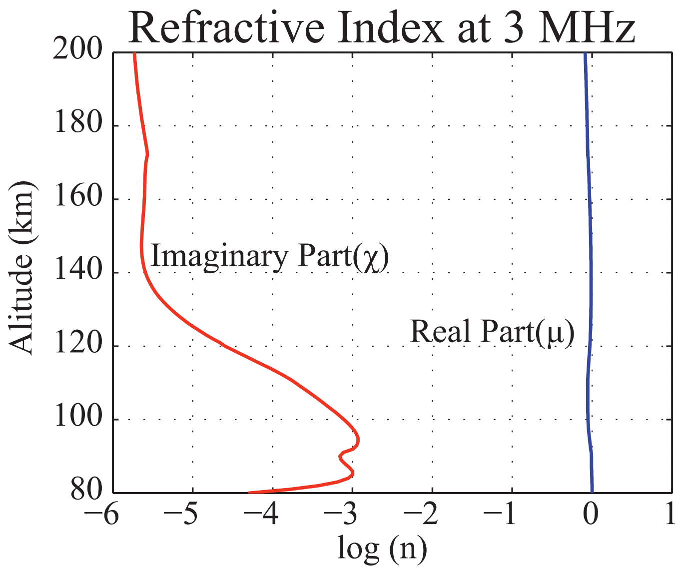

Figure 2-3. Real and imaginary components of the refractive index, *n*.

The absorbed HF waves energize the electrons and can increase their temperatures well beyond ∼1000 K. It is this heating process which enables the modulation of ionospheric conductivities.

2.1.3 Ionospheric Conductivity Modification

The ionosphere is an anisotropic medium due to the presence of the Earth's magnetic field, and the conductivity is represented as a tensor. The conductivity tensor can be expressed as:

$$\bar{\bar{\sigma}} = \begin{bmatrix} \sigma_P & -\sigma_H & 0 \\ \sigma_H & \sigma_P & 0 \\ 0 & 0 & \sigma_{||} \end{bmatrix} \tag{2–6}$$

where (when the collision frequency, ν, is constant):

$$\sigma_P = \frac{N_e q_e^2}{m_e}\left[\frac{\nu}{\nu^2+\omega_H^2}\right] \tag{2–7}$$

$$\sigma_H = \frac{N_e q_e^2}{m_e}\left[\frac{\omega_H}{\nu^2+\omega_H^2}\right] \tag{2–8}$$

$$\sigma_{||} = \frac{N_e q_e^2}{m_e \nu} \tag{2–9}$$

σ_P, σ_H, and $\sigma_{||}$ denote the Pedersen, Hall, and parallel conductivities, respectively. Using the electron density profile in Figure 2-2, σ_P is on the order of 1×10^{-7} S/m, and σ_H and $\sigma_{||}$ are on the order of 1×10^{-6} S/m.

The conductivities are dependent on the collision frequency, ν, and we assume $\nu \propto$ energy. The ionospheric conductivities are thus modified by changes in electron temperature. Equations 2–7 – 2–9 are derived assuming a constant ν, however. Accounting for an energy-dependent ν, the ionospheric conductivities are, as expressed by *Tomko* [1981]:

$$\sigma_P = \frac{4\pi}{3} j \frac{q_e^2}{m_e \omega} \int_0^\infty \frac{U}{U^2 - Y^2} v_e^3 \frac{\partial f_{e,0}}{\partial v_e} dv_e \tag{2–10}$$

$$\sigma_H = \frac{-4\pi}{3} j \frac{q_e^2}{m_e \omega} \int_0^\infty \frac{U}{U^2 - Y^2} v_e^3 \frac{\partial f_{e,0}}{\partial v_e} dv_e \tag{2–11}$$

$$\sigma_{||} = \frac{4\pi}{3} j \frac{q_e^2}{m_e \omega} \int_0^\infty \frac{1}{U} v_e^3 \frac{\partial f_{e,0}}{\partial v_e} dv_e \tag{2–12}$$

where U is $1 - jZ$, v_e is the electron thermal velocity where ν is proportional to v_e^2, and $f_{e,0}$ is the electron energy distribution function, which we assume remains Maxwellian throughout the heating process. The ionospheric conductivities are modified by heating the *D*-region ionosphere with HF waves. If the HF signal is modulated at an ELF/VLF rate, the ionospheric conductivities are modulated according to that rate. In the next section, I discuss the ELF/VLF source created by the modulated ionospheric conductivity.

2.1.4 ELF/VLF Source Currents

In the presence of an external electric field, the conductivities that are modified by HF heating form an ELF/VLF current source. The relationship is expressed by Ohm's law:

$$\bar{J} = \bar{\bar{\sigma}} \bar{E} \tag{2–13}$$

where $\bar{J}$ is the current density, $\bar{\bar{\sigma}}$ is the conductivity tensor, and $\bar{E}$ is the external electric field.

The modulated conductivities thus create an oscillating ELF/VLF current density, J. In the polar regions, where ELF/VLF experiments are typically performed, the electric field exists in the ionosphere as the so-called auroral electrojet electric field. The typical strength of the electric field is on the order of 5-100 mV/m [*Baumjohann*, 1982; *Payne et al.*, 2007]. The resulting ELF/VLF current density serves as an ELF/VLF source that radiates an electromagnetic wave [*Balanis*, 1989]. This dissertation is primarily concerned with the generated ELF/VLF magnetic flux density B. To find the expression of the magnetic flux density, I start with forming the ELF/VLF current source, J, shown in Equation 2–13. Equation 2–13 is expanded in a matrix form,

$$\begin{bmatrix} J_x \\ J_y \\ J_z \end{bmatrix} = \begin{bmatrix} \Delta\sigma_P & -\Delta\sigma_H & 0 \\ \Delta\sigma_H & \Delta\sigma_P & 0 \\ 0 & 0 & \Delta\sigma_{||} \end{bmatrix} \begin{bmatrix} E_x \\ E_y \\ E_z \end{bmatrix} \tag{2–14}$$

where $\Delta\sigma_H$ is the modulated Hall conductivity, $\Delta\sigma_P$ is the modulated Pedersen conductivity, and $\Delta\sigma_{||}$ is the modulated parallel conductivity. From Figure 2-4, E_x and E_y are described by the magnitude and direction, that is

$$\begin{aligned} E_x &= |E|\, sin\theta \\ E_y &= |E|\, cos\theta \end{aligned} \tag{2–15}$$

Thus, the modulated elecrojet current becomes

$$\begin{bmatrix} J_x \\ J_y \\ J_z \end{bmatrix} = \begin{bmatrix} \Delta\sigma_P\,|E|\, sin\theta - \Delta\sigma_H\,|E|\, cos\theta \\ \Delta\sigma_H\,|E|\, sin\theta + \Delta\sigma_P\,|E|\, cos\theta \\ \Delta\sigma_{||} E_z \end{bmatrix} \tag{2–16}$$

The current source, J, is a horizontal dipole due to the lack of contribution of J_z because $E_z = 0$. If we account only for the LOS signals with an image source over the Earth's ground and assume that the Earth's ground is a perfect conductor, the image source, J_{imag}, is

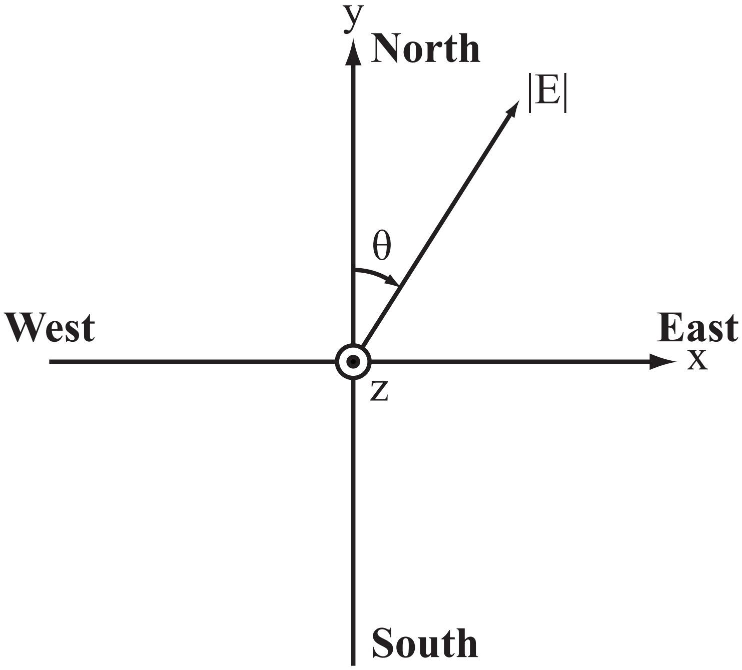

Figure 2-4. North-South and East-West coordinates mapped onto x and y coordinates. $|E|$ is the electrojet electric field magnitude, and θ is the elecrojet electric field direction relative to North. The $+z$ direction (out of the page) coincides with increasing altitude.

$$J_{imag} = -J \tag{2–17}$$

J_{imag} is located at the opposite side to the real source over the ground plane and is equally distanced.

The radiated magnetic field including the image source is expressed as, [*Balanis*, 1989, p. 283]

$$B_x = \frac{\mu}{4\pi}\int_V \left[\left(z-z'\right)J_y - \left(z+z'\right)J_{y,imag}\right]\frac{1+j\beta_0 R}{R^3}e^{-j\beta_0 R}dv' \tag{2–18}$$

$$B_y = \frac{\mu}{4\pi}\int_V \left[-\left(z-z'\right)J_x + \left(z+z'\right)J_{x,imag}\right]\frac{1+j\beta_0 R}{R^3}e^{-j\beta_0 R}dv' \tag{2–19}$$

$$B_z = \frac{\mu}{4\pi}\int_V \left[\left(y-y'\right)\left(J_x+J_{x,imag}\right) - \left(x-x'\right)\left(J_y+J_{y,imag}\right)\right]\frac{1+j\beta_0 R}{R^3}e^{-j\beta_0 R}dv' = 0 \tag{2–20}$$

where $J_{x,imag}$ and $J_{y,imag}$ are the image current densities for x and y direction, β_0 is the wave number, z is the location of the observation, z' is the location of the source, R is the distance between the source and an observation point, and v' is the volume of the source to integrate. If the source is located at the height, h, with the effective volume of ΔV, the horizontal magnetic field observed at the ground is expressed as, by expanding Equation 2–18 with Equation 2–19,

$$B_x = -\frac{\mu}{2\pi} h J_y \frac{1 + j\beta_0 R}{R^3} e^{-j\beta_0 R} \Delta V \tag{2–21}$$

$$B_y = -\frac{\mu}{2\pi} h J_x \frac{1 + j\beta_0 R}{R^3} e^{-j\beta_0 R} \Delta V \tag{2–22}$$

$$B_z = 0 \tag{2–23}$$

Inserting Equation 2–16 to Equation 2–21 and 2–22 yields,

$$B_x = -\frac{\mu h_H}{2\pi} \Delta\sigma_H |E| sin\theta \frac{1 + j\beta_0 R_H}{R_H^3} e^{-j\beta_0 R_H} \Delta V - \frac{\mu h_P}{2\pi} \Delta\sigma_P |E| cos\theta \frac{1 + j\beta_0 R_P}{R_P^3} e^{-j\beta_0 R_P} \Delta V \tag{2–24}$$

and

$$B_y = \frac{\mu h_P}{2\pi} \Delta\sigma_P |E| sin\theta \frac{1 + j\beta R_P}{R_P^3} e^{-j\beta_0 R_P} \Delta V - \frac{\mu h_H}{2\pi} \Delta\sigma_H |E| cos\theta \frac{1 + j\beta R_H}{R_H^3} e^{-j\beta_0 R_H} \Delta V \tag{2–25}$$

where h_H and h_P are the source heights of the modulated Hall and Pedersen conductivities, R_H and R_P are the distance between the source of the conductivity modulation and the observation point for Hall and Pedersen. Using the coordinate in Figure 2-4, B_x and B_y are measured by North-South (NS) and East-West (EW) antenna respectively. Due to the two different sources of the modulated Hall and Pedersen conductivities, and the direction of the electrojet electric field, NS and EW observations are expected to be somewhat different.

The TOA measurement is not able to discern the sources of the modulated Hall and Pedersen conductivities due to the limited time resolution, although it is an interesting problem that may be resolved in the future. The TOA measurement indicates the combined effects of the two sources, however, it is likely dominated by the modulated Hall conductivity modulation. The past literatures have shown that the Hall conductivity modulation dominates the Pedersen modulation in ground-based observations [*Rietveld et al.*, 1986; *Moore*, 2007]. Throughout the observations of this dissertation, the TOA measurement assumes one effective ELF/VLF source.

The equations above describe a magnetic field over an ground plane that propagates directly from the source, the so-called line-of-sight (LOS) path. This signal is typically the largest component of the TOA measurement for receivers within $\sim$200 km of HAARP. Other components not expressed above are called ionospherically reflected signals, which reflect at the Earth's ground and the *D*-region ionosphere and reaches the VLF antenna on the ground. The TOA method separates these signals by their difference in arrival time, allowing us to simply model the LOS signal and focus on ELF/VLF source excitation. While the sum of all ionospherically reflected components represents the effects of the Earth-Ionosphere waveguide, the LOS signal component is considered to be independent of the Earth-ionosphere waveguide. Although this dissertation focuses on the LOS signal component, it is important to review the ionospheric wave reflection process for better understanding of the TOA measurement.

2.1.5 ELF/VLF Reflection in the *D*-region Ionosphere

It is well known that ELF/VLF waves reflect at an altitude of $\sim$60–100 km in the *D*-region ionosphere and propagate between the ionosphere and the ground [e.g, *Lewis et al.*, 1973; *Rietveld et al.*, 1986]. The reflection process is complicated given the large ELF/VLF wavelength and the slowly varying ionospheric medium. In this section, I roughly estimate the reflection height using the refractive index given in Equation 2–3 as introduced in [*Ratcliffe*, 1959].

One of conditions where the reflection of a vertically incident wave occurs is that the refractive index, n, is equal to zero. When the refractive index is equal to zero, the wave field can not propagate because it becomes an evanescent wave (Equation 2–2). At 10 kHz, the refractive index is zero at an altitude of $\sim$120 km. However, when $Z \gg 1$ (Equation 2–4), the reflection occurs due to a rapid change of the imaginary part of the refractive index, χ, below the altitude where $\mu = 0$.

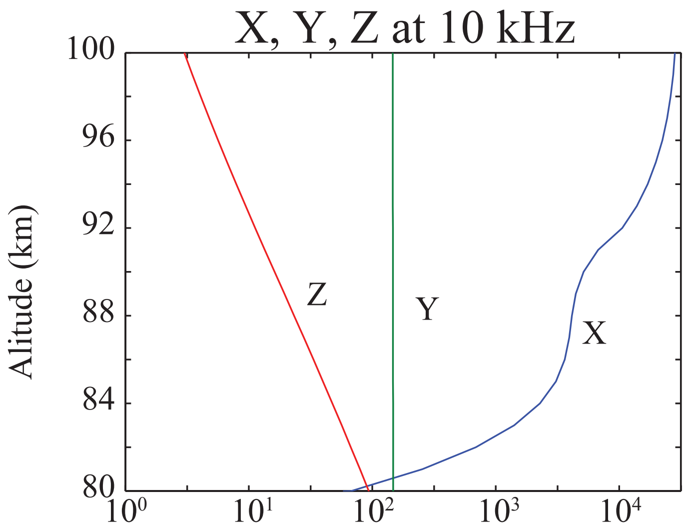

Figure 2-5. Plasma parameters at 3 kHz.

The rapid change occurs at an altitude where $X \approx Z$. The ionosphere acts like a dielectric below that the altitude and a conductor above that altitude. At 10 kHz, $X \approx Z$ at an altitude of $\sim$82 km, as shown in Figure 2-5.

2.2 ELF/VLF Time-of-Arrival (TOA) Analysis Method

The goal of the TOA method is to estimate the amplitude and phase of ELF/VLF waves arriving at the receiver as a function of time in such a way as to reveal characteristics of the ELF/VLF wave source region. As *Payne et al.* [2007] demonstrated, this is not possible using a single-tone modulation frequency. Instead, we utilize a frequency-time ramp modulation format, typically, from 1 kHz to 5 kHz over 4 seconds. This type of signal is broadly known as Frequency Modulated Continuous Wave (FMCW) in radar applications [e.g., *Barrick*, 1973; *Schuster et al.*, 2006] and is commonly referred to as “chirp” modulation.

This particular modulation format is selected due to the relatively simple analysis that results. The linear frequency-time ramp has an approximately flat response in the frequency domain. Also, because the received signal is between $\sim$1–5 kHz, the combined effects of conductivity modulation and LOS propagation is expected to have an approximately flat frequency response. The conductivity modulation decreases with the reciprocal of the modulation frequency after $\sim$1.5 Hz [*Stubbe* *et al.*, 1985], and LOS propagation (Equation 2–21) increases as the modulation frequency increases. These two effects essentially cancel to provide the flat response. The bandwidth of the ramp is chosen to be broad enough to extract the LOS signal in the presence of ionospherically reflected signals.

The bandwdith of the frequency ramp is chosen to be around or broader than 4 kHz in order to separate the multipath components. The time resolution as a function of bandwidth is discussed in Section 2.3.2. The FMCW waveform can be replaced by Frequency Stepped Continuous Wave (FSCW) as long as the reciprocal of the frequency interval is much greater than the propagation delays. The greater the number of frequency steps taken, the more robust the system is to noise. To maximize the noise performance, this dissertation focuses on the FMCW chirp.

The time-dependence of the modulation frequency provides a means to differentiate between signals arriving at different times: the impulse response of the system may be directly calculated from the observations, providing a time-domain estimate of the multi-path propagation delays and other signal properties. It should be noted at this point that the ELF/VLF wave generation process is inherently nonlinear, whereas the TOA analysis method presented is linear. For instance, ELF/VLF harmonics at modulation frequencies that are not transmitted are regularly observed in ELF/VLF recordings. The implementation of the TOA analysis first separates the received ELF/VLF harmonics and considers them individually. Additionally, because ELF/VLF wave generation is nonlinear with HF power and significantly varies with HF frequencies and polarizations, it is expected that the calculated impulse response applies only for a given HF power, frequency, and polarization. Lastly, because different modulation waveforms produce different harmonic content when driving the ionospheric conductivity modulation, we do not expect the calculated impulse to apply to all modulation waveforms. Instead, the intent is to interpret a given TOA impulse response to yield information about the ELF/VLF source region for a given set of transmission parameters.

I begin by expressing the time-averaged Poynting flux of the HF transmission as the sum of harmonic components:

$$\langle P(t)\rangle = \sum_n \langle P_n(t)\rangle = \sum_n A_n \cos\left(2\pi n\left(f_0 t + \frac{\Delta f}{2}t^2 + \phi_{0n}\right)\right) \tag{2–26}$$

where $\langle P_n(t)\rangle$ represents the time-averaged Poynting flux of the n^{th} harmonic, f_0 is the initial frequency of the ramp, and Δf is the slope of the frequency-time ramp. A_n and ϕ_{0n} are the amplitude and phase of the n^{th} harmonic, both of which are assumed to be constant with frequency in this work.

For a given harmonic, the received signal may be expressed as:

$$r_n(t) = \langle P_n(t)\rangle * g_n(t) * p(t) = \langle P_n(t)\rangle * h_n(t) \tag{2–27}$$

where $g_n(t)$ is the effective impulse response converting HF power to ionospheric current modulation for the n^{th} harmonic, $p(t)$ is the impulse response characterizing ELF/VLF wave propagation to the receiver, and $*$ denotes convolution. TOA analysis finds $h_n(t)$, the effective impulse response combining the effects of current generation and wave propagation for a given harmonic.

The total received ELF/VLF signal, $R(t)$, may thus be expressed as:

$$R(t) = \sum_n \left\{A_n \cos\left(2\pi n\left(f_0 t + \frac{\Delta f}{2}t^2\right) + \phi_{0n}\right) \sqcap(t/T - 1/2) * h_n(t)\right\} \sqcap(t/T - 1/2)\text{Ш}(F_s t) \tag{2–28}$$

where T is the duration of the frequency-time ramp, F_s is the sample frequency of the data acquisition system, and $\sqcap$ and Ш are defined as:

$$\sqcap(t) = \begin{cases} 1 & |t| < \frac{1}{2} \\ 0 & |t| > \frac{1}{2} \end{cases} \tag{2–29}$$

$$\text{Ш}(t) = \sum_{n=-\infty}^{\infty} \delta(t-n) \tag{2–30}$$

The processing of the n^{th} harmonic begins by mixing-down and filtering the received signal. The mixing kernel for the n^{th} harmonic may be expressed as:

$$m_n(t) = e^{-j2\pi n\left(f_0 t + \frac{\Delta f}{2}t^2\right)} \sqcap(t/T - 1/2) \tag{2–31}$$

$b(t)$ is, typically, the 100-Hz bandwidth low-pass filter, implemented using a 2000-tap, 8^{th}-order Kaiser window. After applying the low pass filter, $b(t)$, the base-band signal is mixed-up to its original frequency range using the complex conjugate of $m_n(t)$, and the real component of the resulting complex-valued signal represents the isolated n^{th} harmonic.

The isolated n^{th} harmonic of the frequency-time ramp, $y_n(t)$, may then be described:

$$y_n(t) = \Re\left\{\left[(R(t)m_n(t)) * b(t)\right] m_n^*(t)\right\} \tag{2–32}$$

The impulse response, $\tilde{h}_n(t)$ (complex form of $h_n(t)$), is calculated by Fourier analysis, using $y_n(t)$ as the output signal and $x_n(t)$ as the input signal:

$$x_n(t) = \cos\left(2\pi n\left(f_0 t + \frac{\Delta f}{2}t^2\right)\right) \sqcap (t/T - 1/2) Ш(F_s t) \tag{2–33}$$

$$\tilde{h}_n(t) = \mathscr{F}^{-1}\left[\frac{\mathscr{F}(y_n(t))}{\mathscr{F}(x_n(t))} \sqcap \left(\frac{f - nf_0}{nT\Delta f} - \frac{1}{2}\right)\right] \tag{2–34}$$

where $\mathscr{F}$ denotes the Fourier transform and $\mathscr{F}^{-1}$ denotes the inverse Fourier transform. Note that $\Delta f T$ represents the full bandwidth traversed by the frequency-time ramps. The rectangular window is applied here for only a positive component for a simpler interpretation (explained in details later). Then, $\tilde{h}_n(t)$ reduces to:

$$\tilde{h}_n(t) = A_n(t)e^{j\phi_n(t)} * \left\{e^{j2\pi f_c t}\operatorname{sinc}(nT\Delta f t)nT\Delta f\right\} \tag{2–35}$$

where $A_n(t)$ and $\phi_n(t)$ represent the bandwidth-averaged amplitude and phase of the received signal as a function of time, and f_c is the center frequency of the frequency-time ramp. Assuming far-field propagation, $\phi_n(t)$ is equal to the phase of the dominant ELF/VLF current source, whereas $A_n(t)$ depends on both the amplitude of the dominant ELF/VLF current source and the distance from the ionospheric source to the receiver. Here, $\tilde{h}_n(t)$ is complex-valued in order to directly assess the phase $\phi_n(t)$. This result is achieved by eliminating the negative frequency components in Equation 2–34 [*Gabor*, 1946].

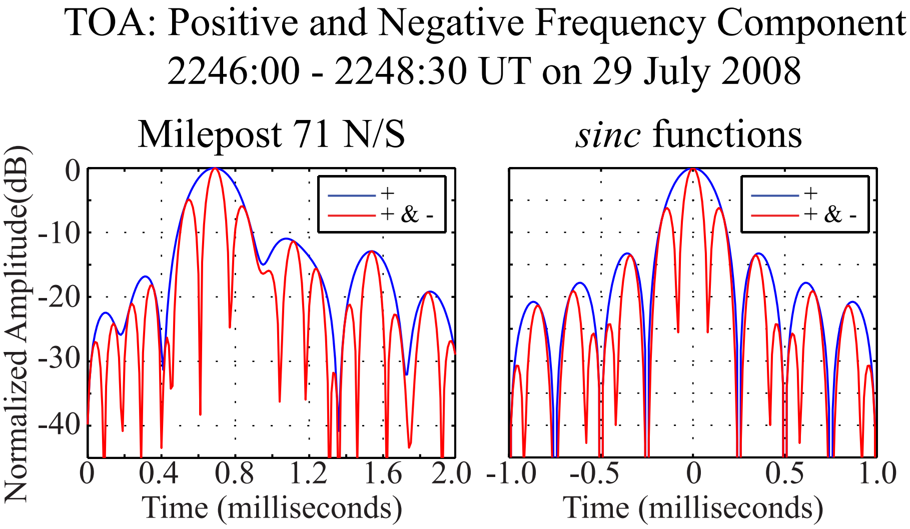

Figure 2-6. A comparison between TOA observations (left) and convolved sinc functions(right). The blue lines use only positive frequency components whereas the red lines use both positive and negative frequency components.

An example of (complex-valued) $\tilde{h}_n(t)$ and (real-valued) $h_n(t)$ is shown in Figure 2-6. As seen in Equation 2–35, the TOA result consists of the complex-weighted sum of sinc functions. Each signal arriving at the receiver at different times is convolved with a sinc function and forms the TOA result. Figure 2-6 also compares TOA results for calculations performed using only positive frequency components and those performed using both positive and negative frequency components. While the combined frequency form produces a narrower main lobe, it does not directly provide phasing information (it is entirely real-valued). Additionally, the positive-frequency (complex-valued) $\tilde{h}_n(t)$ represents the same information as the combined-frequency (real-valued) $h_n(t)$, due to conjugate (Hermitian) symmetry [*Boashash*, 2003]. The complex-valued form of $\tilde{h}_n(t)$ is used throughout this work.

As can be seen in the Equation 2–34, I apply a rectangular window in the frequency domain and transform it to the sinc function in the time domain. A different window can be used, such as a Hamming or Kaiser window, whose side lobes are suppressed to a greater extent than those of the rectangular window. However, the main lobe of the rectangular window is the narrowest of all. In this dissertation, the rectangular window is used to maximize the capability of separating multipath signals in time. The width of the sinc function is determined by the bandwidth of the frequency ramps, $\Delta f T$, and it dictates the TOA properties such as the timing accuracy and resolution.

2.3 TOA Properties

2.3.1 Timing Accuracy

One main concern regarding the TOA method is the timing accuracy of the detected peak amplitude. The effective impulse response is a sampled version of the continuous impulse response convolved with a sinc function whose width is determined by the bandwidth of the transmission. While the detected peak amplitude may be interpolated in time using standard Fourier techniques, the detected peak amplitude may not exactly coincide with the timing of the actual peak amplitude incident upon the receiver, due to convolution with the sinc function. To assess this accuracy, we calculate the Cramér-Rao Lower Bound (CRLB) [*Schuster et al.*, 2006, and reference herein] using the output of a modulated HF heating model that predicts the time distribution of amplitude and phase generated by modulated HF heating of the lower ionosphere. We now describe the HF heating model and how it is used to calculate the CRLB.

The HF heating model employed was developed by *Moore* [2007], and it requires as input the HF frequency, modulation frequency, and HF power. Electron temperature and density profiles, together with molecular nitrogen and molecular oxygen density profiles, are also provided as input. We apply the electron density profiles used in previous ELF/VLF studies [e.g., *Lev-Tov et al.*, 1995; *Moore*, 2007; *Agrawal and Moore*, 2012] and the rest of the ionospheric parameters are available in the MSISE-90 Model on the website at http://ccmc.gsfc.nasa.gov/modelweb/. Using this input, the model computes the modulated conductivities (Perdersen, Hall and Parallel) at each 1 km grid in 3-D rectangular coordinates. The model assumes a constant electrojet electric field parallel to ground throughout the *D*-region ionosphere to predict the magnetic field incident upon a given receiver location as a function of time assuming free-space propagation [*Payne et al.*, 2007]. For example, the model may be used to predict the amplitude and phase of the magnetic field incident upon a receiver as a function of time using a modulation frequency of 2.5 kHz, an

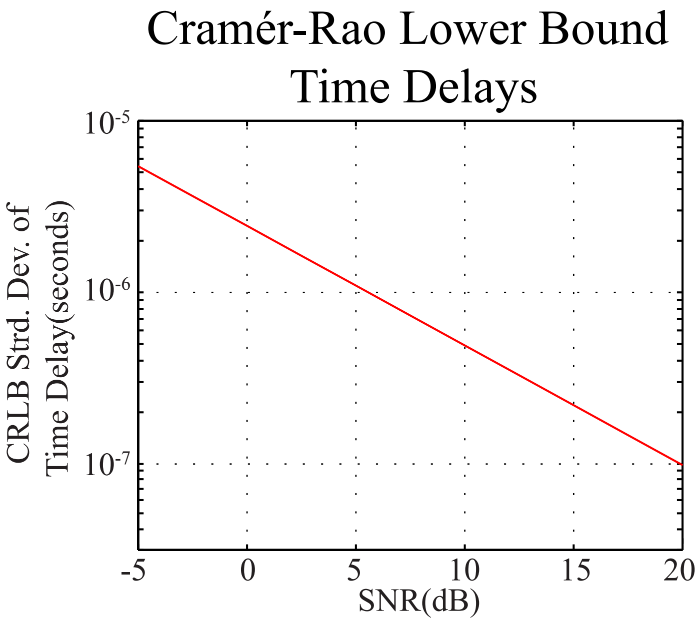

Figure 2-7. The Cramér-Rao Lower Bound (CRLB) of the standard deviation of the time delay for the peak amplitude computed by the HF heating model.

HF power of 85.7 dBW, and an HF frequency of 3.2 MHz (with X-mode polarization). The propagation model employed neglects Earth-Ionosphere waveguide effects, however. For the receiver locations used in this work (each less than ∼100 km away from the HAARP transmitter), this assumption is reasonable as has been demonstrated by *Payne et al.* [2007], which showed excellent agreement between simple ray-tracing and full-wave modeling results at these distances. Applying the TOA technique to the predicted magnetic field time series, I was able to assess the timing accuracy of my peak TOA measurement. Each time bin has three unknown parameters: amplitude, phase, and time delay. We create the Fisher information matrix [*Schuster et al.*, 2006, and reference herein] which may be used to directly compute the CRLB for different white Gaussian Noise levels. Figure 2-7 shows the CRLB of the standard deviation of the time delay for the peak amplitude in the model as a function of the signal-to-noise ratio (SNR). Typically, the SNR of our observations is 5 dB or higher, and Figure 2-7 indicates a best-case accuracy of ∼1 μsec at 5 dB SNR. While model predictions using other ionospheric profiles may yield slightly different results than presented here, we expect the ∼1-μsec accuracy figure to be generally representative of the accuracy of the TOA measurement. Although ELF/VLF data is also sensitive to impulsive noise (from lightning, for example) and to power line radiation in the ELF/VLF range, the CRLB is still a reasonable benchmark for timing accuracy, since we can increase integration period to reduce the noise, or I can just avoid a particular impulsive noise or frequency bandwidth. In addition to the error factors discussed above, there is a 27.5±2.5 μsec transmission delay due to the HAARP transmission and ±30 $n$sec GPS timing accuracy, which have been accounted for in our analysis.

To experimentally evaluate the SNR of the measurement, I perform the same TOA analysis on the data set starting with an offset of a half period of the frequency-time ramp. I do not expect HAARP-generated ELF/VLF waves to contaminate this measurement, yielding an effective measurement of the noise floor. From among the many noise-floor measurements that the TOA analysis produces, I pick the peak noise measurement as the noise floor. As an example, Figure 3-2 in the next chapter exhibits an approximate SNR of $\sim$12 dB (marked with a horizontal line) for the peak amplitude at Sinona Creek and an approximate SNR of $\sim$25 dB (marked with a horizontal line) for the peak amplitude at Milepost 71, both evaluated using 2.5 minutes of data. The nulls in the noise line may be caused by hum noise interference. I note that the SNR of the measurement increases significantly by repeating the frequency-time ramps for a few minutes.

2.3.2 Timing Resolution

Although the timing accuracy is not significantly limiting, the time resolution of the TOA method is more significant. The time resolution of the TOA method is determined by the reciprocal of the modulation bandwidth, which is, for example, $\sim$333 μsec with 3 kHz bandwidth of frequency analysis. The propagation time difference between the LOS and the first ionospherically reflected (IR) path is approximated to $\sim$450 μsec with *D*-region ELF/VLF wave source and reflection height, if we assume a speed-of-light propagation. This time difference is far apart enough to resolve the two signals, however, the measured results may be distorted by convolution with a *sinc* function which is introduced by a rectangular window in Fourier analysis.

To precisely extract the signals, I apply two different deconvolution methods: 1) the CLEAN method, and 2) an exhaustive least square error search algorithm. The CLEAN method iteratively

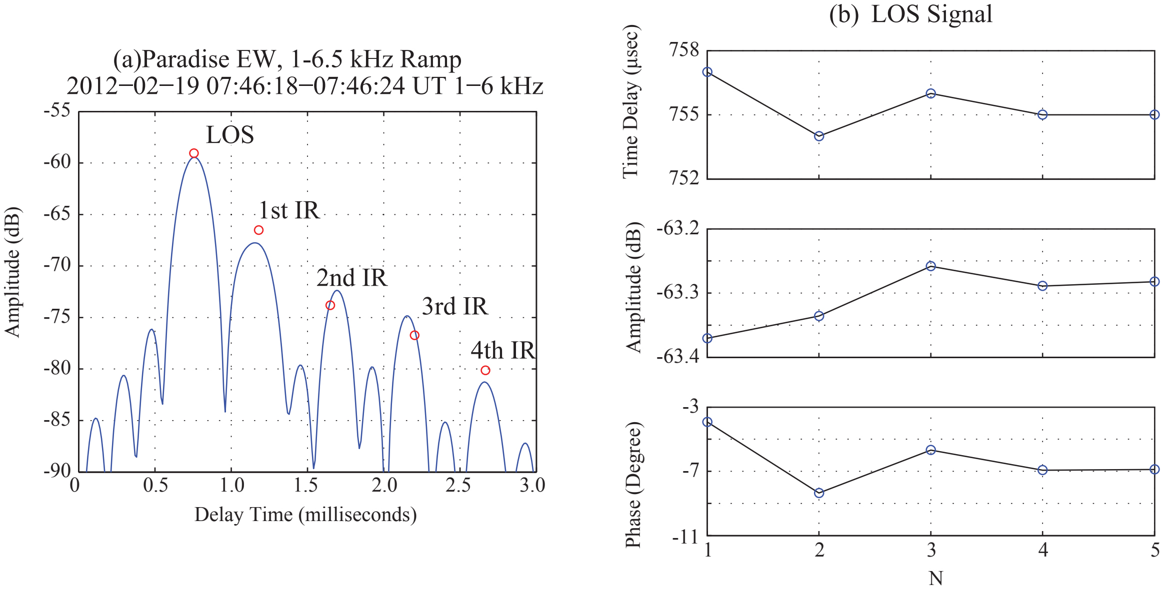

Figure 2-8. (a) Example of the TOA observation at Paradise's EW antenna for 1-6.5 kHz with 5 pulses. (b) Time delay, amplitude, and phase of LOS signal as a function of the number of signals (*N*).

subtracts a portion of the largest amplitude signal from the TOA observations until the noise floor is reached [*Segalovitz and Frieden*, 1978]. The CLEAN method thus decomposes the observed TOA into a series of complex-valued δ functions. *Fujimaru and Moore* [2011] reported an excellent match with a model result shown in Figure 3-3 in the next chapter. However, the CLEAN method cannot estimate each signal accurately if the largest amplitude signal has been distorted by other signals spaced closely in time. This distortion occurs when the LOS and IR signals arrive close in time relative to the time resolution determined by the bandwidth of the transmission. The time separation becomes smaller as a receiver site is further away from the source region. To solve this issue, the least square error search algorithm is typically applied.

The exhaustive least square error search algorithm is applied to deconvolve *N* pulses (amplitude, phase, and arrival time for *N* different paths) that best match observations. The algorithm scans combinations of *N* pulse arrival times, and calculates amplitudes and phases at each time combination in a least square sense. The pulses are convolved back with the *sinc* function and

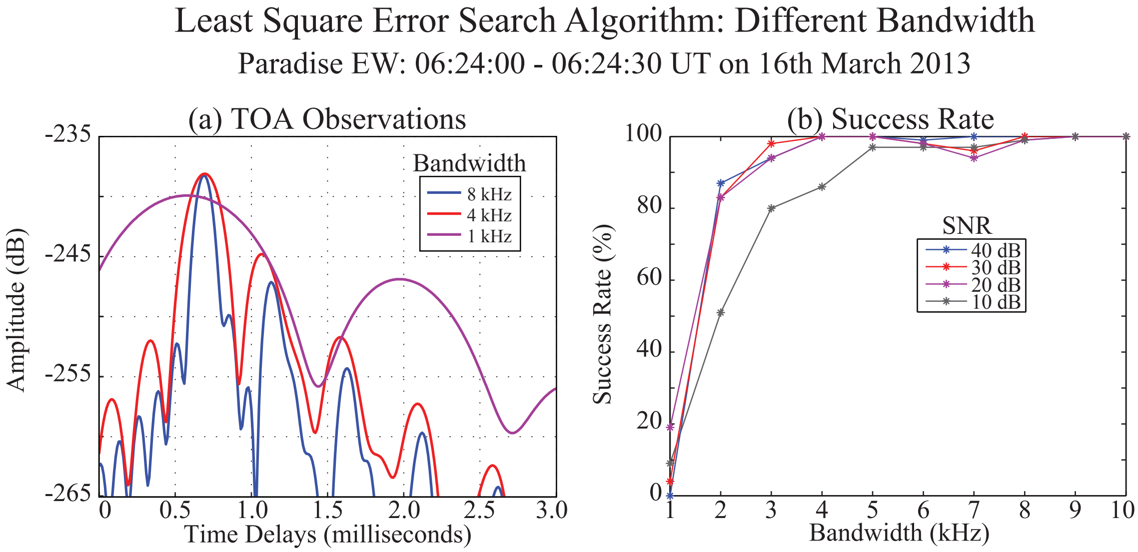

Figure 2-9. (a) TOA observations analyzed using different bandwidths. (b) Percentage of successful analyses using the least square error search algorithm as a function of bandwidth. Color indicates SNR.

compared with the original TOA observations using L-2 norms. The deconvolved pulses are the ones that give the least error. Choice of N is depend on a user's interest.

The relationships between N and the extracted pulses are plotted in Figure 2-8. Figure 2-8(a) is a TOA observation at Paradise's EW antenna with 1-6.5 kHz ramp. The blue trace is the TOA observation, and the red circles are the extracted signal in 5 different paths ($N = 5$). Starting from the earliest arriving signals, they indicate LOS, the 1st IR, 2nd IR, and so forth. Figure 2-8(b) is the propagation delay, amplitude, and phase of the LOS signal as a function of N, where N is a number of signals to extract. Each quantity converges as N increases. The larger N provides more accurate solution, however, at the cost of significantly more computation time. Typically, $N = m + 1$ yields a satisfactory result where m indicates the desired signal component to be analyzed.

It is worth noting that the result of this least square method depends on the bandwidth and SNR. In order to investigate the distribution of the results with different bandwidths and SNRs, the least square method is performed with the observations of the frequency ramp between 1–11 kHz. To see the effects of the bandwidth, I use the frequency windows of 1–11 kHz, 2–10 kHz, 3–8 kHz and so on, so that the frequency bandwidth changes but the center frequency stays the same to

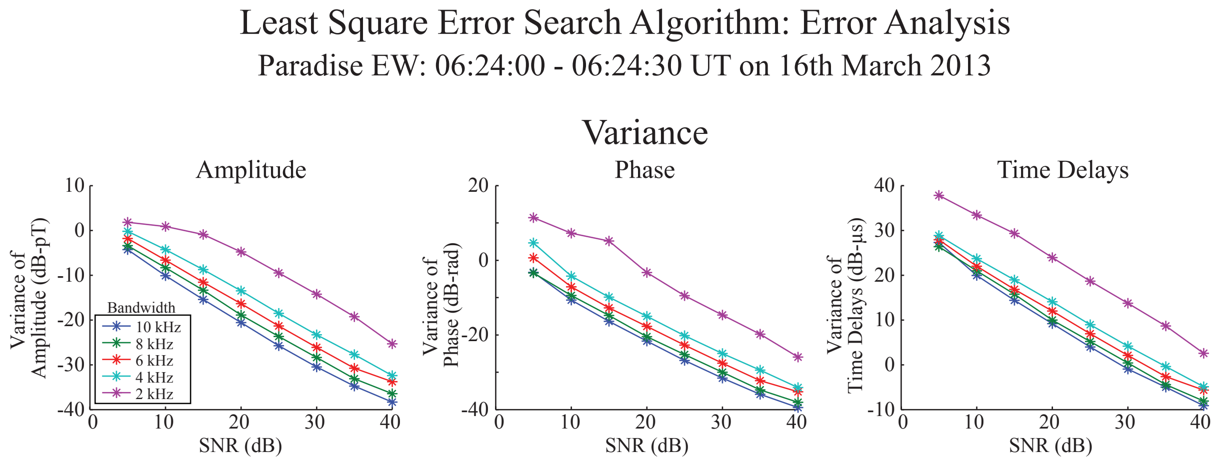

Figure 2-10. Variances of pulses ((a) amplitude, (b) phase and (c) propagation delays) deconvolved using the least square error search algorithm as a function of SNR. Color indicates bandwidth.

compare approximately the same average signal. To see the effect of SNR, I added noise to the observations to falsely set the SNR to a certain value in post-processing. The noise is taken during ambient times when the ramps are not transmitted. The raw observation has 40 dB SNR which will be the maximum SNR considered here. For a given frequency windows and SNR, the least square method was applied for 100 trials where at each trial noise is added taken from different ambient times. The results of this analysis are shown in Figure 2-9 and 2-10.

Figure 2-9(a) plots the TOA observations of the different bandwidths with ∼40 dB SNR. The width of the main and side lobes is wider at narrow bandwidth. With 1 kHz bandwidth, the LOS and the 1st IR signals are not resolved as two separate peaks. Figure 2-9(b) shows the success rate of the least square algorithm with 100 trials at different SNR and bandwidths. The least square algorithm does not provide a reasonable solution when the combination of the arrival times is not sensitive enough to fit to the observation. This occurs more often with lower SNR and narrower bandwidth. 1 kHz bandwidth is impractical for the least square method.

Figure 2-10 shows the variance of the least square algorithm for LOS amplitude, phase and arrival time as a function of bandwidths and SNR. With higher SNR and broader bandwidth, the variance is smaller. For 40 dB SNR, the standard deviations of the amplitude, phase, and arrival times for 3–10 kHz bandwidth vary only from ∼0.012–0.039 pT, ∼0.5–2°, and ∼0.35–1.0μs respectively. With 30 dB SNR, the standard deviations of the amplitude, phase and arrival times for 3–10 kHz bandwidth vary only by ∼0.03–0.1 pT, ∼1.5–6.0°, and ∼1.0–2.5μs respectively. Most of the TOA observations presented in this dissertation has either high enough SNR (>40 dB) for a narrower bandwidth (3 kHz) or broad enough bandwidth (>4 kHz) for a lower SNR (∼30 dB), whose error margins are less than 6% for the amplitude, less than 3° for the phase, and less than 2μs for the arrival times. This small error would not affect the analysis presented in this dissertation.

CHAPTER 3
EXPERIMENTAL VALIDATION OF THE TOA METHOD

In this chapter, I will demonstrate that the TOA technique is a valid measurement by comparing the experimental TOA observations with the amplitudes predicted by the HF heating model. Furthermore, TOA analysis is applied to observations performed during simple experiments: the results demonstrate that the TOA ELF/VLF source polarization and the TOA ELF/VLF source amplitude as a function of modulation frequency behave as expected for simple experiment geometries. Additionally, TOA analysis is applied together with a differential spatial analysis to experimentally detect the spatial distribution of ELF/VLF source phasing.

Some of the materials presented in this chapter have been published [*Fujimaru and Moore*, 2011].

3.1 TOA Observations versus Model Predictions

HAARP experiments designed to validate TOA analysis were performed on 29 July 2008 Universal Time (UT). During the experiment, a 7×7 element sub-array radiated a 3.2 MHz (X-mode) HF beam modulated with a linear chirped frequency format between 1 and 5 kHz over a period of 4 seconds. The frequency-time ramps were repeated sequentially for 150 seconds. Observations were performed at the ELF/VLF receiver systems that consist of two orthogonal air-core magnetic loop antennas oriented to detect the horizontal magnetic field at ground level, a preamplifier, a line receiver, and a digitizing computer that samples at 100 kHz with 16-bit resolution. The receivers are sensitive to magnetic fields with frequencies between $\sim$300 Hz and $\sim$45 kHz. The locations of the ELF/VLF receivers used throughout this dissertation are mapped in Figure 3-1.

Figure 3-2 shows the TOA observations at Sinona Creek (SC) and Milepost 71 (MP71) on the North-South (NS) antenna together with the approximated noise floor, demonstrating that the transmission sequence may be used to produce observations with significant SNR ($\sim$12 dB at SC and $\sim$25 dB at MP71). Figure 3-3 compares these same observations with model predictions. The solid blue lines are experimental observations, the solid red traces are the predicted amplitudes

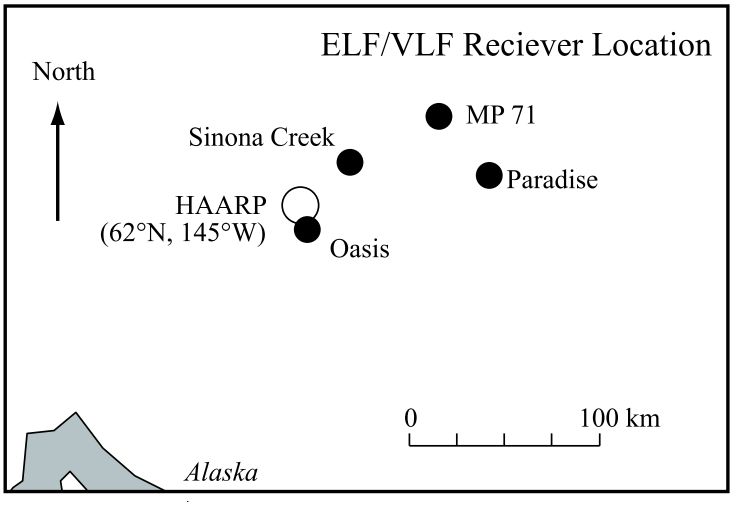

Figure 3-1. Map showing the locations of ELF/VLF receiver sites deployed between 2009 and 2013 for experiments relating to HAARP.

as a function of time (without processing, but including ionospheric reflection) with the reflection height set at 65 km and the effective reflection coefficient set at $0.3\angle 150^\circ$, and the dashed red lines represent the predicted amplitudes as a function of time (following TOA processing). The solid green spikes in Figure 3-3 are derived using the CLEAN method. I interpret earlier arrival times (e.g., $\sim$573 μ seconds at SC and $\sim$673 μ seconds at MP71) as the result of line-of-sight (LOS) propagation, whereas I interpret later arrival times (e.g., $\sim$900 μ seconds at SC and $\sim$1.04 milliseconds at MP71) as the result of the ionospherically reflected (IR) propagation.

Figure 3-3 shows that the modeled LOS signals reasonably matches the observed TOA at both SC and MP71. The TOA of the IR components at MP71 also closely match the timing of the model results, although at SC, the model and observed data are not aligned in time. This is possibly due to the low SNR of the IR component in SC data (Figure 3-2). It may also be possible that the IR components observed at SC and MP71 have different reflection heights and/or reflection coefficients due to the different angles of incidence at the ionospheric boundary. This example, and particularly the MP71 observation, demonstrates the ability of the TOA technique to discern LOS and IR path components of the ELF/VLF waves observed at the receiver. It also demonstrates the ability to assign amplitude values as a function of time. Both experimental observations and the

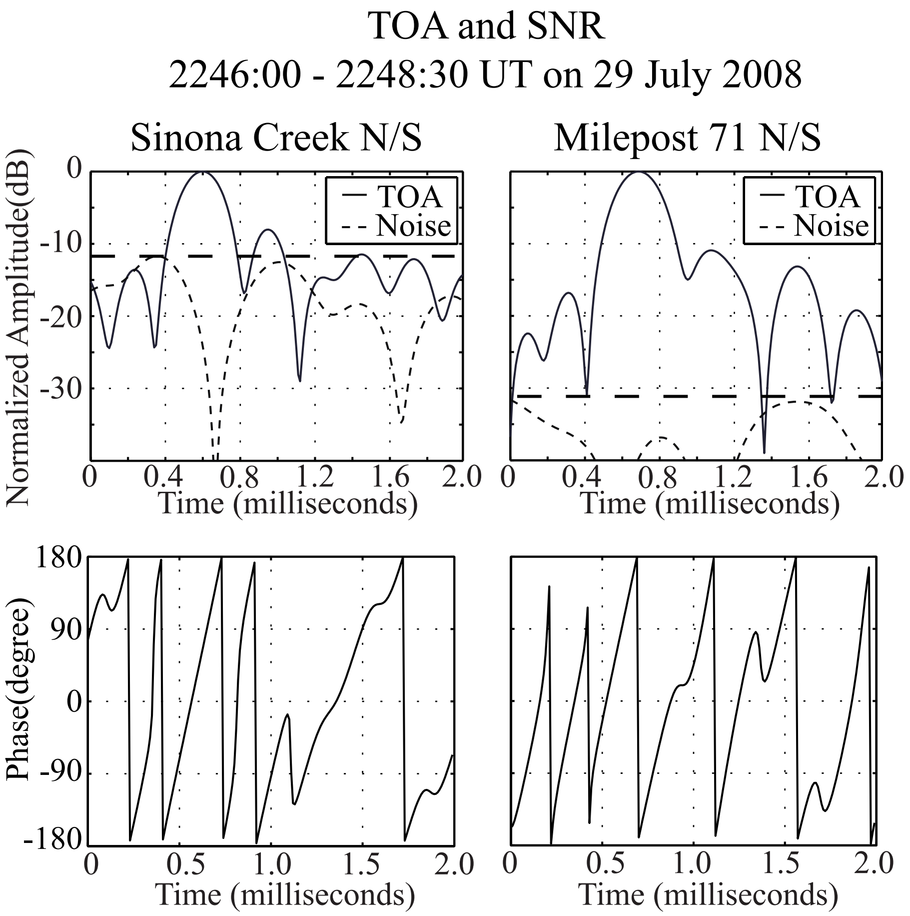

Figure 3-2. The TOA amplitudes and phases of the received ELF/VLF signal versus time. Sinona Creek NS antenna (left) and Milepost 71 NS antenna (right). The dashed line in each case shows the approximate noise level for each site. The horizontal wide dashed line is our noise reference level determined by the peak approximated noise level.

HF heating model indicate that the time difference between the direct and IR signal paths is greater than ~400 μsec, implying a bandwidth of ~2.5 kHz is suitable to resolve the two peaks.

3.2 Source Polarization

Source polarizations are determined by two orthogonal source currents, the Hall and Pedersen currents. The strength and dominant altitude of these source currents is different. Although Figure 3-3 shows the TOA analysis for only the North-South (NS) antenna, due to the interference (in amplitude and phase) produced by Hall and Pedersen currents, I expect observations on the NS and EW antenna to be somewhat different. Furthermore, because the direction of the Hall and

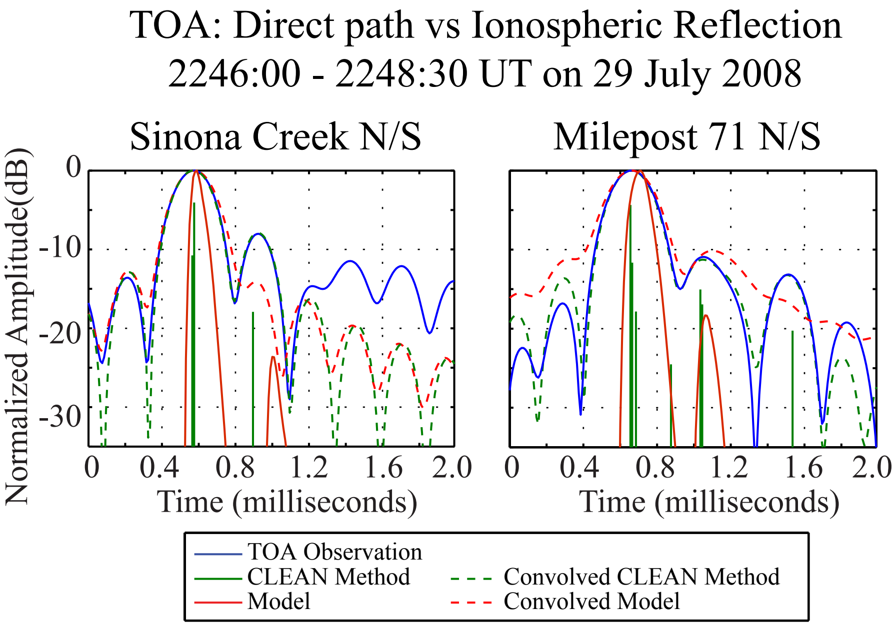

Figure 3-3. A Comparison between model prediction and observations at Sinona Creek (left) and Milepost 71 (right). On this plot, the CLEAN method is employed using a gain loop of 0.4.

Pedersen currents depend on the direction of the auroral electrojet currents, I expect the perceived time of arrival to depend on the direction of the auroral electrojet (Section 2.1.4).

Figure 3-4 shows the experimental observation of the interference of the two sources. The antenna has been artificially rotated in post-processing to simulate the TOA variation with auroral electrojet direction. From the left panel, it is clear that the TOA analysis is dependent upon the electrojet direction and antenna orientation. Expanding the time axis in the right panel, it is clear that the peak arrival time depends on the electrojet direction, varying by 30 μsec. Hence, the TOAs observed on the NS and EW antennas are determined by a combination of the magnetic fields radiated by the Hall and Pedersen currents which in turn depend on the direction of electrojet electric field. Also shown in the right hand panel (in black) is the magnitude of the TOA observation. The magnitude distribution varies with time, but does not depend on the direction of the auroral electrojet.

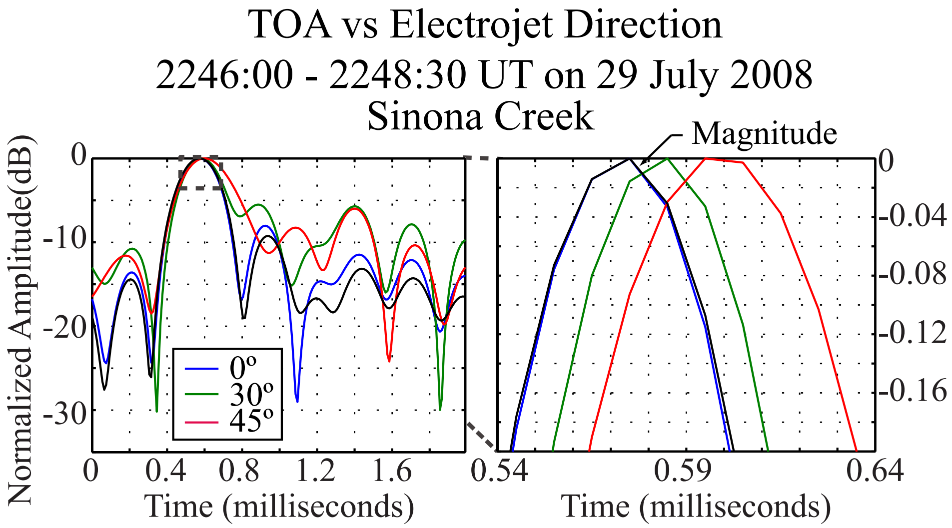

Figure 3-4. TOA at Sinona Creek as a function of the direction of electrojet current calculated by rotating the NS and EW antenna orientations in post-processing.

3.3 TOA versus HF Frequency & Power

The source heights as a function of HF frequency and HF power are investigated. The frequency-time ramps in this case ranged from 1 to 5 kHz over a period of 4 seconds. Every 4 seconds period, the HF power alternated between 25%, 50% and 100% power, and each period repeated for 5 minutes. Every 5 minutes, the HF frequency switched betweeen 3.2 MHz (X-mode) and 5.8 MHz (X-mode). Observations were performed at Sinona Creek and at Milepost 71, but the introduction of commercial powerlines near Milepost 71 site has significantly reduced the data quality at that site. In this section, only observations from Sinona Creek will be discussed.

Figure 3-5 shows the TOA analysis results for the maximum peak magnitude as a function of HF power at 3.2 MHz and at 5.8 MHz. The variations in TOA are small, less than 10 μseconds, whether in terms of HF frequency or in terms of HF power. The experimental results presented in Figure 3-5 do not definitively exhibit a monotonic increase in the TOA in terms of the HF power, and neither do they definitively show an increase in the TOA from 3.2 MHz to 5.8 MHz. Nevertheless, it is clear that the effects of HF frequency and power are relatively small compared to other parameters, such as the HF beam direction. It will be necessary to complete a full statistical

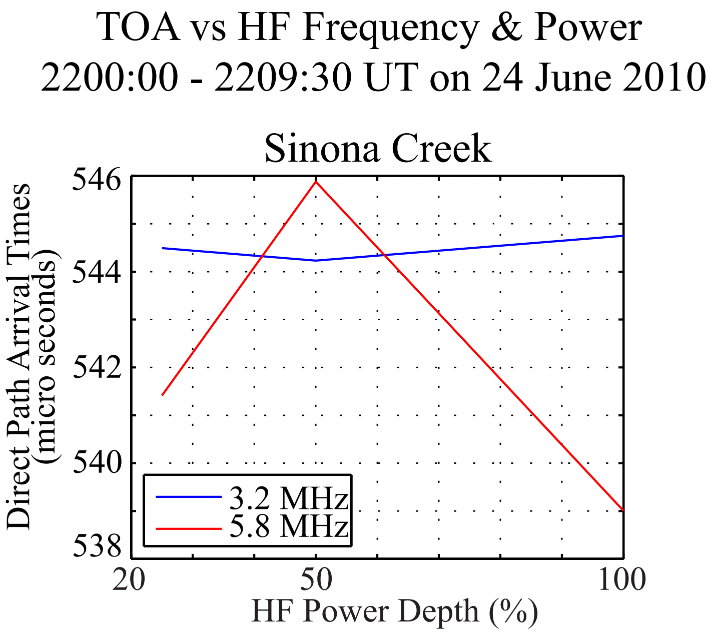

Figure 3-5. TOA as a function of HF frequency and power at Sinona Creek.

analysis of HF power and HF frequency TOA observations to determine whether a consistent dependence may be derived from this data set.

3.4 TOA as a Function of Modulation Frequency

The ELF/VLF wave generation as a function of modulation frequency has been of great interest due to the frequency dependent nature of the Earth-ionosphere waveguide. However, analysis of the data requires the use of a complicated Earth-Ionosphere (EI) waveguide model with an approximated ionospheric condition. Here, the TOA method is used to experimentally discount Earth-ionosphere waveguide effects and determine the effective source altitude as a function of modulation frequency.

For the data shown in Figure 3-6, TOA analysis was performed using a 3 kHz bandwidth centered on different frequencies within the 1-5 kHz frequency-time ramp. The effective source altitude tends to decrease with increasing modulation frequency from a center frequency of 2.5 kHz to 3.5 kHz. Model predictions (shown in the right panel) from the HF heating code introduced in Section 2.3.1 demonstrate that the source altitude tends to decrease with modulation frequency: the conductivity modulation directly above the HAARP transmitter for 1 kHz modulation contains

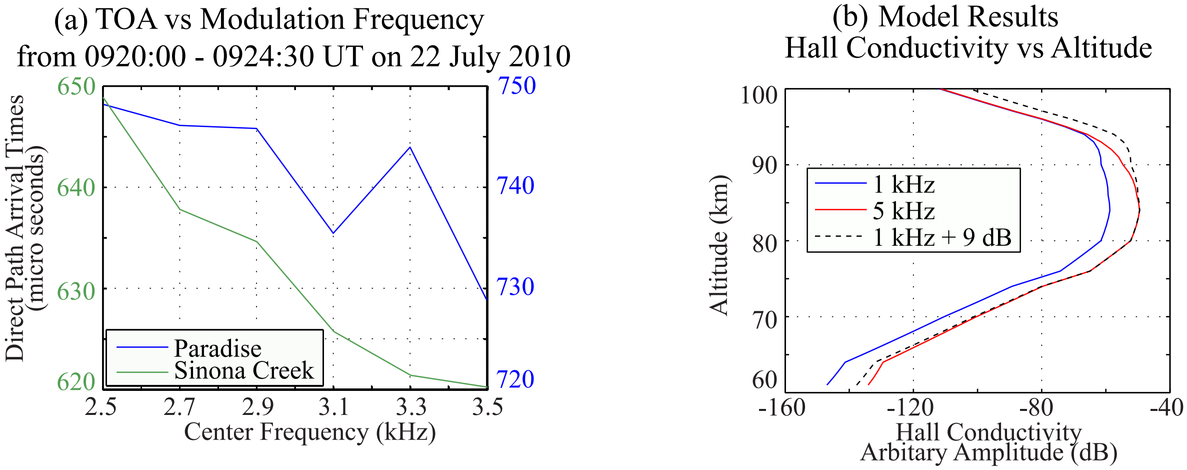

Figure 3-6. (a) TOA as a function of modulation frequency at Sinona Creek and Paradise. (b) Amplitude of Hall conductivity modulation as a function of height at 1 and 5 kHz using generic electron density and temperature profiles.

larger conductivity modulation components at higher altitudes than for 5 kHz. The variation in the two traces is almost exactly the same below an altitude of 85 km. Above 85 km, the 1 kHz modulation is relatively stronger than the 5 kHz modulation. The modulation of the Pedersen conductivity (not shown) exhibits similar effects.

3.5 Broad Beam Construction from Multiple Narrow Beams

In this section, we demonstrate that the ELF/VLF waves generated using a narrow HF beam pattern directed at multiple specific locations in the sky can be linearly summed to accurately approximate the ELF/VLF radiation produced by a broadened HF beam pattern. Recently, a similar effect has been discussed: *Gołkowski et al.* [2013] interpreted observations of ELF/VLF wave amplitudes generated by simultaneously modulating the ionosphere using two HF beams at different HF frequencies as the sum of the ELF/VLF signals generated using the individual HF beams. The theoretical predictions were provided by a simple model and heuristically matched observations. The analysis provided by *Gołkowski et al.* [2013] is not substantially different from past work that analyzed ELF/VLF phased arrays [*Barr et al.*, 1987; *Papadopoulos et al.*, 1989; *Cohen et al.*, 2008, 2010b,a], in that the phased array structure of the source was modeled and compared to observations to show consistency. The experiment described in this section uses HAARP's broad beam

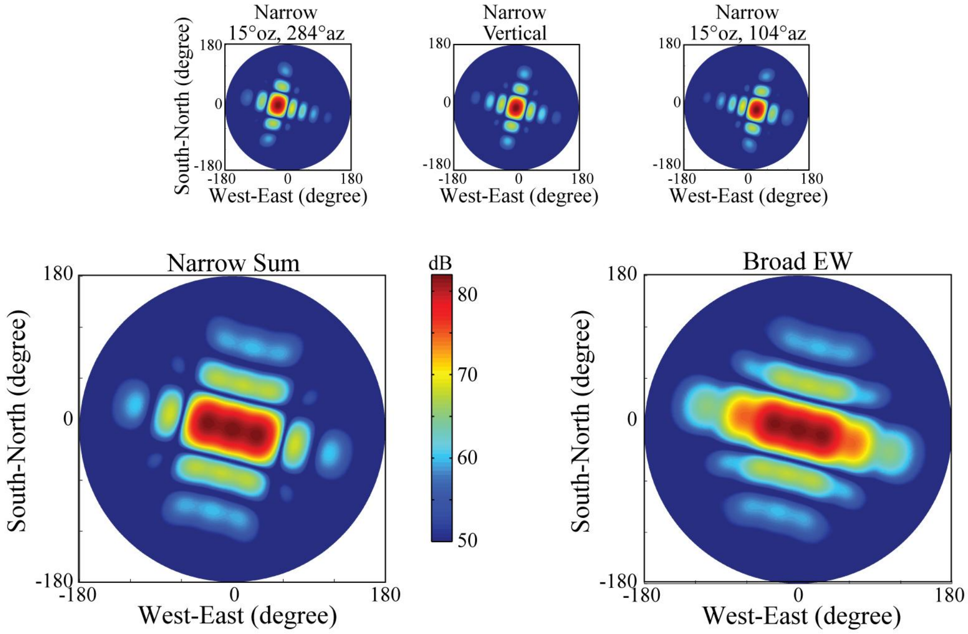

Figure 3-7. (top) Three narrow HF beam patterns: 15° off-zenith with 104° azimuth, vertical and 284° azimuth. (bottom) A comparison of the sum of the three narrow beam patterns (left) with the vertical BBEW pattern (right).

pattern to generate waves, and then approximates the result by summing the waves generated separately by three narrow beam patterns. In this case, the HF beams are all at the same HF frequency, and no theoretical modeling is required. These experimental results are thus the first experimental confirmation that a linear sum of the ELF/VLF waves generated by multiple narrow HF beams suitably approximates the ELF/VLF fields generated by the broader HF beam pattern.

3.5.1 Narrow Beam/Broad Beam Experiment Description

HAARP is capable of broadcasting a "Broad EW" HF beam pattern (BBEW), which spoils the narrow HF beam pattern in the East-West direction, as shown in Figure 3-7. The BBEW beam pattern can be approximately decomposed into appropriately scaled (in ERP) narrow HF beam patterns directed toward: 284° Az with 15° off-zenith (OZ), Vertical, and 104° Az with 15° OZ. The three narrow beam patterns and the sum of the three narrow beam patterns are shown alongside the BBEW pattern in Figure 3-7. The BBEW pattern is grossly equivalent to the sum of the three appropriately scaled narrow beams.

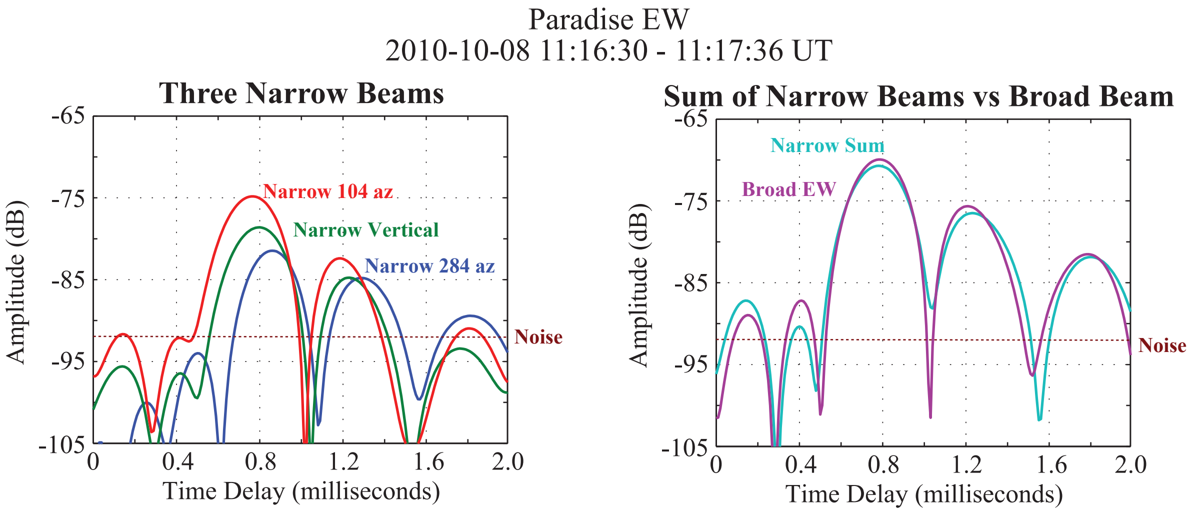

Figure 3-8. (left) TOA observations for the three narrow beam patterns. (right) TOA observations for the sum of the three narrow beam patterns and the BBEW pattern.

On 8 October 2010, HAARP broadcast each beam pattern described above at 3.2 MHz (X-mode). Each beam was modulated using AM sine modulation with a linear frequency-time chirp from 0.5 kHz to 6.5 kHz over 6 seconds.

3.5.2 Results and Analysis

TOA observations from Paradise are shown in Figure 3-8. The TOA observations are processed using a bandwidth of 1–5 kHz and produce a decent SNR (16 dB). Figure 3-8 includes TOA observations for BBEW, the three individual narrow beams, and the sum of the three narrow beams. Comparing the BBEW and the sum of the narrow beams, the amplitude, phase (not shown), and timing of the TOA analyses are all extremely similar. Hence, ELF/VLF wave generation using the BBEW pattern can be closely approximated by summing the ELF/VLF fields generated by the three narrow beam patterns. This approximation extends to a more general conclusion: an arbitrarily shaped HF beam pattern can be successfully approximated using the linear summation of narrow beams that produce the arbitrary beam pattern. This concept will be used to analyze the phased array structure of the ELF/VLF source generated by BP/GM formats discussed in the next two chapters.

Together, the calculations and observations presented in this chapter demonstrate the validity and utility of the ELF/VLF TOA analysis method. In subsequent chapters, TOA analysis is applied to experimental observations in order to quantify physical properties produced by specific modulation formats.

CHAPTER 4
OBSERVATIONS OF ELF/VLF SOURCE PHASING

In the previous two chapters, the ELF/VLF TOA analysis method has been described in detail and applied to example experimental observations to demonstrate its utility. In this chapter, TOA analysis is applied to predict methods to increase the amplitude of generated ELF/VLF waves. Based on previous experimental observations of ELF/VLF waves generated using the Geometric Modulation (GM) format, which increases the ELF/VLF amplitude by 7–11 dB (over vertical AM heating) at frequencies above $\sim$3 kHz [*Cohen et al.*, 2008, 2010b,a], the formation of an optimized ELF/VLF phased array is the most promising technique to further improve the amplitude ELF/VLF wave generation. The analysis presented in this chapter is used to provide a limited optimization of the signal radiated by a phased ELF/VLF source and to identify the additional parameters required to complete a full optimization.

New experimental observations are presented of ELF/VLF waves generated using a modified GM format: GM is combined with pulse modulation (in effect producing beam painting, or BP, modulation) to control the physical area of the ionospheric ELF/VLF source region. As a result, four competing physical effects that contribute to the received ELF/VLF amplitude are closely investigated: the area of the ELF/VLF source region, the oblique angle of HF heating, the effective duty cycle of GM, and the phase distribution within the ELF/VLF source region. Based on these observations, new modulation formats are predicted to increase the received ELF/VLF magnitude by more than 4 dB and the HF-to-ELF conversion efficiency by more than 7 dB.

4.1 Beam Painting/Geometric Modulation (BP/GM)

4.1.1 BP/GM Experiment Description

20 days of successful ELF/VLF observations were performed over the course of four experimental HAARP campaigns between 19 Jul 2011 and 12 May 2012. During these campaigns, the HAARP HF transmitter broadcast a variable pulse length geometric modulation format. Two types of transmission formats were employed, and both are depicted schematically in Figure 4-1. Both transmission formats are based on the circle sweep GM format, which traces out a circle in the

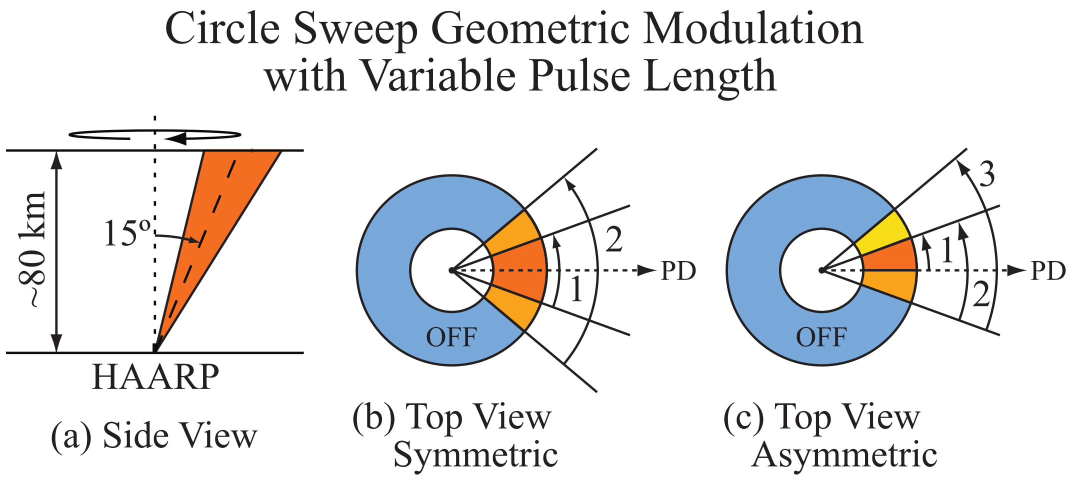

Figure 4-1. Cartoon diagrams for modified circle sweep geometric modulation formats. (a) Side view. (b) Top view: two symmetric arcs. (c) Top view: three asymmetric arcs. The orange and blue regions indicate when the HF beam is ON or OFF, respectively.

ionosphere, as depicted in Figure 4-1(a). These formats additionally employed a variable pulse length modulation format such that the HF transmitter was ON only for a portion of each circle sweep. The end result is a circle sweep GM format that produces an ELF/VLF source with a certain known arc length.

For the first format, depicted in Figure 4-1(b), the timing of the variable pulse length modulation produces arc lengths varying from 20° to 360° in 20° steps. The arcs were produced such that they were all centered on the same azimuthal direction: 81° east of north (EoN) (which is the direction toward the ELF/VLF receiver located at Paradise). For the second format, the resulting arc lengths vary from 10° to 360° in 10° steps, but the arcs are incremented asymmetrically as indicated in Figure 4-1(c). Strictly speaking, only the 360° arc length transmissions are GM formats, whereas the remainder of the transmissions would be classified as BP formats because they include off time during the modulation period. Accordingly, we will refer to these formats as BP/GM transmission formats.

For both of these BP/GM transmission formats, HAARP broadcast an HF wave at 3.2 MHz (X-mode) with 15° off-zenith angle and 85.7 dBW effective radiated power (ERP). The transmission for each arc length had a duration of 3 seconds. During the 3-second duration, the speed of the circle-sweep linearly increased, so that the expected ELF/VLF modulation frequency linearly increased from 1.5 to 4.5 kHz over the course of the 3 seconds. The resulting frequency-time ramp, or linear chirp, is used in post-processing to determine the propagation delay between HAARP transmission and ELF/VLF wave reception by employing time-of-arrival (TOA) analysis. After each 3-second period, the arc length increased in the steps described above.

In order to provide a comparison with amplitude modulation (AM) formats, the BP/GM transmissions were bounded by AM transmissions. The 25 symmetric format transmissions were bounded by AM transmissions that were aimed vertically, whereas the 77 symmetric and 69 asymmetric format transmissions employed oblique AM heating transmissions that were aimed at a 15° of off-zenith angle and 81° EoN azimuth. Both vertical and oblique AM transmissions broadcast at 3.2 MHz (X-mode) with the same ERP and the same frequency-time ramp as GM using 50% duty cycle square-wave modulation.

A direct comparison can be made between ELF/VLF signals generated using oblique AM heating formats and those generated using BP/GM formats with arc lengths of 20°. The 360° GM formats are implemented using an average of 12 HF beam positions. At lower modulation frequencies, more HF beam positions are used to implement the circle sweep, whereas at higher frequencies, fewer HF beam positions are used. At 3 kHz, however, exactly 12 HF beam positions are used. THe BP/GM arc length of 20° exactly correspond to an oblique AM heating transmissions with 5.6% duty cycle. As a result, we are able to use the ELF/VLF amplitudes observed at 3 kHz for AM 50% duty cycle heating and BP/GM with 20° arc length as a measure of ELF/VLF amplitude dependence on duty cycle. This measurement enables the characterization of ionospheric heating and cooling rates as well as the characterization of the effective duty cycle for GM formats.

In this section, I present a statistical summary of observations performed over the course of the four campaigns (and for which the geomagnetic and ionospheric conditions varied significantly), but we highlight observations with particularly high signal-to-noise ratio (SNR) performed on 20 July 2011 and 19 February 2012. On 20 July 2011, the HAARP flux-gate magnetometer registered

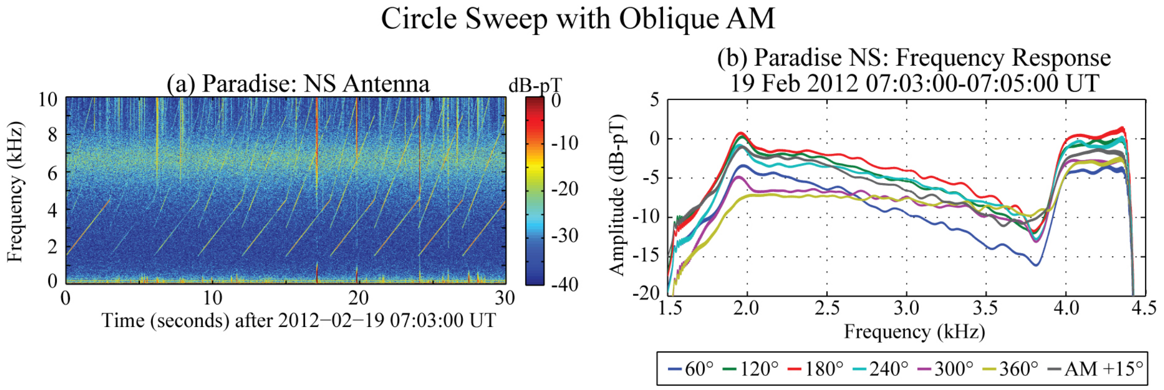

Figure 4-2. Asymmetric GM Circle sweep with oblique AM: Spectrogram (a) and frequency response (b) for different arc lengths (color) of the circle sweep and oblique AM. The "AM +15°" label identifies amplitude modulation with a beam tilted 15° toward Paradise (81° az).

fluctuations <75 nT, ionospheric absorption as measured by the HAARP riometer was ∼0.2 dB, and the K_p index was 4. On 19 February 2012, the HAARP flux-gate magnetometer registered fluctuations <50 nT, ionospheric absorption as measured by the HAARP riometer was ∼0.3 dB, and the K_p index was 3−.

4.1.2 BP/GM Experimental Observations

4.1.2.1 Frequency and time response observations

A spectrogram and associated frequency responses for the BP/GM formats are compared to oblique AM heating in Figure 4-2. The first ramp in the spectrogram is generated by oblique AM heating and the remainder of the ramps are generated by BP/GM whose arc length increases from 10° to 90°. For both types of transmissions, the second and third harmonics are successfully detected. The frequency response panel contains oblique AM and BP/GM for every 60° arc length. Over this frequency range, the amplitude increases up to ∼180° arc length and decreases afterward, with details depending on frequency.

Figure 4-3 presents TOA observations comparing GM (full circle sweep) and oblique AM heating. Each trace exhibits a dominant LOS peak at ∼0.7 milliseconds and a secondary peak at ∼1.1 milliseconds, which is interpreted as the first ionospherically reflected (IR) signal. Using the least square deconvolution procedure discussed in Chapter 2, we identify the amplitude, phase, and

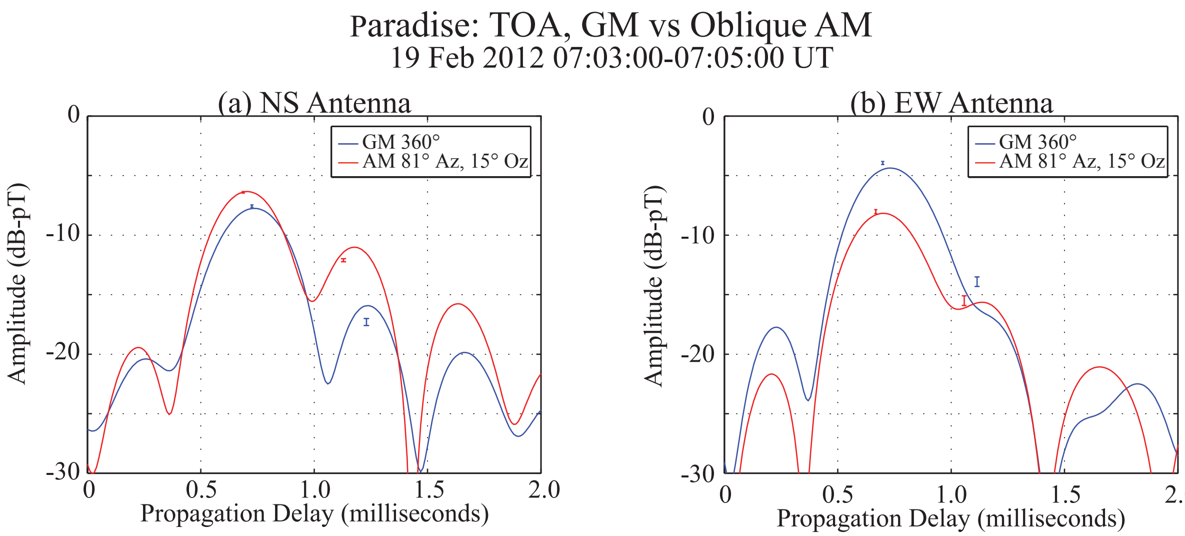

Figure 4-3. TOA observations for GM 360° circle sweep and oblique AM heating (50% duty cycle) at Paradise for (a) the north-south antenna and (b) the east-west antenna. Error bars indicate the uncertainty in amplitude for the LOS and IR signal components.

propagation delay associated with the LOS and IR signal components, all of which are identified in Figure 4-3. While the propagation delay identifies the maximum possible ELF/VLF source altitude, we can assume a specific geometry and approximate the source altitude for that geometry. For example, the source altitude for oblique AM heating can be approximated as ∼90 km altitude if we assume ELF/VLF waves propagate at the speed-of-light and that the source is located at the center of the HF beam.

For the case shown in Figure 4-3, GM enhances the LOS amplitude only for the EW channel as compared to oblique AM. The total ELF/VLF signal magnitude for GM is only ∼2 dB stronger than for oblique AM, and this is typically the case. Figure 4-4(a) plots the ratio of the ELF/VLF signal magnitude (independent of signal polarization) for GM to that for oblique AM averaged over the duration of the four campaigns (with the average weighted by signal-to-noise ratio (SNR)). GM is typically weaker than oblique AM by ∼1 dB near 2 kHz, but stronger than oblique AM by ∼1-3 dB at higher frequencies. Using TOA analysis, GM is typically stronger than oblique AM by 0.6–1.6 dB. For comparison, Figure 4-4(b) plots the ratio of the ELF/VLF signal magnitude for GM to that for vertical AM heating similarly averaged over the duration of the four

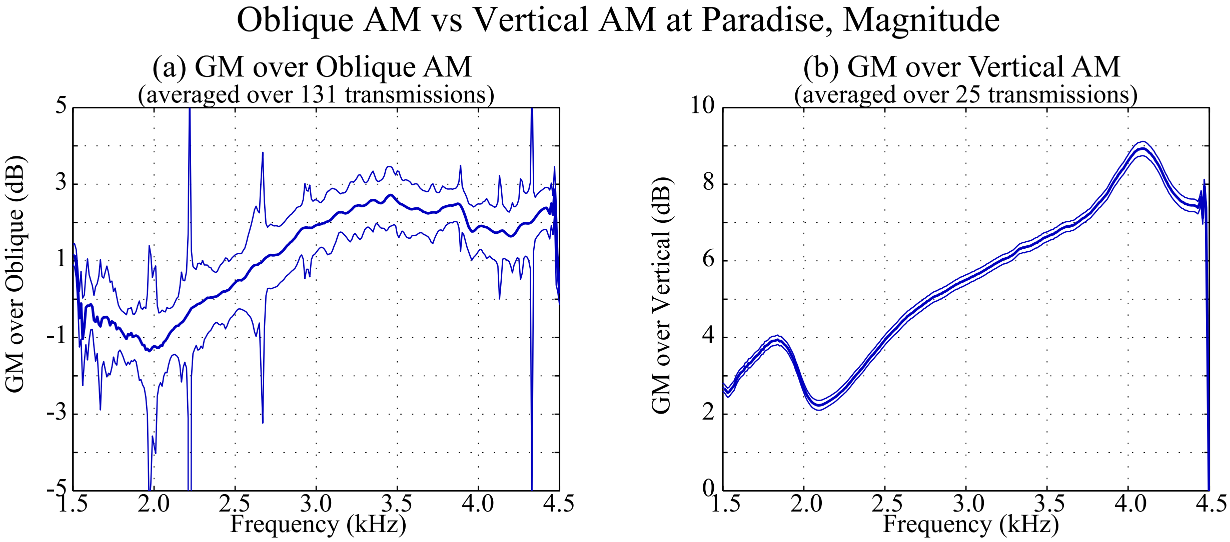

Figure 4-4. (a) The SNR-weighted ratio of the ELF/VLF signal magnitude for GM to that for oblique AM averaged over the duration of the four campaigns. (b) Same plot, but for vertical AM.

campaigns. The ratio of GM to vertical AM heating is consistent with past observations and predictions [*Moore and Rietveld*, 2009; *Cohen et al.*, 2010a]. Compared to vertical AM heating, GM produces larger ELF/VLF signal magnitudes (by at least 2 dB) across the frequency range, and at higher modulation frequencies the effect is more pronounced (up to 9 dB). TOA analysis indicates that GM is typically stronger than vertical AM by 5.9–6.1 dB. Similar observation led *Cohen et al.* [2008] to imply that ELF/VLF wave generation using GM might produce unprecedented HF-to-ELF conversion efficiencies at higher modulation frequencies. Compared to oblique AM heating, however, GM produces lower ELF/VLF signal magnitudes at frequencies of 2 kHz and below. At 3 and 4 kHz, GM produces 1–3 dB larger signal magnitudes, but the difference appears to stop increasing in that frequency range. In this case, it appears that the nature of oblique AM heating at higher modulation frequencies produces a substantial portion (4–7 dB out of 7–9 dB) of the gain previously reported and attributed to the GM heating format at higher frequencies.

These observations are actually consistent with the observations reported by *Cohen et al.* [2010a], who indicated a 3–4 dB enhancement in amplitude for oblique AM heating compared to vertical AM heating and also identified amplitude gains of ∼2.5 dB for oblique heating at 5010 Hz

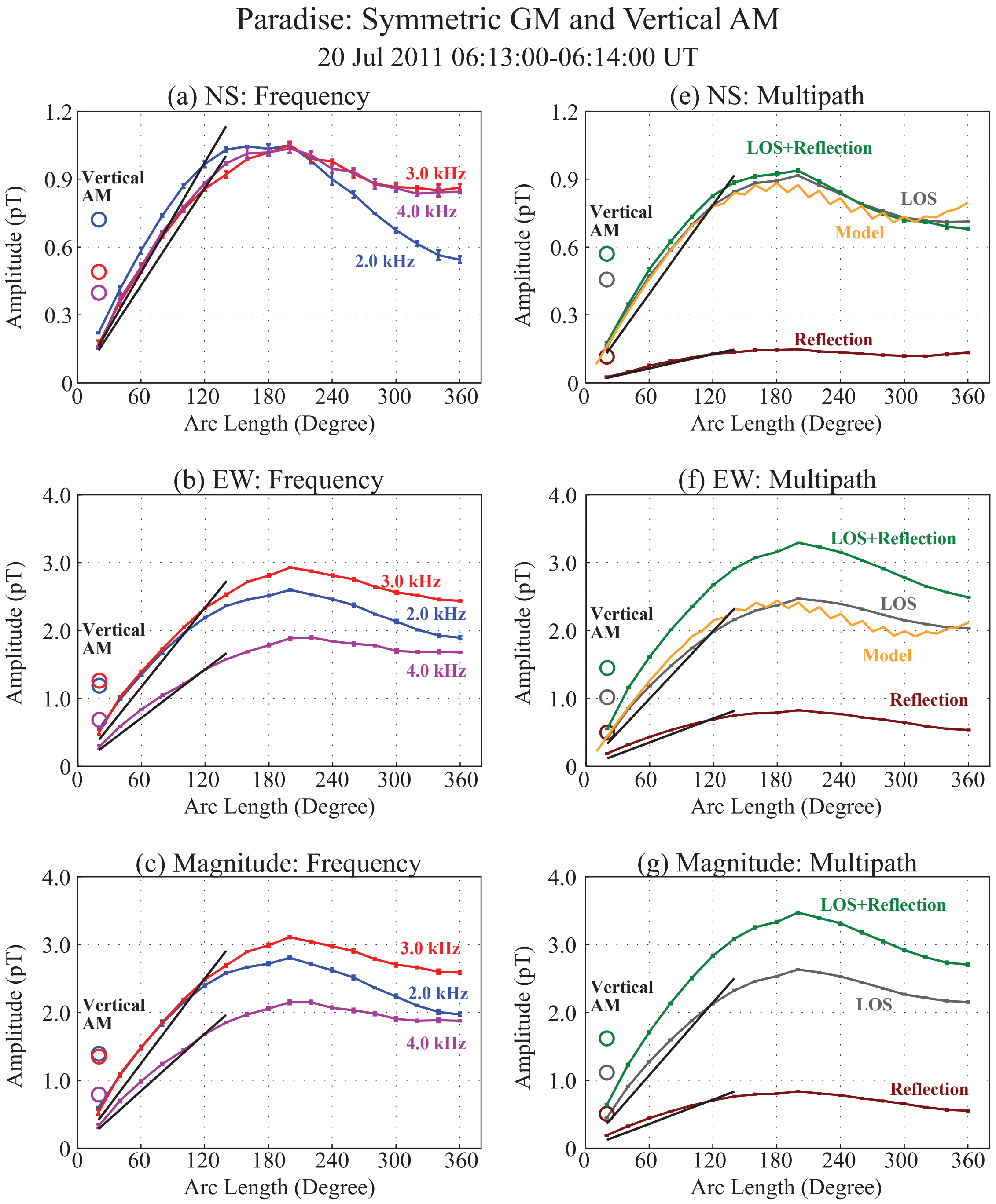

Figure 4-5. Symmetric circle sweep amplitudes as a function of arc length compared with AM vertical heating at Paradise.

versus 1249 Hz. *Cohen et al.* [2010a] concluded that based on their observations, oblique heating contributed only a small fraction of the gain observed for GM formats. At higher frequencies, however, our observations (near 4 kHz) are more consistent with the sum of their oblique HF

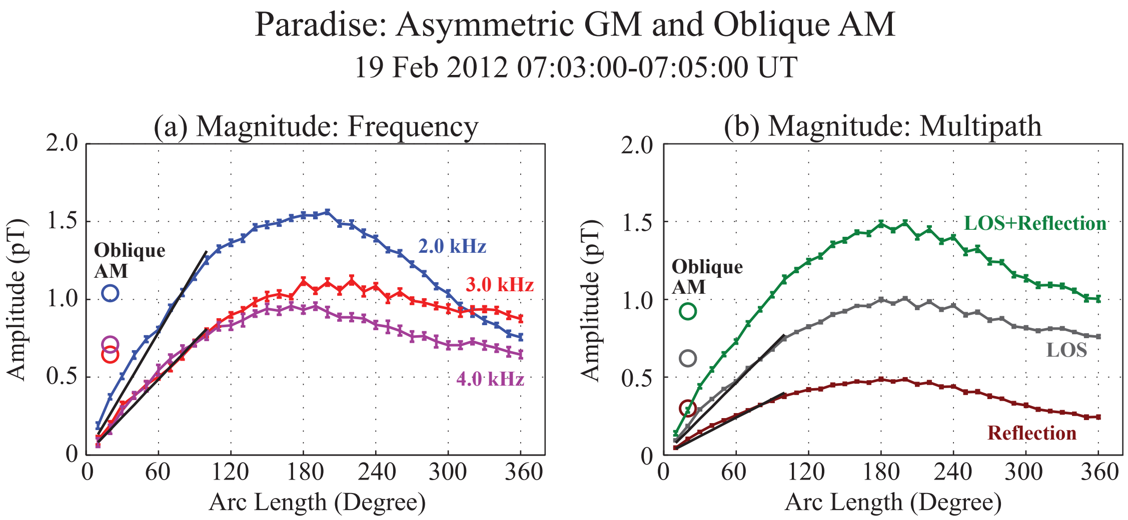

Figure 4-6. Asymmetric circle sweep amplitudes as a function of arc length compared with AM oblique (81° Azimuth, 15° off-zenith) at Paradise.

heating effects: a 5.5–6.5 dB enhancement. These gains attributed to oblique heating are, in fact, a significant portion of the 7–11 dB enhancement originally attributed to the GM heating format at high frequencies. It is noteworthy that oblique AM heating is more efficient (accounting for shorter transmission durations) than GM heating by 3–5 dB at 2 kHz and by 0.5–2.0 dB at 4 kHz, observations that are perfectly consistent with the theoretical predictions presented by *Moore and Rietveld* [2009].

It should be noted at this point, however, that the directionality of the ELF/VLF source produced by oblique heating produces a competing effect once multiple beams are employed. If N beam directions are employed, the heated area approximately increases by a factor of N. Due to the directionality of the ELF/VLF source produced by the oblique HF beam, this factor of N is not realized in practice. This effect will be discussed in greater detail later in this chapter.

4.1.2.2 Amplitude as a function of arc length

Figure 4-5 shows the ELF/VLF signal amplitudes and magnitudes received at Paradise for different frequencies (2, 3 and 4 kHz), the LOS signal component, and the first IR component as a function of arc length for the symmetric BP/GM experiment. The amplitudes/magnitudes for specific frequencies are shown in the left panels ((a), (b) and (c)), while the amplitudes/magnitudes

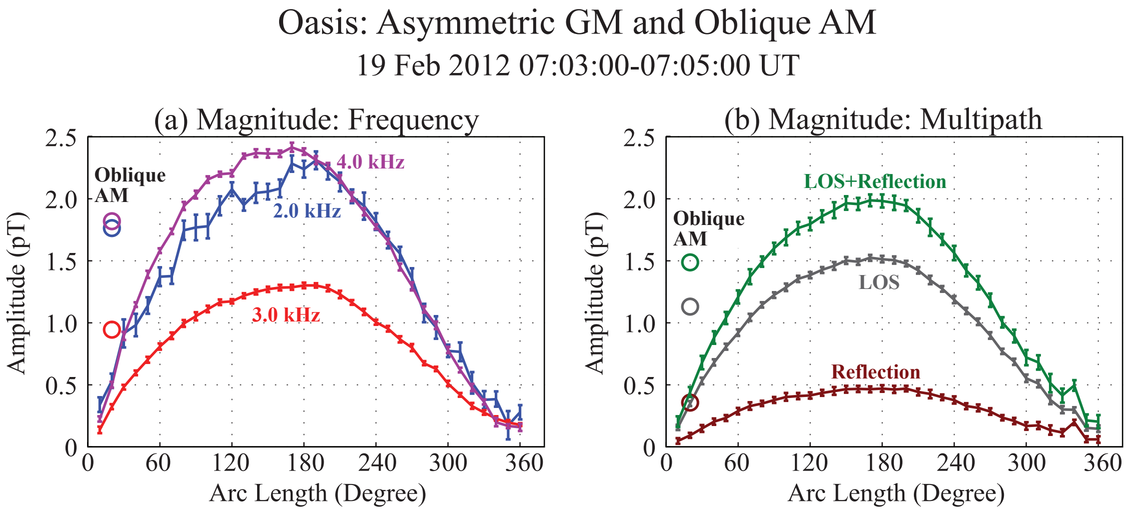

Figure 4-7. Asymmetric circle sweep amplitudes as a function of arc length compared with AM oblique (81° Azimuth, 15° off-zenith) at Oasis.

for the LOS and first IR components are shown in the right panels ((d), (e) and (f)). The LOS amplitudes, isolated from the waveguide effects, are compared with the predictions of a simple distributed phased array model. Aside from specific details, all of the plots are very similar in nature. In all cases, the signal level increases until an arc length of 180°–200°. At larger arc lengths, the signal level decreases. At low arc lengths, the signal levels increase approximately linearly with arc length, which is not unexpected considering that past work has indicated that the ELF/VLF signal amplitude is proportional to the area of the heated region [*Barr and Stubbe*, 1991a]. The traces exhibit slight curvatures at low arc lengths, however, and we attribute this curvature to the different source phasing as a function of arc length. This phased array nature is much more pronounced at larger arc lengths, where this effect is the dominant cause of the reduction in signal level (>200°). Plotted together with the BP/GM traces are the amplitudes/magnitudes observed for vertical AM heating. We have plotted these points at 20° arc length to indicate the similar nature of the two transmissions. Vertical AM heating produces larger signal amplitudes than the 20° BP/GM "sweep" due in large part to the larger duty cycle employed. We hesitate to make a direct comparison using vertical AM transmissions, however, and reserve detailed comment for comparisons with oblique AM heating.

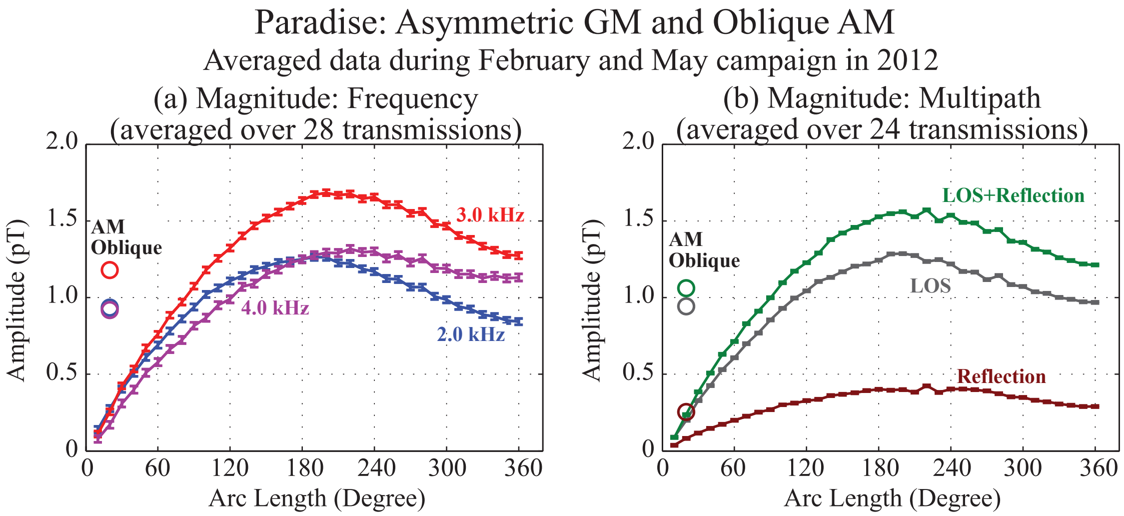

Figure 4-8. Average asymmetric circle sweep amplitudes as a function of arc length compared with oblique AM (81° Azimuth, 15° off-zenith) at Paradise.

Figures 4-6 and 4-7 show the results of asymmetric BP/GM compared with oblique AM observed at Paradise and Oasis respectively. Because the traces are so similar, we have only plotted the results for signal magnitude. While the traces shown for Paradise are extremely similar to those for the symmetric experiment, here we highlight the comparison with *oblique* AM heating. The signal levels generated by oblique AM are a much larger fraction of GM than those generated by vertical AM heating. In fact, in many cases, the signal generated using oblique AM heating is larger than that generated using the full sweep GM. The oblique AM heating transmission is only different from the 20° BP/GM transmission in their duty cycles: oblique AM utilized a 50% duty cycle, whereas the 20° BP/GM transmission is equivalent to a 5.6% duty cycle. Based on our observations, the duty cycle difference typically produces a 3.9–4.5 dB gain in favor of the 50% duty cycle. Observations at Oasis serve to highlight the phased array nature of the ELF/VLF source. All of the observed signal levels increase up to 180° and decrease to null amplitudes at 360°. For 360°, each of the individual source regions can be paired with out-of-phase counterparts, since Oasis is located very close to HAARP at the center of the circle, and these observations are consistent with the model predictions provided by *Cohen et al.* [2010b].

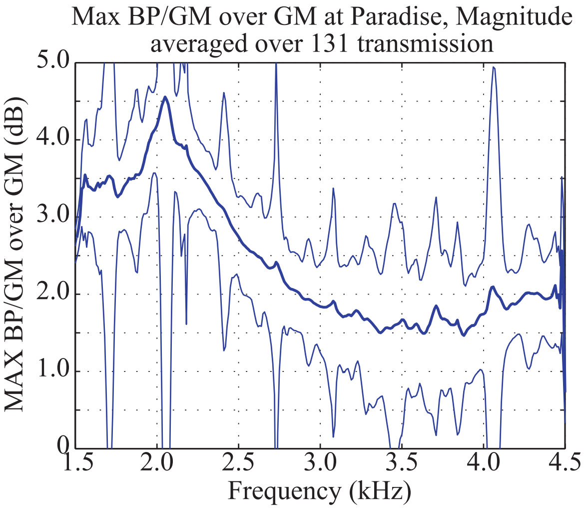

Figure 4-9. The campaign-averaged ratio of the ELF/VLF signal magnitude generated using 360° GM to the maximum BP/GM signal magnitude.

Refocusing once again on observations performed at Paradise, Figure 4-8 presents weighted average signal magnitudes for the asymmetric BP/GM experiment for 20–30 transmissions performed during the 2012 Feb and May BRIOCHE campaigns. For the TOA analysis, only the runs for which the least square analysis converged to a result were included in the averaging. For the frequency analysis, a minimum SNR threshold of 3 dB was employed to avoid unnecessary noise content. Plotted together with these traces are the weighted average signal magnitudes for oblique AM heating at 2, 3, and 4 kHz, and for the LOS and IR signal components. It can be seen that while the 360° GM sweep typically produces larger ELF/VLF signal magnitudes than oblique AM heating, at 180° BP/GM sweeping *always* produces larger ELF/VLF signal magnitudes than oblique AM heating. Figure 4-9 shows the campaign-averaged ratio of the ELF/VLF signal magnitude generated using 360° GM to the maximum BP/GM signal magnitude observed as a function of arc length. BP/GM produces larger (at least 0.5–2.5 dB) signal magnitudes at all frequencies, although it produces the largest gains (3–5 dB) at lower frequencies.

In order to better display the phased array nature of the BP/GM source region, the amplitude and phase contribution produced by a particular source element is calculated by differentiating the TOA observations as a function of arc length. In order to achieve reasonable SNR levels, 30°

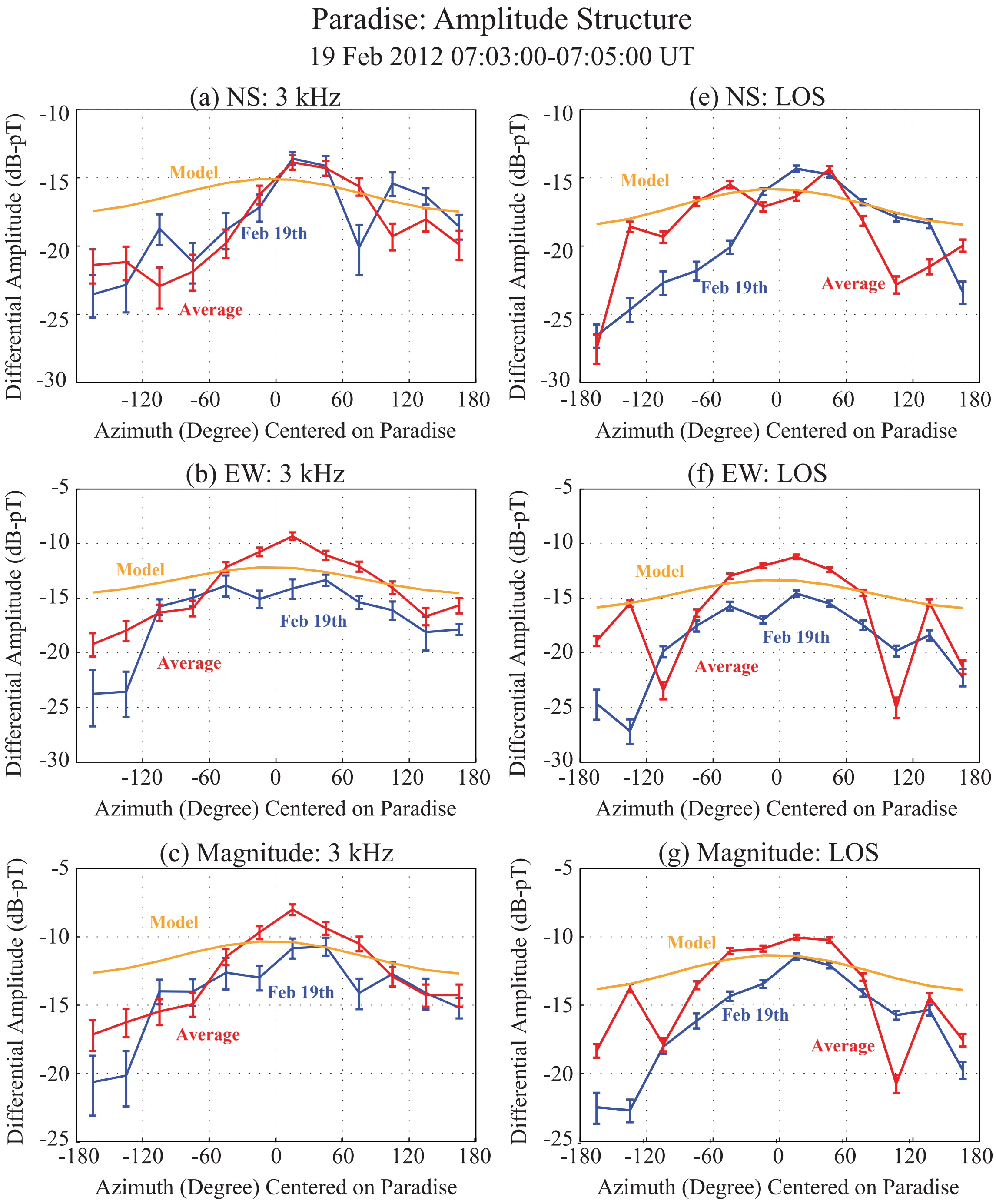

Figure 4-10. The amplitudes (Left: 3 kHz, Right: LOS) at Paradise are plotted as a function of azimuth centered at Paradise. 0° indicates azimuthal direction toward Paradise. 30° arc lengths are integrated to calculate the amplitude and phase. The orange line is the same model result used in Figure 4-5.

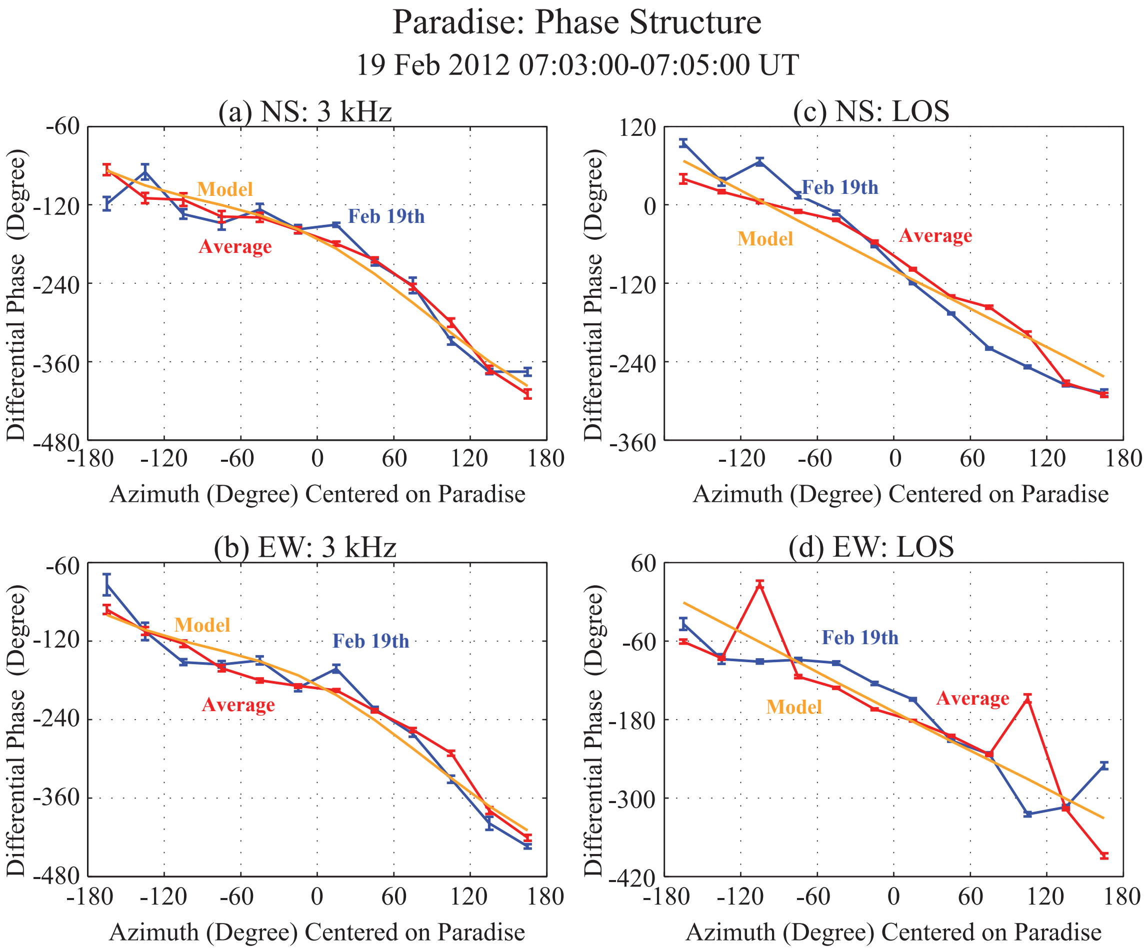

Figure 4-11. The phases (Left: 3 kHz, Right: LOS) at Paradise are plotted as a function of azimuth centered at Paradise. 0° indicates azimuthal direction toward Paradise. 30° arc lengths are integrated to calculate the amplitude and phase. The orange line is the same model result used in Figure 4-5.

arc lengths are used. Similarly, the amplitude and phase over 30° arc length are calculated in the frequency domain. The LOS and 3 kHz amplitude and phase observed at Paradise are plotted in Figures 4-10 and 4-11. We observe ∼5–13 dB amplitude differences, which is somewhat larger than past observations (6-10 dB observed by *Barr et al.* [1987] and 6-8 dB observed by *Cohen et al.* [2010a]). The portion of the circle directed toward the receiver (up to 120° arc length) produces by far the largest signal amplitudes, and the portion of the circle directed away from the receiver (>240° arc length) produces the lowest amplitudes. These observations support *Moore* *and Rietveld* [2009]'s prediction that the portion of the circle closest to the receiver dominates the received amplitude.

The interpretation of the phase for the LOS component and the 3 kHz component is somewhat different. Using the TOA method, the phase of the measurement represents the ELF/VLF source phase, whereas in the frequency domain, the phase represents the phase of the source plus the propagation phase. The phase shown in Figures 4-11(c) and (d) is the source phase. The phase approximately follows a linear progression (dashed line) due to the timing offset of heating by sweeping. The fluctuation along the linear phase line shows a relative source phase difference due to the ionospheric response, or to differences in the HF beam pattern as a function of azimuth. On the other hand, Figures 4-11(a) and (b) show the phase structure at 3 kHz which include the phase contribution due to propagation (including ionospheric reflections).

4.1.3 BP/GM Analysis

Based on the observations reported in the previous section, it is clear that the amplitude of the received ELF/VLF signal depends on the area of the source region, the relative phasing of individual source elements, the nature of oblique HF heating, and the effective duty cycle. Previous analyses have typically compared GM heating to vertical AM heating. We provide the following expression to convert vertical AM heating to GM, and we analyze each of its individual components:

$$A_v \cdot \frac{A_o}{A_v} \cdot D_{GM} \cdot \frac{S_{GM}}{S_o} \cdot \frac{\sum_{i=1}^{N} A_i}{N \max(A_i)} \cdot \frac{\left|\sum_{i=1}^{N} A_i e^{j\phi_i}\right|}{\sum_{i=1}^{N} A_i} = \left|\sum_{i=1}^{N} A_i e^{j\phi_i}\right| \tag{4–1}$$

where A_v is the amplitude produced by vertical AM heating with 50% duty cycle, A_o is the amplitude produced by oblique AM heating with 50% duty cycle aimed toward the receiver, D_{GM} accounts for the relative signal level change produced by the effective duty cycle relative to 50% duty cycle, and S_{GM} and S_o are the 3-dB heated areas for GM and oblique AM. A_i and ϕ_i are the amplitude and phase produced by the ith source element (around the circle), and N is the total number of source elements considered.

Stepping through each of the terms from left to right, A_o/A_v converts the vertical AM (50% duty cycle) signal to an oblique AM signal, and we will refer to this as the oblique heating effect.

D_{GM} coverts the oblique AM 50% duty cycle signal to an oblique AM $X\%$ duty cycle signal. At this point, X is unknown because the effective duty cycle of the GM sweep is unknown. We will refer to this effect as the duty cycle effect. The last remaining effect is the increased area of the GM sweep. In addition to simply increasing the area, denoted by the term S_{GM}/S_o, the amplitude generated changes as a function of azimuth due to the directionality of oblique heating. This effect is accounted for using the $\frac{\sum_{i=1}^{N} A_i}{N \max(A_i)}$ term, which we will refer to as the oblique directionality effect. The relative phasing of the elemental source components is also important and accounted for using the $\frac{\left|\sum_{i=1}^{N} A_i e^{j\phi_i}\right|}{\sum_{i=1}^{N} A_i}$ term. We will refer to this component as the phasing effect. In the end, combining all of these effects produces the final GM amplitude: $\left|\sum_{i=1}^{N} A_i e^{j\phi_i}\right|$. Note that the oblique directionality effect and the phasing effect are produced as side-effects of directing the HF beam to different locations in order to increase the total heated area, meaning that the value ascribed to each effect is only valid when also accounting for the 17.9 dB enhancement due to the increase in area.

All of the terms described above can be calculated based on our observations. The ratio A_o/A_v can be derived statistically, S_{GM}/S_o is known for a given HF transmission frequency and A_i and ϕ_i can be extracted from the data shown in Figures 4-10 and 4-11. D_{GM} is calculated after simplifying the Equation 4–1:

$$D_{GM} = \frac{S_o}{S_{GM}} \cdot \frac{N \max(A_i)}{A_o} \tag{4–2}$$

Duty cycle refers to the ratio of HF heating time to the HF modulation period. Past studies show that the ELF/VLF signals are maximized around ∼40% [*Barr and Stubbe*, 1991b; *Barr et al.*, 1999; *Cohen et al.*, 2010a] and that lower duty cycles tend to be more efficient [*Barr and Stubbe*, 1991b; *Barr et al.*, 1999; *Jin et al.*, 2012]. Estimating the duty cycle for GM can become very complex, since the heating time varies within the heated region as a function of distance from the center of the circle to the heated region by treating GM as a continuous circle sweep. The duty cycle for GM ranges from 5–20% as a function of radius in the circle [*Cohen*, 2009], for instance. *Cohen* [2009] also estimate the average duty cycle as ∼12% by taking a ratio of an single HF beam area (3-dB beamwidth) to an entire GM circle area.

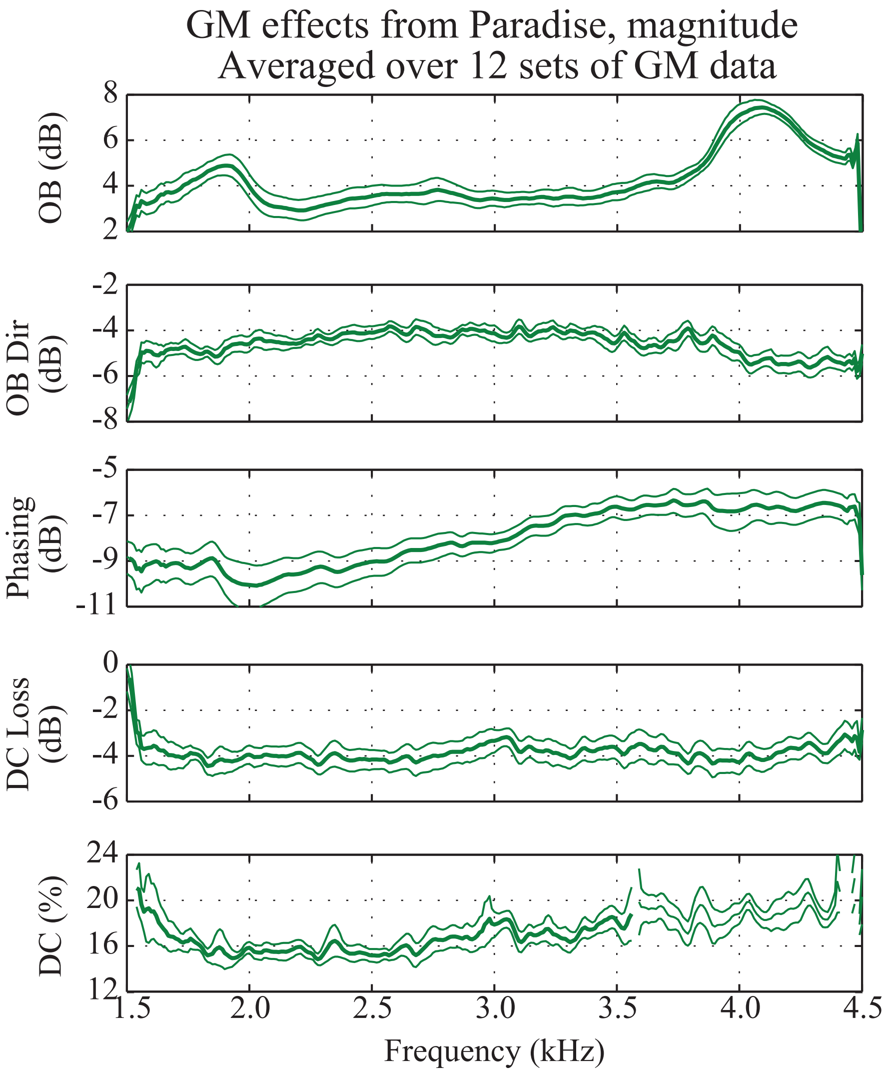

Figure 4-12. Quantified effects contributing to the amplitude of ELF/VLF wave generation, averaged over the two campaigns.

The averaged analysis results are shown in Figure 4-12, noting that the 17.9 dB increase in area, which is constant as a function of frequency is not shown. The dramatic increase in the area of the GM transmission is the most important factor increasing the received ELF/VLF amplitude. The second most important factor is the phasing effect, which decreases the received ELF/VLF amplitude significantly (by ∼10 dB) at low frequencies, and to a lesser extent (6–8 dB) at higher frequencies. The oblique heating effect is the next most important factor, producing +2–5 dB gains at lower frequencies and +6–8 dB gains at higher frequencies. At low frequencies, the oblique heating effect is almost, but not quite, canceled by the oblique directionality effect that only occurs together with a massive increase in area. The oblique directionality effect is characterized by a 3–5 dB loss. The last effect is the duty cycle effect: the lower effective duty cycle of the GM transmission compared to the 50% duty cycle AM transmission reduces the received ELF/VLF amplitude by ∼3–5 dB. As a side note, the ∼3–5 dB duty cycle effect corresponds to an effective duty cycle of 16±0.5% at lower frequencies and 18±2% at higher frequencies for the GM format, which seemingly corresponds to the 60° beamwidth of the HF beam divided by the 360° full circle (16.7%).

Based on this analysis, increasing the heated region area provides the primary gain factor for the GM format. Combining the effects of area, oblique directionality, and phasing, increasing the area has an overall effect of +7.9–11.9 dB on the received ELF/VLF signal amplitude. While the duty cycle and oblique heating effects nearly cancel at low frequencies, oblique heating produces larger (an additional 3 dB) gains at higher frequencies that are not matched by the duty cycle effect. For a given set of ionospheric heating points, it is clear that the phasing effect is the primary effect to mitigate, particularly at low frequencies, and that the duty cycle effect is important, although secondary.

4.2 Optimized Heating Order for BP/GM (Constant Duration)

In the preceding sections, TOA analysis has proved to be useful, although not entirely necessary. In this section, the propagation delays and source phases derived using TOA observations are leveraged to provide an optimized heating location order. Using the spatial amplitude and phase TOA measurements shown in Figures 4-10 and 4-11, we predict the ELF/VLF amplitude that would result using a different heating order. The different heating order controls the phase structure of the ELF/VLF source region. We consider two optimizations: 1) simply maximize the received ELF/VLF amplitude, and 2) maximize the ELF/VLF amplitude such that the heating order is symmetric.

For this exercise, the duty cycle (or equivalently heating duration) for each source segment is the same as during the experiment – we use the amplitude directly from Figure 4-10 and modify the

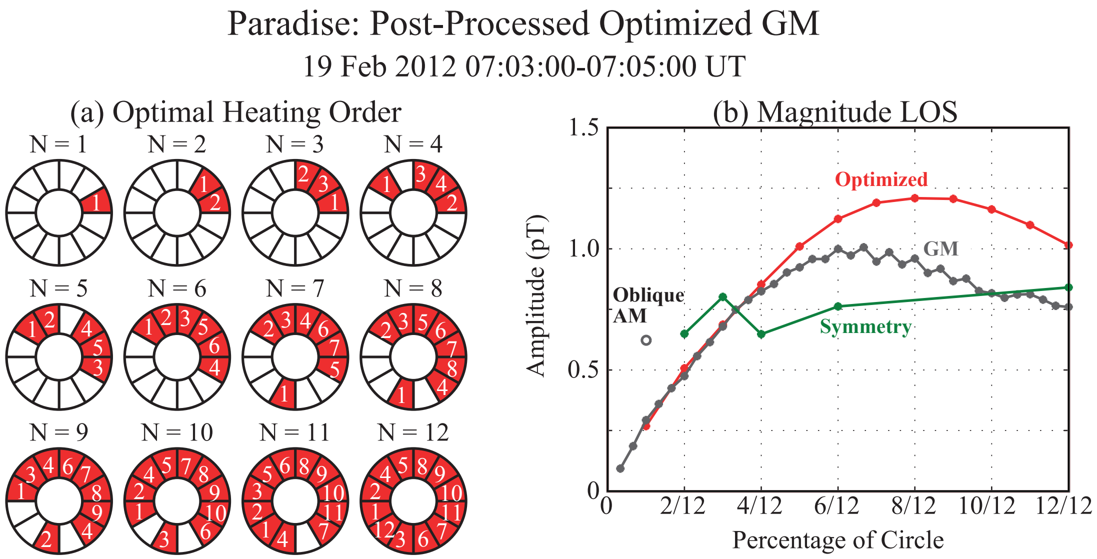

Figure 4-13. The amplitude post-processed to optimize heating order of GM. (a): Optimal heating order with different numbers of heating locations. (b): Optimized amplitudes (red) are compared with those of GM circle (gray) and symmetric heating (green). For symmetric heating, the locations are equally apart in a circle.

phase from Figure 4-11 according to the change of order. Figure 4-13 shows the optimal heating order for *N* heating locations in the left panel and the resulting optimized amplitudes in the right panel. The optimized and symmetric results are compared with those for oblique AM and GM. The symmetric heating is constrained to heat the segments in an order that produces an approximately symmetric ELF/VLF beam pattern. For the symmetric format, however, we allow the duty cycle to increase so that the 100% of the modulation cycle is available for heating.

The maximum amplitude is achieved when only 8 out of 12 arc segments are used. The amplitude is increased by 4 dB compared to GM (360°) and the efficiency is increased by 7 dB. The optimal heating order starts with the segments farther away from Paradise and ends with closer segments in order to best match the propagation phase. At the lower number of the heating segments, the selection of the segments is prioritized to the closer segments to utilize the higher amplitudes.

For symmetric heating, the amplitude remains in the same range (~0.6–0.8 pT) for any percentages of the circle heated. The optimal duty cycle is the same as for the GM format – no beam-off time, except at 2/12% of the circle. To make symmetric heating pattern, each segment is assigned equally a fraction of the modulation period and within the assigned time the duty cycle and off-time are adjusted to maximize the total amplitudes. For this reason, the maximum amplitude is generated by the GM format because the larger duty cycle produces the larger amplitude up to ∼40%. At 2/12% of the circle, each of the two chosen segments are assigned 40% of the modulation period, and the beam is turned off for the remaining time.

The discrepancy of the magnitude at GM (full circle) and 12/12 on "Symmetry" is from the different direction of the sweep rotation. To find an optimal symmetric heating, we estimate the magnitudes for all possible symmetric pattern that can be done for one rotation of the circle. Even though the amplitude and phase structures are asymmetric shown in Figures 4-10 and 4-11, the change of rotation direction makes slight difference in the total amplitude experimentally reported by *Cohen et al.* [2008].

In this chapter, we have demonstrated a method to optimize the order of heating locations, assuming that the duration of heating at each location is pre-determined. In the next chapter, we consider a full optimization of the ELF/VLF source region, allowing the start timing and duration for each heating location to vary.

CHAPTER 5
OPTIMIZATION OF ELF/VLF AN PHASED ARRAY

The previous chapter increased the ELF/VLF amplitude generated using a ELF/VLF phased array by changing the order of heating locations while keeping the duration of heating at each location the same. In this chapter, we experimentally investigate the effect of duty cycle as a function of the source location (relative to the receiver location). As a result, we are able to perform an optimization that considers the best ordering of heating location together with the best heating durations for each individual heating locations. Solutions are constructed using TOA analsyis of ELF/VLF amplitudes and phases observed when the HF beam is aimed at eight different azimuthal directions with 15° off-zenith.

5.1 Optimization Experiment Description

To measure the amplitude, phase, and propagation delay as a function of ionospheric heating location, the HF beam is aimed 15° off-zenith in eight azimuthal directions. The azimuthal directions are separated by 45°, from 14° to 329° east of north. Each beam was transmitted with amplitude modulation with 50% duty cycle. In order to investigate the effect of duty cycle, the HF beam was directed at two heating locations alternatively (81° and 261° azimuth at 15° off-zenith), and the duty cycle changed from 5% to 75% in 5% steps. The transmissions were performed closely in time so that accurate comparisons could be made. All transmissions were at 3.25 MHz (X-mode) and at full power (3.6 MW, 84.7 dBW). The beam was modulated with an AM square wave and the modulation frequency linearly varied from 1 kHz to 5 kHz with a 1 kHz/sec slope.

For this analysis, we focus on ELF/VLF observations performed at Paradise.

5.2 Experimental Observations

During the BRIOCHE campaign in March, 2013, ELF/VLF waves were generated with excellent SNR (>21 dB) for different azimuths and duty cycles. The Kp Index was 4- and the Gakona Magnetometer registered magnetic flux variations of $<$125 nT. The observed ELF/VLF waves at Paradise are presented in this section and are used to optimize the heating location and order.

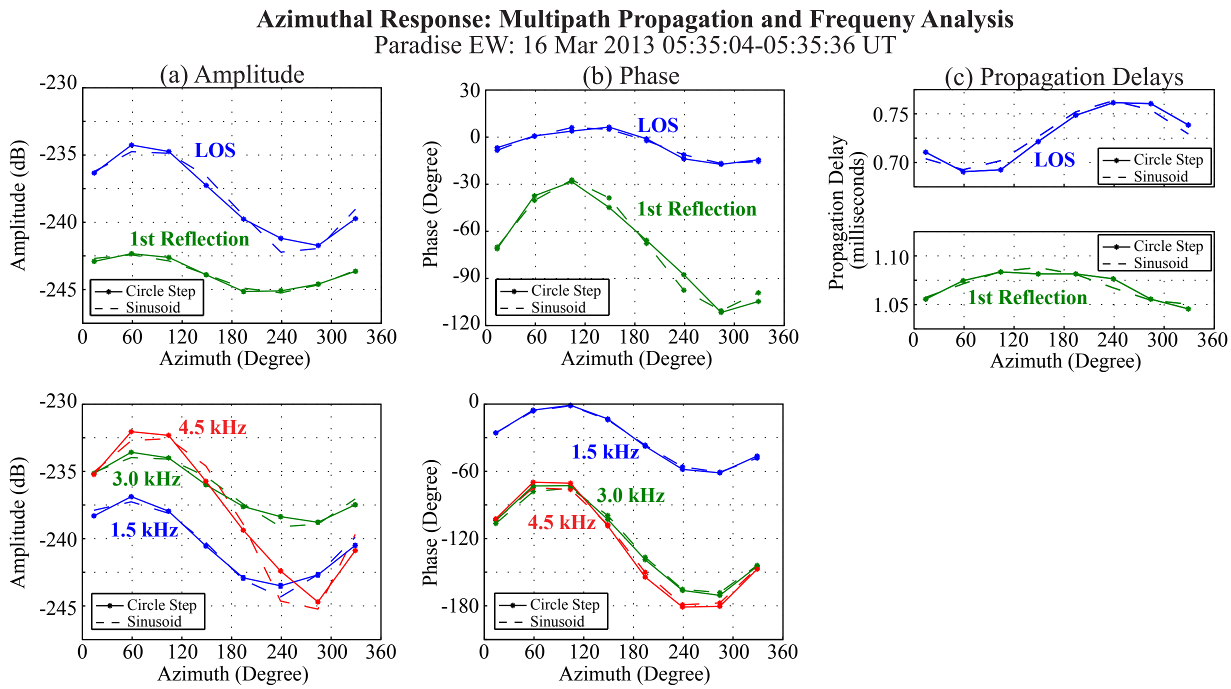

Figure 5-1. (a) Amplitude, (b) phase and (c) propagation delays as a function of azimuth direction. The solid line is the observation and the dash line is a sinusoid.

5.2.1 ELF/VLF Observations vs. Azimuth

The observed ELF/VLF signals for 8 azimuthal directions are shown by solid lines in Figure 5-1. The amplitudes and phases are shown for two propagation paths (LOS and 1st IR) and for three different frequencies (1.5, 3.0, 4.5 kHz) in addition to propagation delays for LOS and 1st IR. The amplitudes of the EW signals are larger than the NS signals by ∼38 dB. Since EW component of the observed ELF/VLF signal is dominant, we focus on the EW component for the rest of this chapter.

The amplitudes for the LOS and IR propagation paths and for three frequencies have a similar shape: the amplitude is largest when the beam is aimed toward the receiver (Paradise at 81°) and smallest when it is aimed away from the receiver. The amplitude difference as a function of azimuth is ∼5–8 dB which is consistent with past observations [*Barr et al.*, 1987; *Cohen et al.*, 2010b]. The phases for the frequencies and propagation paths are interpreted differently. The phases for the frequency response include the ELF/VLF source phase as well as the propagation phase (including effects of the waveguide), while the phases for the LOS component represent only the ELF/VLF source phase.

The propagation delay for each propagation path is shown in the most right panel in Figure 5-1. The LOS propagation delay follows a straightforward interpretation: heating locations closer to the receiver produce shorter propagation delays. The 1st IR propagation delays are not so simple, however. The propagation delay seems longer when the heated location is to the south (>90° and <270° az) and shorter when it is to the north. The observation may be explained by different ionospheric conditions or incident angles, or a mix of those effects, but it is most likely due to the frequency-dependent reflection coefficients for the air-ionosphere interface. The IR components contain a multitude of physical effects that are not considered in this dissertation, and it will have to suffice to approximate their properties in order to get the best estimate of the LOS signal component.

All components (amplitude, phase, and propagation delay) of the received ELF/VLF signals vary sinusoidally with azimuth. The dashed line in Figure 5-1 is a sinusoidal line provided for comparison. In subsequent sections, this fact will be used to estimate the effect of duty cycle based on measurements at only a few heated locations.

5.2.2 ELF/VLF Amplitude vs. Duty Cycle

The received ELF/VLF amplitude and phase as a function of duty cycle are shown in Figures 5-2. The amplitudes and phases are normalized by the signal with 50% duty cycle. The amplitude and phase plots are compared with an analytical expression for the effect of duty cycle [*Barr and Stubbe*, 1991b] using a heating constant-to-cooling constant ratio of 0.282.

The received ELF/VLF amplitude increases with duty cycle until it reaches a maximum near 30–40% duty cycle, and at larger duty cycles it decreases with increasing duty cycle. The maximum amplitudes are 30–40% larger than at 50% duty cycle. The maximum amplitude occurs at lower duty cycles because the time constant for electron heating is shorter than that for electron cooling [*Barr and Stubbe*, 1991b; *Cohen et al.*, 2010b]. The phases for different frequencies and

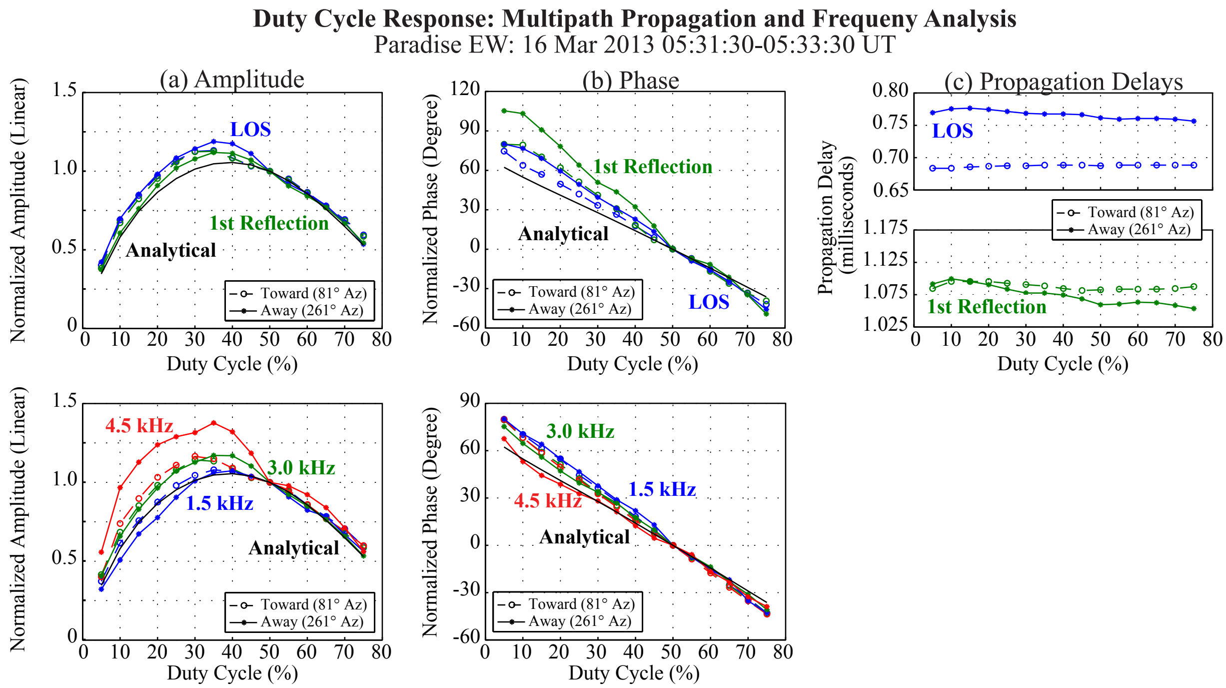

Figure 5-2. (a) Amplitude, (b) phase and (c) propagation delays as a function of duty cycle. The amplitudes and phases are normalized by the signal with 50% duty cycle.

propagation paths are also compared with the analytical case. The phase of all components in Figure 5-2 vary almost linearly with duty cycle: they deviate from linear by only ±10°.

Most importantly, the ELF/VLF amplitude dependence on duty cycle additionally depends upon the location of the ELF/VLF source with respect to the receiver location. The responses are slightly different when the HF beam is directed away from the receiver and toward the receiver. During the optimization process, we will desire knowledge of the duty cycle response at all eight heating locations. Based on the observations presented in the previous section, we estimate this response as a function of azimuth by fitting a sinusoid to the amplitudes observed (as a function of duty cycle) for 81° and 261° azimuth.

The propagation delay as a function of duty cycle is shown in the right panel of Figure 5-2. The propagation delays for the LOS component are all within ±10 μsec of each other. This translates to a maximum source height difference of only ±2 km assuming that the source is located at the center of the HF beam. The propagation delays for the first IR component vary by ±25 μsec. Once again, we attribute the variation observed in the first IR component to ionospheric conditions:

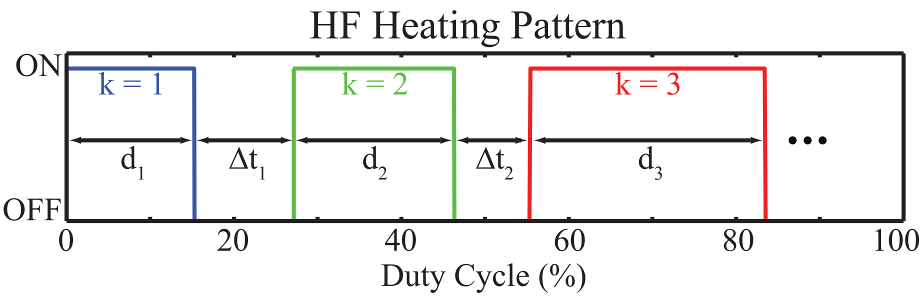

Figure 5-3. Diagram of HF heating pattern

most likely the frequency-dependent reflection coefficients at the air-ionosphere interface affect this measurement.

5.3 Optimization of Beam Painting

Given the observations presented in the two previous sections, we provide an optimization for the ELF/VLF amplitude at Paradise that accounts for different ON/OFF times at eight heating locations, and different heating location ordering. To accomplish this, the observed ELF/VLF amplitudes at the eight heating locations (shown in Figure 5-1) are modified by the duty cycle, and the phase is modified by the propagation delay, duty cycle, and time offset due to the start timing of the heating. As is shown in Section 3.5.1, a linear summation of these signals approximates the total received signals quite well. The total received amplitude can be described:

$$S = \left| \Sigma_{k=1}^{N} A_k e^{j\phi_k} D_k(d_k) e^{-j2\pi \Sigma_{m=1}^{k}(d_{m-1}+\Delta t_{m-1})} \right| \tag{5–1}$$

where N is the total number of heating locations, A_k and ϕ_k are the amplitude and phase of the kth ELF/VLF source (the subscript indicates the heating location) at 50% duty cycle, D_k is the amplitude and phase relative to 50% duty cycle as a function of duty cycle, d_k, and Δt_k is the time that the HF beam is off between the kth and $(k+1)$th heating locations. These parameters are diagrammed in Figure 5-3. There is no unit in Δt_k because Δt_k is the fraction of the modulation period. For TOA analysis, the above equation is modified to:

$$S = \max \left| \left\{ \Sigma_{k=1}^{N} A_k e^{j\phi_k} D_k(d_k) \operatorname{sinc}\left[B(t-\tau_d)\right] e^{j2\pi f_c(t-\tau_d)} e^{-j2\pi \Sigma_{m=1}^{k}(d_{m-1}+\Delta t_{m-1})} \right\} \right| \tag{5–2}$$

where B is the bandwidth of the ramp, τ_{d_k} is the propagation delay at the duty cycle d_k, t is the time vector $(t_1, t_2, t_3, \ldots)$, max finds the maximum value as a function of t, and the sinc function is defined as:

$$\operatorname{sinc}(x) = \begin{cases} 1 & \text{if } x = 0 \\ \frac{\sin(\pi x)}{\pi x} & \text{otherwise} \end{cases}$$

In TOA analysis, the sinc function arises as a result of rectangular windowing in the frequency domain. The width of the sinc function is determined by the bandwidth of the rectangular window.

The goal is to maximize th amplitude S by optimizing the duty cycle and the HF heating off time with a combination of the heating locations. The optimization expression is:

$$\begin{aligned} \text{maximize} \quad & S \\ \text{subject to} \quad & \sum_{k=1}^{N} d_k + \sum_{k=1}^{N-1} \Delta t_k <= 1, \\ & d_k >= 0, \\ & \Delta t_k >= 0. \end{aligned} \tag{5–3}$$

The optimization is not straightforward due to the trade-off between phase interference and duty cycle. For instance, with $N = 2$, we may choose the closest heating locations to the receiver for the largest amplitudes. However, for the signals to interfere constructively, each duty cycle has to be short and the amplitudes generated at each location become smaller; thus the total amplitude may become smaller.

To solve the optimization problem, we apply a gradient descent method which iteratively updates the parameters according to the derivatives of S_{VLF}. To make sure the solution is the global maximum, the result of the gradient descent method is compared to that of a direct search method which scans through all possible combination of the parameters. Due to the heavy computational

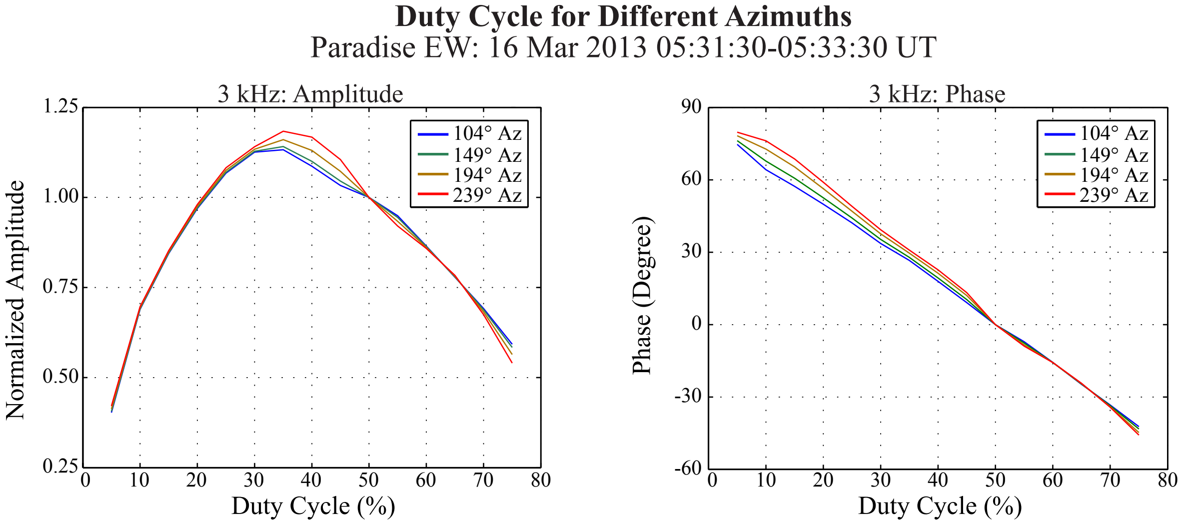

Figure 5-4. Duty cycle dependence on azimuth.

requirements, the direct search can compute S_{VLF} only up to $N = 5$ in a reasonable time frame. It suffices to observe a typical trend of S_{VLF} and to make sure S_{VLF} converges to the global maximum for $N \geq 6$.

5.3.1 Duty Cycle Dependence vs. Azimuth

The ELF/VLF amplitude dependence on duty cycle also depends upon the location of the heated region relative to the receiver location (Figure 5-2). In order to optimize the signals generated at the eight azimuthal locations, we estimate the amplitudes and phases as a function of duty cycle for the azimuthal locations using the observations shown in Figure 5-2. The result corresponds to the function, $D_k(d_k)$ in Equations (5–1) and (5–2).

To estimate the ELF/VLF amplitude dependence on duty cycle, we estimate that both the amplitudes and the phases vary sinusoidally as a function of azimuth. The peaks of the sinusoids are determined by the experimental data. For each duty cycle, the sinusoidal curves are estimated using all eight azimuthal directions. Results are shown in Figure 5-4. It is worth noting that the dependence of ELF/VLF amplitude on duty cycle varies with time. For instance, while it would be ideal to measure the duty cycle dependence all azimuthal angles, it is likely that ionospheric conditions have changed by the time the measurement has completed. Using the sinusoidal assumption allows for rapid accounting of the duty cycle effect.

5.3.2 Gradient Descent Method

The gradient descent method is used to iteratively optimize for the maximum amplitude (or minimum error to the maximum amplitude) in Equation (5–1) and (5–2) [*Gill et al.*, 1981]. S_{VLF} converges to the maximum amplitude with a given heating order, and the largest amplitude of all the possible orders is determined. The variables to be optimized are $d_1, d_2, \ldots d_N$ and $\Delta t_1, \Delta t_2, \ldots \Delta t_{N-1}$, which are the heating duration divided by the total duration (i.e., duty cycle) for each heating location and the length of time for which the HF beam is off before heating at the next location.

The iterative method starts with an initial guess for each of the unknown variables. Subsequently, the variables are updated by using:

$$\beta^{(i+1)} = \beta^{(i)} + \mu J \tag{5–4}$$

where β is a set of variables (i.e, $[d_1, \ldots d_N]$ and $[\Delta t_1, \ldots \Delta t_{N-1}]$), the superscript $^{(i)}$ is the iteration count, μ is the step size and J is a set of the partial derivatives of S with respect to each variable. The step size is adjusted by the user so that the variables converge. The derivatives are computed numerically every iteration.

The variables must satisfy the optimization constraints in Equation (5–3). To simplify the equation, Equation (5–3) is re-written with β:

$$\begin{aligned} \text{maximize} \quad & S \\ \text{subject to} \quad & \sum_{k=1}^{2N-1} \beta_k <= 1, \\ & \beta_k >= 0,\ k = 1, 2, \ldots 2N-1 \end{aligned} \tag{5–5}$$

To meet the constraints, β_k is forced to be zero when it becomes negative, and J is modified when $\sum \beta^{(i+1)} = \sum \beta^{(i)} + \mu J > 1$. The modification is fairly simple. When J has negative elements and

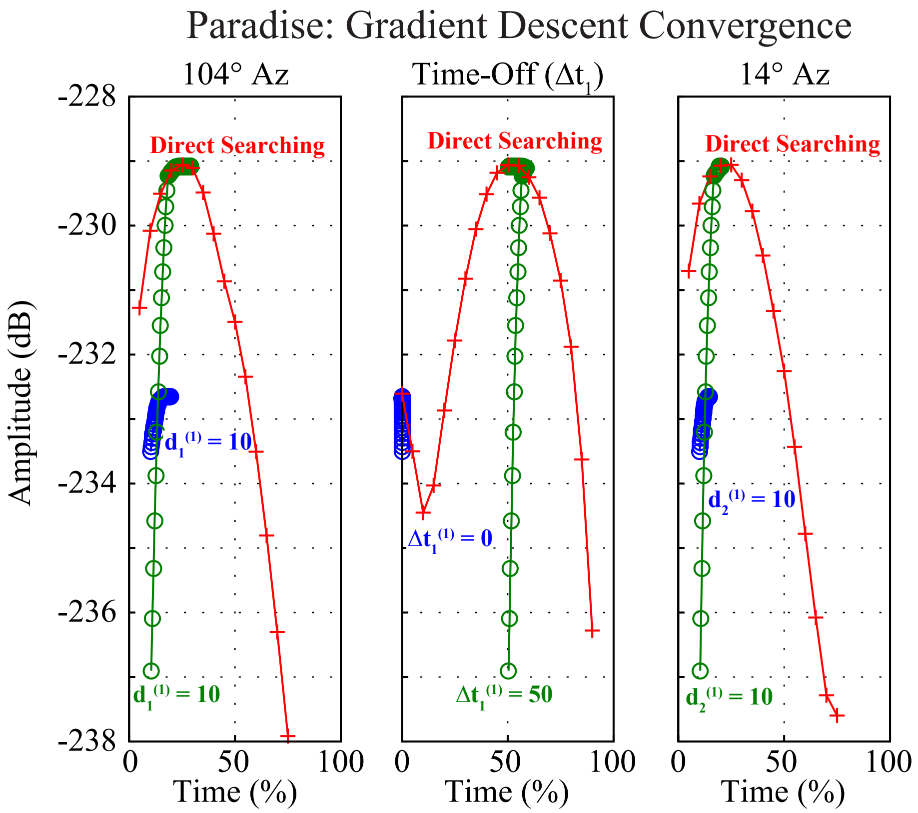

Figure 5-5. Convergence of parameters (on time and off time) to optimize for the maximum amplitude using Gradient descent method. Blue and green trace are the updated parameters with different initial values. Red trace is the maximum amplitude from direct searching method.

β's elements at the same indices are positive, J's positive elements are modified to zero and the J's negative elements remain the same. When this is not the case, we keep the largest of J's elements as is and replace the smallest of J's elements with the largest element that is negated. The other elements of J are modified to zero. The modified J has a positive value for the element of β which contributes the most to increase S and has a negative value for the element of β which contributes the least to increase S. By meeting the constraints with this modification, S will continue converging to the maximum value without $\sum \beta^{(i+1)}$ exceeding 1.

The convergence of the gradient descent method is shown in Figure 5-5 with comparison to the results of the direct searching method. The direct searching method scans through all the possible combinations and locates the global maximum. Figure 5-5 shows that the gradient descent method converges to the global or local maximum depending on initial values. In Figure 5-5, the heating direction is 104° and 14° Az. The red trace shows the maximum amplitude at a length of time spent on that location. The global maximum for this heating and locations is 229 dB for $d_1 = 25\%, d_2 = 25\%, \Delta t_1 = 50\%$. There is also local maximum at $\Delta t_1 = 0\%$. The blue and green traces are updated each iteration with different initial values for Δt_1, one of which is 0% and the other of which is 50%. Depending on these initial values, the trace converges to either the local or global maximum. Since we cannot tell which set of initial value converges to the global maximum, the global maximum is determined by comparing the converged amplitudes with different sets of the initial values. It is important to use all possible initial values that converge to the maxima, otherwise we may not be able to identify the global maximum. In the next section, we discuss how to determine the initial values.

5.3.3 Determination of Initial Values

The initial values that converge to any maxima are

$$\begin{cases} d_{1,\ldots,N} = 0.1 \\ \Delta t_{1,\ldots,N} = 0 \end{cases}$$

Or

$$\begin{cases} d_{1,\ldots,N} = 0.1 \\ \Delta t_k = 0.4 & k = i \\ \Delta t_k = 0 & k = 1,\ldots,N, k \neq i \end{cases}$$

These initial values indicate that the duty cycle for heating is operated in an efficient range (i.e., the lower duty cycle is more efficient), and time-off periods between two heating locations are zeros for the signals to constructively add each other. The large time-off period such as 40% is equivalent to the zero time-off period between two locations if $\sum_{k=1}^{N} d_k + \sum_{k=1}^{N-1} \Delta t_k = 1$, just like the case in Figure 5-5. 25% of a period for heating at 104° az, 50% for turning off and 25% for heating at 14° az, is equivalent to 25% for at 14° az, 25% for at 104° az and 50% for turning off – just the order has been changed. In this section, we discuss how the zero time-off maximizes the amplitude.

To simplify the discussion, we analyze a case of heating two locations with a linear phase. The phase of the two signals (Φ_1 and Φ_2 in degrees) are,

$$\begin{aligned}
\Phi_1 &= \varphi_1 + (90 - 180d_1) \\
\Phi_2 &= -360(d_1 + \Delta t_1) + \varphi_2 + (90 - 180d_2) \qquad (5\text{–}6)
\end{aligned}$$

where ϕ_1 and ϕ_2 are the phases of the signals at each location with 50% duty cycle, d_1 and d_2 is the duty cycle at each location, and Δt_1 is the time off between heating the two locations. $(90 - 180d_k)$ modifies φ_k with d duty cycle (Equation (5–1) or (5–2)), and $-360(d_1 + \Delta t)$ accounts for the time delay of heating at the 2nd location. The relative phase for Φ_1 and Φ_2 is

$$\begin{aligned}
\Delta\Phi &= \Phi_2 - \Phi_1 \\
&= \varphi_2 - \varphi_1 - 180\left(d_1 + \Delta t_1 + d_2\right) - 180\Delta t_1 \\
&= \Delta\phi - 180\left(d_1 + \Delta t_1 + d_2\right) - 180\Delta t_1 \qquad (5\text{–}7)
\end{aligned}$$

where $\Delta\phi = \varphi_2 - \varphi_1$. For the signals to interfere constructively, $\Delta\Phi$ is zero. So,

$$0 = \Delta\phi - 180\left(d_1 + \Delta t_1 + d_2\right) - 180\Delta t_1 \qquad (5\text{–}8)$$

which reduces to,

$$\Delta t_1 = \frac{\Delta\phi}{360} - \frac{1}{2}\left(d_1 + d_2\right) \qquad (5\text{–}9)$$

The equation above is plotted with constraints ($d_1 > 0, d_2 > 0, \Delta t_1 > 0, d_1 + d_2 + \Delta t_1 \leq 1$) in Figure 5-6. The gray shade indicates where the constraints are satisfied. The color lines show the Equation (5–9) at different relative phase, $\Delta\phi$. To achieve a constructive interference and the longest total heating time (maximum $d_1 + d_2$) is an intersection of a color line and either $\Delta t_1 = 0$ or $d_1 + d_2 + \Delta t_1 = 1$.

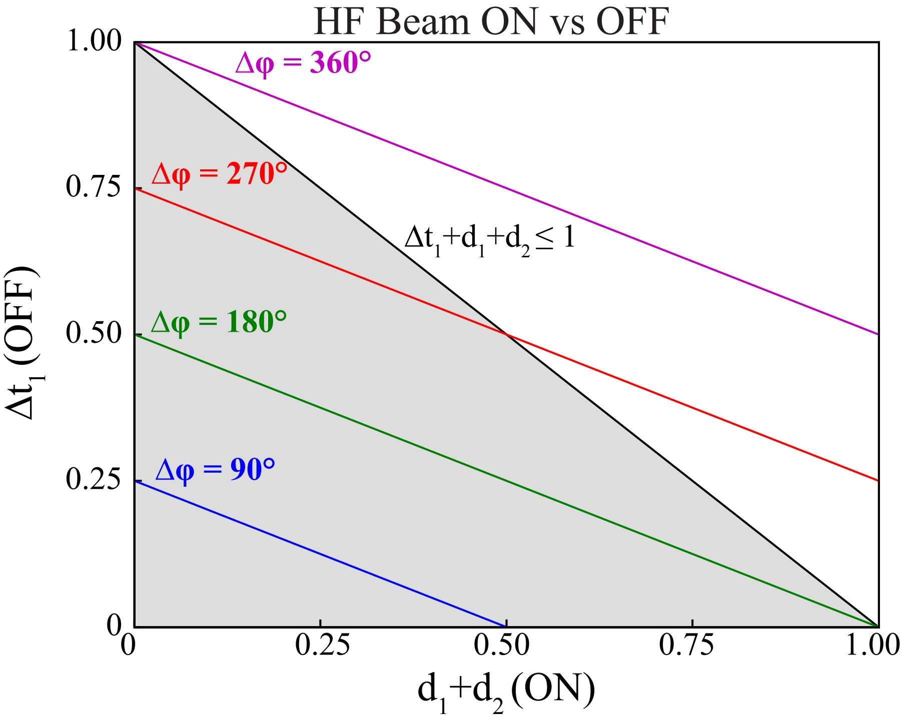

Figure 5-6. Off-time between the 1st and 2nd heating location against total duty cycle of 1st and 2nd heating location. The gray shade indicates the region where the constraint meets. Different color lines indicate the combination of Δt_1 and $d_1 + d_2$ that makes in-phase with different relative phase of the two location.

Although the longest total heating time does not necessarily maximize the amplitudes due to the non-linear relation of amplitudes over duty cycle, it is likely to maximize the amplitude especially when $d_1 + d_2 < 0.8$. The amplitude increases monotonically up to $\sim$40% duty cycle; thus the optimal total amplitude of the two locations increase until both of the duty cycle reach to $\sim$40% when they are in-phase. In our experimental observation, the relative phase, $\Delta\phi$, is from 0° to 120° or from 240° to 360° depending on the order of heating locations. This yields that optimal $d_1 + d_2$ is less than 0.72.

I have discussed how to determine the initial values with two heating sections. Similarly, it generally works with N heating locations. An optimal time-off period between the first two heating locations is zero to be in-phase, and a next time-off period between the 2nd and 3rd heating

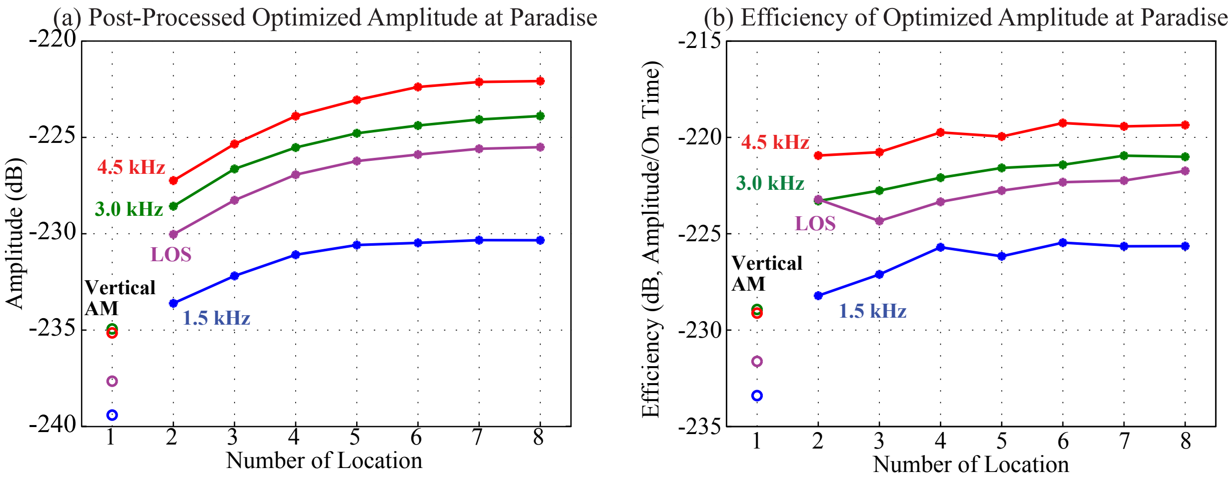

Figure 5-7. Optimized amplitude (a) and efficiency (b) as a function of number of heating locations.

locations is also zero to produce in-phase radiation. Then, the first three locations are all in-phase and this sequence continues to *N*th location.

Zero time-off periods between heating locations do not necessarily maximize the received ELF/VLF amplitude. Nevertheless, such an approximation suffices for an initial guess. To determine the optimized amplitude at a given order of heating locations, we compare the converged amplitudes from all the sets of initial values.

5.3.4 Optimization Result and Analysis

The results for optimized ELF/VLF amplitudes are shown in Figure 5-7. Compared to vertical AM heating with 50% duty cycle, the amplitude is increased by 10–15 dB and the efficiency is increased by 7–13 dB. Compared to geometric modulation (circle) shown in the previous chapter, the amplitude is increased by ~7 dB and the efficiency is increased by ~11 dB. The comparisons are shown in Table 5-1.

The largest optimized amplitude for LOS and all frequency components are produced with eight heating locations (out of eight considered locations). However, the amplitude converges as the number of heating locations increases, indicating that increasing the number of heating locations increases the received ELF/VLF amplitude to a lesser extent as the number of heating locations increases.

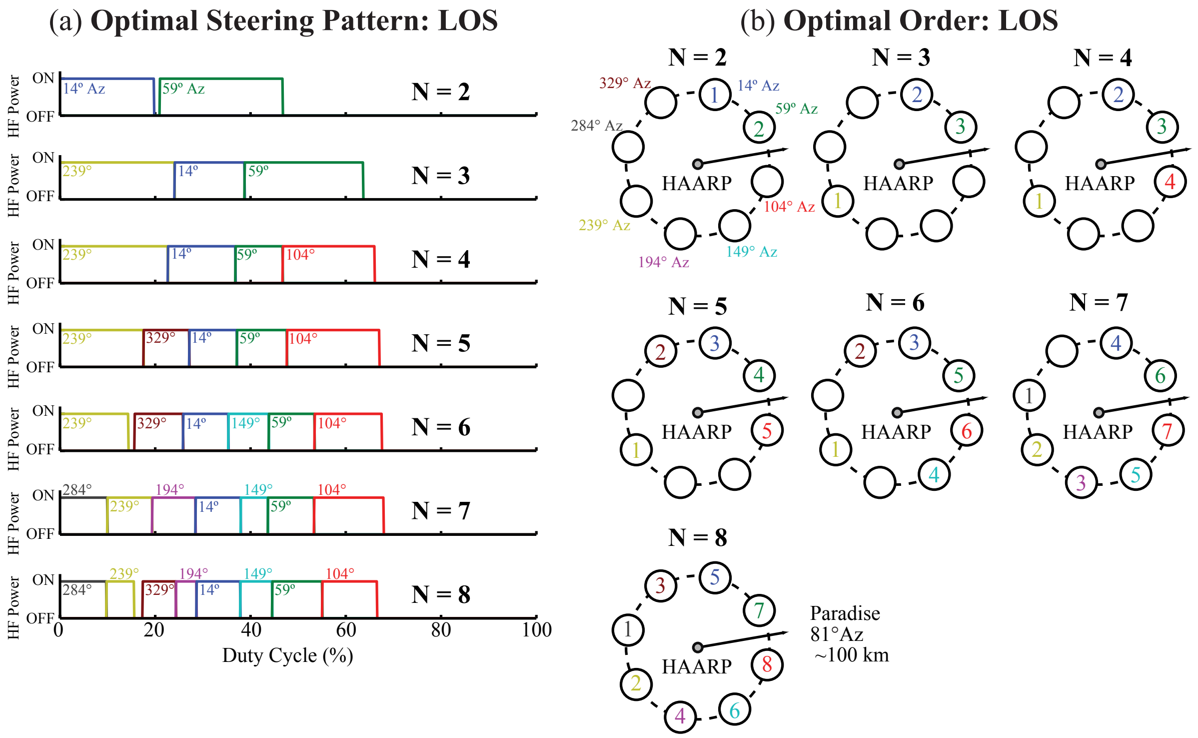

(a) **Optimal Steering Pattern: LOS**

(b) **Optimal Order: LOS**

Figure 5-8. (a) Optimal steering pattern and (b) order for various number of heating locations.

The optimal heating pattern for the LOS signal component is shown in Figure 5-8. The optimal heating order generally starts with heating locations farther from the receiver (81° az) and ends with locations closer to the receiver. This order makes up for the shorter wave propagation delays closer to the heating locations.

The duty cycle at each location becomes smaller as the number of heating locations increases. The smaller duty cycle generates ELF/VLF waves more efficiently, decreases the phase delay due to the heating order, and makes the signals interfere more constructively. The smaller duty cycle is optimally selected over the larger duty cycle which would generate larger amplitudes at each location, but would produce larger destructive interference for the total signal.

All of the optimal off-times between locations are zero except for $N = 2$, 6, and 8; even the largest off-time is only 1.7% at $N = 8$. The zero off-times are likely to produce in-phased signals with an optimal duty cycle, which is discussed in Section 5.3.3

HAARP is capable of steering the beam with 10 μsec dwell time. The dwell time corresponds to 3% duty cycle for 3 kHz modulation frequency. To implement the beam pattern in Figure 5-8

Table 5-1. Received amplitude (dB) relative to vertical AM at 50% duty cycle

Method	LOS	1.5 kHz	2.0 kHz	3.0 kHz	4.0 kHz	4.5 kHz
Optimized BP	12.1	9.8		12.2		14.4
GM (Maximum)	7.7–8.3		6.4–7.3	6.9–7.8	9.5–11.1	
GM (Full Circle)	5.9–6.1		2.6–2.8	5.4–5.6	8.4–8.8	

at HAARP, we can simply round the duty cycles at multiples of 3% and the optimized amplitudes would change only by $\sim$0.5 dB. If a higher modulation frequency is used, the dwell time becomes more significant. For instance, 10 kHz modulation frequency would have 10% duty cycle resolution in beam painting. At this high frequency, rather than rounding optimal duty cycles to 10% resolution, the gradient method can be modified so that the optimal duty cycle is updated using 10% resolution.

When it comes to symmetric heating, where there is no favor in any azimuthal direction, the optimal heating pattern is very similar to standard circle-sweep geometric modulation where the beam moves along in a circle and heats each spot at the maximum allowed time (12.5% duty cycle at each of eight locations). The post-processed amplitude for the LOS component is $\sim$2 dB larger than experimental observations of GM (Table 5-1). The discrepancy comes from the number of heating locations: geometric modulation was implemented with 12 heating steps which produce more overlapping regions at the heating locations. The overlap yields different effective duty cycles and waveforms at the heated spots, and changes the total received amplitude. While the overlap of the beams may be engineered to increase the received amplitude, the effect is not considered here.

CHAPTER 6
SUMMARY AND FUTURE WORK

6.1 Summary of Contributions

In this dissertation, I have provided transmission sequences that optimize the received ELF/VLF amplitude at a particular receiver by engineering the ELF/VLF phased array created in the *D*-region ionosphere by rapid heater beam steering at HAARP. By painting a vast area of the ionosphere at the desired ELF/VLF rate with the HF beam, I created an ON-OFF pattern at elemental source locations, and I observed larger ELF/VLF source regions with distributed amplitude and phase. Throughout the experimental observations, the TOA method was used to measure the amplitude, phase, and propagation delays of the received ELF/VLF signals.

In Chapters 2 and 3, I provide the mathematical framework for the ELF/VLF TOA analysis method in the context of ELF/VLF wave generation physics. I showed experimental observations and numerical modeling results to demonstrate that the TOA method distinguishes LOS and IR signal components and identifies the ELF/VLF source heights. The TOA observations indicate that the source height decreases with increasing modulation frequency and is mostly insensitive to the HF power levels and HF frequency.

In Chapter 4, the Geometric Modulation (GM) format is combined with a variable HF heating pulse to investigate the four important effects that contribute to the generated ELF/VLF amplitude. The results are compared with conventional AM heating. Those four effects are the area of the source region, the obliqueness of the HF beam, the effective duty cycle of the heating, and the phased array structure of the source. Using measurements of the spatial distribution of ELF/VLF amplitude and phase created by GM, an optimal heating order is identified. The results indicate that the optimal heating order increases the ELF/VLF amplitude up to 4 dB and the HF-to-ELF/VLF conversion efficiency up to 7 dB. However, for symmetric heating, the GM format (HF beam is on continuously) produces the largest amplitude.

In Chapter 5, instead of optimizing sweep speed and heating order individually, I optimize the heating durations and orders together. The observed amplitude and phase at different azimuths and duty cycles are post-processed to predict the received amplitude at Paradise. The gradient descent algorithm is employed to identify the global maximum for the received amplitude. As a result, the amplitude is increased up to 7 dB and the efficiency is increased up to 11 dB compared to GM.

6.2 Suggestions for Future Research

6.2.1 Implementation of Optimal Heating Pattern

This dissertation suggests an optimal heating pattern, but the optimal heating pattern has not yet been implemented. To confirm the prediction, observed ELF/VLF amplitudes should be directly compared to those generated using oblique AM and GM formats. The optimal format depends on ionospheric conditions. It is ideal to optimize the HF beam pattern in real-time as the ELF/VLF signals are being generated. At present, real-time implementation is unreasonable for the current ELF/VLF receiver setup and calculation time for optimization.

The provided optimization does not currently account for the overlapping of HF beams. At 3.25 MHz, the overlap of the 3 dB beamwidth is merely 10% with its neighbor heating locations when they are 45° azimuth apart. It is better to quantify this effect than to assume it is negligible. To quantify this effect, I suggest altering the HF frequency. The HF frequency controls the 3 dB beam width, with a more focused beam at higher frequencies. It is important to keep in mind that the azimuthal dependence and duty cycle response would also change for different HF frequencies. The optimal heating pattern will be bounded by the azimuthal and duty cycle step transmissions at the same HF frequency.

6.2.2 High Frequency Resolution TOA

Probably the most important next research step is the development of a high frequency resolution TOA method. The TOA observation were typically performed using a 3–4 kHz bandwidth in order to accurately discern LOS components from IR components by their time differences. The amplitude, phase, and propagation delays measured by the TOA method are averaged over the bandwidth, and as a result, frequency resolution is lost. Important physical quantities depend on frequency, however. For instance, reflection coefficients for the air-ionosphere boundary are expected to be frequency-dependent. With a high frequency resolution TOA method, it may be possible to quantify reflection coefficients as a function of frequency and provide an approximation of *D*-region properties.

6.2.3 Separation of Hall and Pedersen Currents

The orthogonal ELF/VLF antennas measure somewhat different amplitudes and phases due to direction of the auroral electrojet currents. In this dissertation, the two directional signals are modeled, but are not separated. A more in-depth study of the conductivity modulation would focus on measuring and separating the Hall and Pedersen current contributions to the ELF/VLF source. With high frequency resolution TOA method, such a decomposition of the ELF/VLF signal may be possible.

REFERENCES

Agrawal, D., and R. C. Moore (2012), Dual-beam ELF wave generation as a function of power, frequency, modulation waveform, and receiver location, *J. Geophys. Res.*, *117*, A12305.

Balanis, C. A. (1989), *Advanced Engineering Electromagnetics*, John Wiley & Sons Inc, New York.

Barr, R., and P. Stubbe (1991a), ELF radiation from the Tromsø "super heater" facility, *Geophys. Res. Lett.*, *18*(6), 1035–1038.

Barr, R., and P. Stubbe (1991b), On the ELF generation efficiency of the Tromsø heater facility, *Geophys. Res. Lett.*, *18*(11), 1971–1974.

Barr, R., and P. Stubbe (1993), ELF harmonic radiation from the Tromsø heating facility, *Geophy. Res. Lett.*, *20*(20), 2243–2246.

Barr, R., M. T. Rietveld, H. Kopka, P. Stubbe, and E. Nielsen (1985), Extra-low-frequency radiation from the polar electrojet antenna, *Nature*, *317*, 155–157.

Barr, R., M. T. Rietveld, P. Stubbe, and H. Kopka (1987), Ionospheric heater beam scanning: A mobile source of ELF radiation, *Radio Sci.*, *22*(6), 1073–1083.

Barr, R., M. T. Rietveld, P. Stubbe, and H. Kopka (1988), Ionospheric heater beam scanning: A realistic model of this mobile source of ELF/VLF radiation, *Radio Sci.*, *23*(3), 1073–1083.

Barr, R., P. Stubbe, and M. T. Rietveld (1999), ELF wave generation in the ionosphere using pulse modulated HF heating: Initial tests of a technique for increasing ELF wave generation efficiency, *Ann. Geophy.*, *17*(6), 759–769.

Barrick, D. E. (1973), FM/CW radar signals and digital processing, *Tech. Rep. ERL283-WPL20*, NOAA.

Baumjohann, W. (1982), Ionospheric and field-aligned current systems in the auroral zone: A concise review, *Adv. Space Res.*, *2*(10), 55–62.

Bernstein, S. L., M. L. Burrows, J. E. Evans, A. S. Griffiths, D. A. McNeill, C. W. Niessen, I. Richer, D. P. White, and D. K. Willim (1974), Long-range communications at extremely low frequencies, *Proc. IEEE*, *62*(3), 292–312.

Bilitza, D. (2012), Ionospheric models, `http://ccmc.gsfc.nasa.gov/modelweb/models/iri_vitmo.php`.

Boashash, B. (2003), *Time frequency signal analysis and processing : a comprehensive reference*, 743 pp., Elsevier, Oxford, UK.

Cohen, M. B. (2009), ELF/VLF phased array generation via frequency-matched steering of a continuous HF ionospheric heating beam, Ph.D. thesis, Stanford University.

Cohen, M. B., and M. Gołkowski (2013), 100 days of ELF/VLF generation via HF heating with HAARP, *J. Geophys. Res. Space Physics*, *118*, 1–11.

Cohen, M. B., U. S. Inan, and M. Gołkowski (2008), Geometric modulation: A more effective method of steerable ELF/VLF wave generation with continuous HF heating of the lower ionosphere, *Geophys. Res. Lett.*, *35*, L12101, doi:10.1029/2008GL0340610.

Cohen, M. B., U. S. Inan, M. Gołkowski, and M. J. McCarrick (2010a), ELF/VLF wave generation via ionospheric HF heating: Experimental comparison of amplitude modulation, beam painting, and geometric modulation, *J. Geophys. Res.*, *115*, A02302.

Cohen, M. B., U. S. Inan, M. Gołkowski, and N. G. Lehtinen (2010b), On the generation of ELF/VLF waves for long-distance propagation via steerable HF heating of the lower ionosphere, *J. Geophys. Res.*, *115*, A07322.

Cohen, M. B., M. Gołkowski, N. G. Lehtinen, U. S. Inan, and M. J. McCarrick (2012a), HF beam parameters in ELF/VLF wave generation via modulated heating of the ionosphere, *J. Geophys. Res.*, *117*, A05327.

Cohen, M. B., R. C. Moore, M. Gołkowski, and N. G. Lehtinen (2012b), ELF/VLF wave generation from the beating of two HF ionospheric heating sources, *J. Geophys. Res.*, *117*, A12310.

Cummer, S. A., U. S. Inan, and T. F. Bell (1998), Ionospheric *D* region remote sensing using VLF radio atmospherics, *Radio Sci.*, *33*(6), 1781–1792.

Davies, K. (1990), *Ionospheric Radio*, Peter Peregrinus Ltd., London, UK.

Dowden, R. L., J. B. Brundell, and C. J. Rodger (2002), VLF lightning location by time of group arrival (toga) at multiple sites, *J. Atomos. Sol. Terr. Phys.*, *64*(7), 817–830.

Eliasson, B., C. L. Chang, and K. Papadopoulos (2012), Generation of ELF and ULF electromagnetic waves by modulated heating of the ionospheric F2 region, *J. Geophys. Res.*, *117*, A10320.

Ferraro, A. J., H. S. Lee, R. Allshouse, K. Carroll, A. A. Tomko, and R. G. Joiner (1982), VLF/ELF radiation from the ionospheric dynamo current system modulated by powerful HF signals, *J. Atmos. Terr. Phys.*, *44*(12), 1113–1122.

Ferraro, A. J., H. S. Lee, R. Allshouse, K. Carroll, R. Lunnen, and T. Collins (1984), Characteristics of ionospheric ELF radiation generated by HF heating, *J. Atmos. Terr. Phys.*, *46*(10), 855–865.

Field, E. C., and R. D. Engel (1965), The detection of daytime nuclear bursts below 150 km by prompt VLF phase anomalies, *Proc. IEEE*, *53*(12), 2009–2017.

Frank, R. L. (1983), Current developments in Loran-C, *Proc. IEEE*, *71*(10), 1127–1139.

Fujimaru, S., and R. C. Moore (2011), Analysis of time-of-arrival observations performed during ELF/VLF wave generation experiments at HAARP, *Radio Sci.*, *46*, RS0M03.

Gabor, D. (1946), Theory of communication, *J. IEEE*, *93*(26), 429–457.

Getmantsev, G. G., N. A. Zuikov, D. S. Kotik, L. F. Mironenko, N. A. Mityakov, V. O. Rapoport, V. Y. T. Y. A. Sazonov, and V. Y. Eidman (1974), Combination frequencies in the interaction between high-power short-wave radiation and ionospheric plasma, *JETP Lett.*, *20*, 101–102.

Gill, P. E., M. W., and M. H. Wright (1981), *Practical optimization*, Academic press.

Gołkowski, M., M. B. Cohen, D. L. Carpenter, and U. S. Inan (2011), On the occurrence of ground observations of ELF/VLF magnetospheric amplification induced by the HAARP facility, *J. Geophys. Res.*, *116*, A04208.

Gołkowski, M., M. B. Cohen, and R. C. Moore (2013), Modulation of auroral electrojet currents using dual modulated HF beams with ELF phase offset, a potential *D*-region ionospheric diagnostic, *J. Geophys. Res. Space Physics*, *118*, 2350–2358.

Helliwell, R. A. (1965), *Whistlers and related ionospheric phenomena*, Dover Publications, New York.

Inan, U. S., and D. L. Carpenter (1987), Lightning-induced electron precipitation events observed at L $\sim$ 2.4 as phase and amplitude perturbations on subionospheric VLF signals, *J. Geophys. Res.*, *92*(A4), 3293–3303.

James, H. G. (1985), The ELF spectrum of artificially modulated *D*/*E*-region conductivity, *J. Atmos. Terr. Phys.*, *47*(11), 1129–1142.

James, H. G., R. L. Dowden, M. T. Rietveld, P. Stubbe, and H. Kopka (1984), Simultaneous observations of elf waves from an artificially modulated auroral electrojet in space and on the ground, *J. Geophys. Res.*, *89*(A3), 1655–1666.

Jin, G., M. Spasojevic, and U. S. Inan (2009), Relationship between electrojet current strength and ELF signal intensity in modulated heating experiments, *J. Geophys. Res.*, *114*, A08301.

Jin, G., M. Spasojevic, M. B. Cohen, U. S. Inan, and N. G. Lehtinen (2011), The relationship between geophysical conditions and ELF amplitude in modulated heating experiments at HAARP: Modeling and experimental results, *J. Geophys. Res.*, *116*, A07310.

Jin, G., M. Spasojevic, M. B. Cohen, and U. S. Inan (2012), Harmonic minimization waveforms for modulated heating experiments at HAARP, *J. Geophys. Res.*, *117*, A11315.

Kotik, D. S., and E. N. Ermakova (1998), Resonances in the generation of electromagnetic signals due to the thermal cubic nonlinearity in the lower ionosphere, *J. Atmos. Sol. Terr. Phys.*, *60*(12), 1257–1259.

Lauben, D. S., U. S. Inan, and T. F. Bell (2001), Precipitation of radiation belt electrons induced by obliquely propagating lightning-generated whistlers, *J. Geophys. Res.*, *106*, 29,745–29,770, doi:10.1029/1999JA000155.

Lev-Tov, S. J., U. S. Inan, and T. F. Bell (1995), Altitude profiles of localized *D* region density disturbances produced in lightning-induced electron precipitation events, *J. Geophys. Res.*, *100*(A11), 21,375–21,383.

Lewis, E. A., J. E. Rasmussen, and P. A. Kossey (1973), Measurements of ionospheric reflectivity from 6 to 35 khz, *J. Geophys. Res.*, *78*(19), 3903–3912.

Lunnen, R. J., H. S. Lee, A. J. Ferraro, T. W. Collins, and R. F. Woodman (1984), Detection of radiation from a heated and modulated equatorial electrojet current system, *Nature*, *311*, 134–135.

Merrill, J. (1974), Some early historical aspects of project sanguine, *Communications, IEEE Transactions on.*, *22*(4), 359–363, doi:10.1109/TCOM.1974.1092206.

Milikh, G. M., and K. Papadopoulos (2007), Enhanced ionospheric ELF/VLF generation efficiency by multiple timescale modulated heating, *Geophy. Res. Lett.*, *34*, L20804.

Moore, R. C. (2007), ELF/VLF wave generation by modulated HF heating of the auroral electrojet, Ph.D. thesis, Stanford University, Stanford, CA.

Moore, R. C., and D. Agrawal (2011), ELF/VLF wave generation using simultaneous CW and modulted HF heating of the ionosphere, *J. Geophys. Res*, *116*, A04217, doi:10.1029/2010JA015902.

Moore, R. C., and M. T. Rietveld (2009), Comment on ”Geometric modulation: A more effective method of steerable ELF/VLF wave generation with continuous HF heating of the lower ionosphere” by M. B. Cohen, U. S. Inan, and M. A. Gołkowski, *Geophy. Res. Lett.*, *36*, L04101.

Moore, R. C., C. P. Barrington-Leigh, U. S. Inan, and T. F. Bell (2003), Early/fast vlf events produced by electron density changes associated with sprite halos, *J. Geophys. Res. (Space Physics)*, *108*, 1363, doi:10.1029/2002JA009816.

Moore, R. C., U. S. Inan, and T. F. Bell (2006), Observations of amplitude saturation in ELF/VLF wave generation by modulated HF heating of the auroral electrojet, *Geophys. Res. Lett.*, *33*, L12106.

Moore, R. C., U. S. Inan, T. F. Bell, and E. J. Kennedy (2007), ELF waves generated by modulated HF heating of the auroral electrojet and observed at a ground distance of $\sim$4400 km, *J. Geophys. Res*, *112*, A05309.

Moore, R. C., S. Fujimaru, D. A. Kotovsky, and M. Gołkowski (2013), Observations of ionospheric ELF and VLF wave generation by excitation of the thermal cubic nonlinearity, *Phys. Rev. Lett.*, *111*, 235007.

Papadopoulos, K., T. Wallace, M. McCarrick, G. M. Milikh, and X. Yang (1989), On the efficient operation of a plasma ELF antenna driven by modulation of ionospheric currents, *Comments Plasma Phys. Controlled Fusion*, *13*(1), 1–17.

Papadopoulos, K., C. Chang, P. Vitello, and A. Drobot (1990), On the efficiency of ionospheric ELF generation, *Radio Sci.*, *25*(6), 1311–1320.

Papadopoulos, K., T. Wallace, G. M. Milikh, W. Peter, and M. McCarrick (2005), The magnetic response of the ionosphere to pulsed HF heating, *Geophys. Res. Lett.*, *32*, L13101.

Papadopoulos, K., N. A. Gumerov, X. Shao, I. Doxas, and C. L. Chang (2011a), HF-driven currents in the polar ionosphere, *Geophys. Res. Lett.*, *38*, L12103.

Papadopoulos, K., C. L. Chang, J. Labenski, and T. Wallace (2011b), First demonstration of HF-driven ionospheric currents, *Geophys. Res. Lett.*, *38*, L20107.

Payne, J. A., U. S. Inan, F. R. Foust, T. W. Chevalier, and T. F. Bell (2007), HF modulated ionospheric currents, *Geophys. Res. Lett.*, *34*, L23101, doi:10.1029/2007GL031724.

Raghuram, R., R. Smith, and T. Bell (1974), VLF antarctic antenna: Impedance and efficiency, *IEEE Trans. Antennas Propag.*, *22*(2), 334–338.

Ratcliffe, J. A. (1959), *The magneto-ionic theory and its applications to the ionosphere*, vol. 206, Cambridge Univ. Press, London, UK.

Riddolls, R. J. (2003), Structure of the polar electrojet antenna, Ph.D. thesis, Massachusetts Institute of Technology, Cambridge, MA.

Rietveld, M. T., H. Kopka, E. Nielsen, P. Stubbe, and R. L. Dowden (1983), Ionospheric electric field pulsations: A comparison between VLF results from an ionospheric heating experiment and STARE, *J. Geophys. Res.*, *88*(A3), 2140–2146.

Rietveld, M. T., R. Barr, H. Kopka, E. Nielsen, P. Stubbe, and R. L. Dowden (1984), Ionospheric heater beam scannning: A new technique for ELF studies of the autoral ionosphere, *Radio Sci.*, *19*(4), 1069–1077.

Rietveld, M. T., H. Kopka, and P. Stubbe (1986), *D*-region characteristics deduced from pulsed ionospheric heating under auroral elecrojet conditions, *J. Atmos. Terr. Phys.*, *48*(4), 311–326.

Rietveld, M. T., H. P. Mauelshagen, P. Stubbe, H. Kopka, and E. Nielsen (1987), The characteristics of ionospheric heating-produced ELF/VLF waves over 32 hours, *J. Geophys. Res.*, *92*(A8), 8707–8722.

Rietveld, M. T., P. Stubbe, and H. Kopka (1989), On the frequency dependence of ELF/VLF waves produced by modulated ionospheric heating, *Radio Sci.*, *24*(3), 270–278.

Said, R. K., U. S. Inan, and K. L. Cummins (2010), Long-range lightning geolocation using a VLF radio atmospheric waveform bank, *J. Geophys. Res.*, *115*, D23108.

Schuster, S., S. Scheiblhofer, L. Reindl, and A. Stelzer (2006), Performance evaluation of algorithms for SAW-based temperature measurement, *IEEE Trans. Ultrason., Ferroelectr., Freq. Control*, *53*, 1177–1185.

Segalovitz, A., and B. R. Frieden (1978), A ”CLEAN”-type deconvolution algorithm, *Astron. Astrophys. Suppl.*, *70*, 335–343.

Stubbe, P., H. Kopka, and R. L. Dowden (1981), Generation of ELF and VLF waves by polar electrojet modulation: Experimental results, *J. Geophys. Res.*, *86*(A11), 9073–9078.

Stubbe, P., H. Kopka, M. T. Rietveld, and R. L. Dowden (1982), ELF and VLF wave generation by modulated HF heating of the current carrying lower ionosphere, *J. Atmos. Terr. Phys.*, *44*(12), 1123–1135.

Stubbe, P., H. Kopka, M. T. Rietveld, A. Frey, P. Høeg, H. Kohl, E. Nielsen, G. Rose., C. LaHoz, R. Barr, H. Derblom, r. Hedberg, B. Thide, T. B. Jones, T. Robinson, A. Brekke, T. Hansen, and O. Holt (1985), Ionospheric modification experiments with the Tromsø heating facility, *J. Atmos. Terr. Phys.*, *47*(12), 1151–1163.

Swanson, E. R. (1983), Omega, *Proc. IEEE*, *71*(10), 1140.

Tomko, A. A. (1981), Nonlinear phenomena arising from radio wave heating of the lower ionosphere, Ph.D. thesis, The Pennsylvania State University.

Villascfior, J., A. Y. Wong, B. Song, J. Pau, and M. McCatrick (1996), Comparison of ELF/VLF generation modes in the ionosphere by the HIPAS heater array, *Radio Sci.*, *31*(1), 211–226.

Watt, A. D. (1967), *VLF Radio Engineering*, Pergamon Press Oxford.

BIOGRAPHICAL SKETCH

Shuji Fujimaru received his bachelor's degree in electrical and computer engineering from the University of Florida in 2009. With the Alumni Fellowship award from the University of Florida, he entered the Ph.D program in electrical and computer engineering. He received the master's degree in 2011 with guidance from Dr. Robert Moore, and continued to complete Ph.D in 2014. His research focuses on ELF/VLF generation using modulated HF heating of the lower ionosphere. His studies are mainly applied to electromagnetics, plasma physics, and signal processing.